Published in final edited form as:

J Fluid Mech. 2020 June 10; 892: . doi:10.1017/jfm.2020.170.

Surfactant dynamics: hidden variables controlling fluid flows

Harishankar Manikantan[†], **Todd M. Squires**

Department of Chemical Engineering, University of California, Santa Barbara Santa Barbara, CA 93106, USA

Abstract

Surfactants – molecules and particles that preferentially adsorb to fluid interfaces – play a ubiquitous role in the fluids of industry, of nature, and of life. Since most surfactants cannot be seen directly, their behavior must be inferred from their impact on observed flows, like the buoyant rise of a bubble, or the thickness of a coating film. In so doing, however, a difficulty arises: physically distinct surfactant processes can affect measurable flows in qualitatively identical ways, raising the specter of confusion or even misinterpretation. This Perspective describes, in one coherent piece, both the equilibrium properties and dynamic processes of surfactants, to better enable the fluid mechanics community to understand, interpret, and design surfactant/fluid systems. Specifically, §2 treats the equilibrium thermodynamics of surfactants at interfaces, including surface pressure, isotherms of soluble and insoluble surfactants, and surface dilatational moduli (Gibbs and Marangoni). §3 describes surfactant dynamics in fluid systems, including surfactant transport and interfacial stress boundary conditions, the competition between surface diffusion, advection, and adsorption/desorption, Marangoni stresses and flows, and surface excess rheology. §4 discusses paradigmatic problems from fluid mechanics that are impacted by surfactants, including translating drops and bubbles, surfactant adsorption to clean and oscillating interfaces; capillary wave damping, thin film dynamics, foam drainage, and the dynamics of particles and probes at surfactant-laden interfaces. Finally, §5 discusses the additional richness and complexity that frequently arise in ‘real’ surfactants, including phase transitions, phase coexistence, and polycrystalline phases within surfactant monolayers, and their impact on non-Newtonian surface rheology.

Graphical Abstract

hmanikantan@ucdavis.edu.

[†]current address: Department of Chemical Engineering, University of California, Davis, CA 95616, USA.

Declaration of Interests: The authors report no conflict of interest.

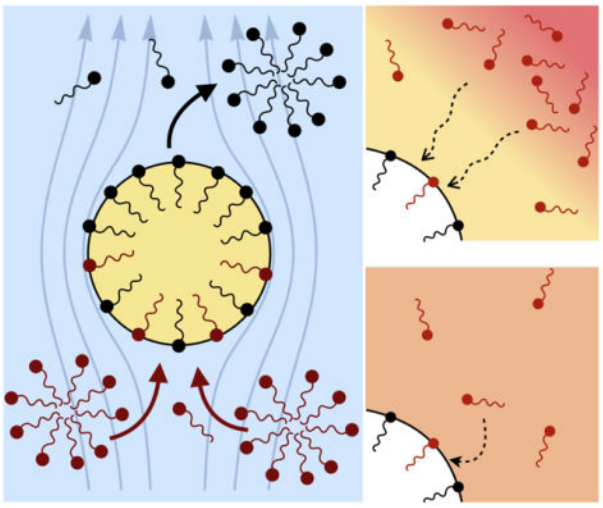

1. Introduction

Interfaces between fluids appear throughout science, technology, industry and nature. Bubbles are generated by crashing waves in the ocean, by agitation in washing machines, during froth flotation in the mining and energy industries, and when super-saturated, dissolved gasses nucleate and grow bubbles in sodas, geysers, canned whipped cream, and during fermentations. Droplets of one liquid may be emulsified in a second immiscible liquid – as found in foods, consumer products, pharmaceuticals, oil production and processing. Sea surfaces may be smooth and glassy, or riddled with capillary waves.

Almost without exception, ‘surface-active’ molecules and/or particles – collectively called ‘surfactants’ – control the initiation, dynamics, and behavior of these and other processes. The fluid mechanics community knows quite well that surfactants reduce the interfacial tension of liquid surfaces, thus lowering the energetic cost of blowing bubbles or inflating lungs. By extension, surfactant gradients are well-known to exert ‘Marangoni’ stresses on fluid interfaces, often driving or influencing the flow of the fluids that form them.

Surfactants also impact a variety of scientific and industrial processes through a number of processes and mechanisms that are not so clear. A simple example highlights the difficulties that arise: the buoyant rise of a small bubble through a Newtonian liquid (figure 1). A bubble of radius R with perfectly clean surface rises according to the classic Stokes drag calculation, imposing a no-shear stress boundary condition, to give

$$U^c = \frac{F}{4\pi\eta R}, \tag{1.1}$$

where F is the drag and η is the shear viscosity of the fluid. In many cases, however, bubbles rise with velocities much closer to

$$U^s = \frac{F}{6\pi\eta R}, \tag{1.2}$$

as one would expect for a rigid particle. What is the reason?

A vague acknowledgment that surfactants exist doesn't help much. In fact, a number of phenomena may be responsible for the slower rise. Boussinesq (1913) originally surmised that the fluid/gas interface might itself have some surface excess viscosity, dissipating energy as it deforms (figure 1 *b*). A more modern understanding holds that such surface viscosities are established by the surfactants adsorbed to the interface. Even without surface rheology, bulk viscous stresses advect surfactant to the rear of the bubble as it rises (figure 1 *e*), establishing a concentration gradient that drives a counter-acting Marangoni stress (figure 1 *f*). The strength of this gradient depends on how the surfactant responds (Levich 1962) to being driven out of equilibrium. Insoluble surfactants diffusively fight to equalize their surface concentration (figure 1 *g*). Soluble surfactants adsorb and desorb from the interface to maintain an equilibrium (figure 1 *h*). If this equilibration process occurs slowly, gradients (and Marangoni stresses) are strong; conversely, rapid equilibration causes only weak gradients.

It is hard to imagine a simpler experiment than this – measuring the rise velocity of a nearly spherical bubble in a liquid, say as a function of bubble radius. If the measured velocity matches U^c from (1.1), one can conclude that the drop is clean. If, on the other hand, the measured velocity is slower than U^c, the discrepancy might be caused by (a) inherent surface viscosity; (b) surface viscosity due to a surfactant; (c) flow-induced Marangoni stresses from an insoluble surfactant; (d) flow-induced Marangoni stresses from a soluble surfactant, the magnitude of which might be determined by (i) adsorption/desorption rate kinetics; or (ii) surfactant diffusion across the bubble; (iii) convection-diffusion transport of surfactant across the bubble. However sensible figure 1 *a* may seem, the x-axis is often difficult to unambiguously determine.

This difficulty – of identifying mechanisms by which surfactants act – arises much more broadly, in systems and processes that are much more complicated. Surfactants influence film thicknesses in coating flows (Quéré 1999; Shen *et al.* 2002; Scheid *et al.* 2010), the dispersion of surface waves (Levich 1962; Lucassen & Hansen 1966), the dynamics and thicknesses of spreading films (Troian *et al.* 1990; Darhuber & Troian 2005), and the lifetime of foams and emulsions (Langevin 2000; Cohen-Addad *et al.* 2013). Mechanisms by which these effects arise can be complicated and varied. For example, surfactants may provide additional energetic barriers to droplet and bubble coalescence: surfactants on either side of a liquid film may repel each other sterically or electrostatically, and thus retard or arrest the thinning of the film (Bibette *et al.* 1992; Stancik *et al.* 2004). Alternatively, or additionally, dynamic mechanisms may also act: surfactants advected by thinning films establish gradients, and thus Marangoni stresses, that oppose the film drainage (Leal 2004). Monolayers of surfactant may introduce an excess surface viscosity, elasticity, or visco-elasticity that retards or alters film thinning (Langevin 2000). Even more subtle, surfactant exchange between the bulk and the interface can mimic surface-excess (dilatational) viscosity, masking the physical origin of the dissipation (Levich 1962; Lucassen & van den Tempel 1972).

Despite the controlling influence that surfactants exert over many fluid systems, the surfactants themselves are effectively invisible in most experiments, and to most techniques. Interpreting such experiments becomes challenging at best, given that physically distinct surfactant processes impact measurements in identical ways. In many ways, surfactants behave like 'hidden variables' that cannot be measured directly, yet influence fluid flows so profoundly that they must be determined in order to understand even gross, qualitative fluid phenomena. Surfactant distributions are thus typically *inferred* from observable fluid phenomena – e.g. measured fluid velocity fields, free surface dynamics, or Laplace pressure measurements. Connecting measurements and observations with the underlying surfactant fields, however, requires some model for the dynamics and mechanics of surfactant transport.

The fact that physically distinct surfactant processes can impact measurable properties in the same way – while the surfactants themselves elude detection – has caused significant confusion. For example, the origin and even existence of surface rheology has long been controversial (Scriven & Sternling 1960), with justifiable reason: if Marangoni stresses can explain an experimental observation, what is the need to invoke surface rheology? Why should a rightly skeptical scientist invoke some nebulous phenomenon, when established processes can explain measurements? At the same time, plausible mechanisms should not be dismissed out of hand: after all, however familiar a process may be, it might actually not be the one responsible for an observation.

Understanding these surfactant systems – and ultimately predicting and designing them – requires that these mechanisms and processes be differentiated unambiguously. This might be accomplished by specifically designing experiments to excite one process but not others: forcing a surfactant-laden interface to deform in a purely shear fashion – i.e., with zero compression or dilation – should not trigger Marangoni stresses, but would be sensitive to surface shear rheology. In systems with compression, it may not be easy or even possible to separate stresses cause by surface dilatational viscosity – an intrinsic material property – from an *effective* surface viscoelasticity due to surfactant adsorption and desorption, surface and bulk diffusion, aggregation or phase transitions, Marangoni flows, or some combination of these processes. Knowing how these processes scale with e.g. system geometry, fluid velocity, surfactant concentrations and properties, however, might suggest complementary experiments to tease apart these influences.

The objective of this Perspective, then, is to enumerate and elucidate the multitude of transport processes involved in the formation, flow and rheological response of surfactant-laden interfaces, and therefore to better understand, interpret, predict, and design surfactant-fluid flows and materials. By presenting these diverse phenomena in one comprehensive piece, described using the same language and within the same context, we hope to to empower the fluid mechanics and soft condensed matter physics communities to discern and differentiate between the various dynamics surfactants might cause. We also hope to connect the fluid mechanics community to the physical chemistry literature on surfactants, which is more steeped in equilibrium thermodynamics than typical fluid mechanicians have at their fingertips. To this end, this Perspective highlights paradigmatic examples chosen for their

pedagogic value in weaving a coherent and compelling picture of surfactant dynamics, rather than a comprehensive treatment of this vast literature.

In what follows, we treat surfactants from the physical-chemical standpoint, hopefully giving the fluid mechanician enough basis to connect with the surfactant literature. We will start with equilibrium arguments about surface tension and surface pressure, including the equilibrium properties of soluble and insoluble surfactants (§2). We then move on to dynamic processes – which tend to be more familiar to the fluid mechanician – and discuss the various ways in which surfactant is transported (§3). We will touch on surface rheology, which is relatively unfamiliar to both communities. Then, in §4, we show how even these most basic treatments give rise to remarkable richness in a series of paradigmatic problems: (§4.1) the buoyant translation of bubbles and drops; (§4.2) the oscillatory compression of soluble monolayers; (§4.3) surface wave dynamics; (§4.4) coating flows; (§4.5) foam drainage; and (§4.6) particle motion within surfactant-laden interfaces. These problems are chosen both for their ubiquity and importance, as well as the nontrivial and rich phenomena that appear even for the simplest assumptions for the processes described in §3. Finally, in §5, we present a variety of complexities that arise even in common surfactant systems – beyond the ‘simplest’ treatments in §2–4 – with the goal of highlighting areas where standard assumptions may not capture experimental observations, and to encourage new directions for research and innovation.

2. Interfaces at Equilibrium

2.1. Surface tension and its origins

Surface tension originates from the imbalance in mutually attractive forces felt by molecules near an interface. A liquid molecule in the bulk of a fluid is surrounded by neighbors of the same kind, all exerting attractive intermolecular forces. Molecules that are surrounded experience no net force, due to the symmetric distribution of their neighbors. A force is required to pull one molecule out of the bulk liquid, however: one must supply enough free energy to break the N ‘bonds’, each of strength ΔU.

A molecule near an immiscible fluid-fluid interface, however, feels a net force towards the fluid phase with higher intermolecular attractions. These interfacial molecules are in an energetically unfavorable state, and creation of additional interfacial area is expensive. A fluid system, therefore, minimizes interfacial area. The surface tension γ of a fluid-fluid interface is then the energy associated with creating excess area, which depends on the strength of intermolecular forces in both bulk phases. For example, a clean air-water interface has $\gamma \approx 0.072$ J/m^2, or equivalently, 72 mN/m.

The surface tension of a liquid can be estimated with the simple thought experiment depicted in figure 2. Each molecule in the bulk liquid has attractive interactions with N neighbors. Cleaving the bulk into two, and therefore creating two interfaces, requires $N/2$ bonds, each of energy ΔU, to be supplied for every interfacial molecule. Given Γ_s molecules per unit area, cleaving these bonds requires an energy per unit area

$$\gamma \sim N \Delta U \Gamma_s . \tag{2.1}$$

Of course, molecules at the interface might relax and re-arrange, changing the energetics of interfacial molecules, but we neglect these small changes. The interaction energy $N\Delta U$ must be $O(k_B T)$ in order for the bulk to be a liquid: if the interaction energy were much stronger than thermal energy ($N\Delta U \gg k_B T$), molecules would lock in place as a solid or glass, whereas if it were much weaker ($N\Delta U \ll k_B T$), the molecules would fly apart to form a gas. Ignoring numerical prefactors, this suggests a surface tension

$$\gamma \sim k_B T \Gamma_s . \tag{2.2}$$

However crude, this approximation gives reasonable estimates: assuming water molecules to have an approxmate radius $r_w \sim 0.2$ nm (based on the bulk density and molecular mass of water) suggests water molecules occupy the interface with density $\Gamma_s \sim 9/\text{nm}^2$. Using $k_B T \sim 4$ pN nm at room temperature gives $\gamma \sim 40$ mN/m, which is within a factor of two of the measured value 72 mN/m. More generally, most liquids with approximately Angstrom radii thus have surface tensions in the tens of mN/m.

Surface tension can be alternatively interpreted in terms of the mechanical work done in stretching an interface. If the application of a force F within the plane of the interface changes its area by $\mathrm{d}A$, the net change in energy is a sum of mechanical work done and the surface energy associated with surface tension:

$$\mathrm{d}U = -F\mathrm{d}x + \gamma \mathrm{d}A . \tag{2.3}$$

At mechanical equilibrium, $\mathrm{d}U = 0$, and writing $\mathrm{d}A = \ell \mathrm{d}x$ where ℓ is the width of the interfacial layer, we find $\gamma = F/\ell$ In other words, surface tension gives the force per unit length to create interfacial area.

Finally, γ can be thought of as a surface stress, pulling isotropically within the plane of the interface, and is therefore analogous to a negative 3D pressure. We will soon extend this analogy with 3D pressure, as surfactants exert a ‘surface pressure’, Π, against the surface tension γ of the clean interface.

Unlike bulk 3D fluids, however, surfaces are two-dimensional and can be curved, which modifies the static stress required to create additional area. For example, increasing the volume of a bubble of gas A suspended at equilibrium in liquid B increases the surface area of the bubble, and therefore its interfacial energy. If the bubble radius increases from R to $R + \mathrm{d}R$, the net free energy change is

$$\mathrm{d}U = -p_A \mathrm{d}V_A - p_B \mathrm{d}V_B + \gamma_{AB} \mathrm{d}A, \tag{2.4}$$

where γ_{AB} is the surface tension of the A–B interface, p_A and p_B are the pressures inside and outside the bubble, respectively, $\mathrm{d}V_A = -\mathrm{d}V_B = 4\pi R^2 \mathrm{d}R$ and $\mathrm{d}A = 8\pi R \mathrm{d}R$. Imposing $\mathrm{d}U = 0$ to satisfy mechanical equilibrium reveals the well-known Laplace pressure jump across the bubble surface,

$$\Delta p = p_A - p_B = \frac{2\gamma_{AB}}{R}. \tag{2.5}$$

The larger the interfacial curvature or surface tension, the greater is the bulk fluid pressure required to maintain the system in equilibrium: smaller bubbles have a higher internal pressure. More generally, the Laplace pressure is given by the Young-Laplace equation (Leal 2007):

$$\Delta p = \gamma_{AB} \nabla_s \cdot \boldsymbol{n}, \tag{2.6}$$

where $\boldsymbol{n}$ is the normal to the interface, pointing away from the fluid A, $\nabla_s = (\boldsymbol{I} - \boldsymbol{nn}) \cdot \nabla$ is the surface gradient operator, and $\nabla_s \boldsymbol{n}$ is the mean curvature of the surface.

2.2. ‘Dirty’ interfaces: surfactants of different classes

Many surfactants are ‘amphiphilic’ – having both hydrophilic and hydrophobic parts – and adsorb to surfaces to minimize energetically unfavorable interactions. For instance, amphiphilic molecules adsorb to a water-air interface with their hydrophobic tails directed out of the water phase (figure 3). Adsorption to a surface comes at a cost, however: the bulk fluid offers a wider range of translational and rotational micro-states and therefore, a larger entropy per surfactant molecule. At equilibrium, the balance between adsorbed surfactants, with surface concentration Γ, and dissolved surfactants, with bulk concentration C, reflects a balance between the (favorable) enthalpy change and the (unfavorable) entropy loss that occurs during adsorption. With increasing bulk concentration, the balance between the energetic expense of hydrophobic groups remaining within the bulk and the entropic loss of moving to the interface tilts in favor of adsorption (figures 3 *b*,c) and a monolayer of increasing surface concentration Γ forms at the interface.

The affinity of surfactant molecules towards interfaces creates a surface ‘excess’ concentration, Γ. In other words, Γ is the number of molecules per unit interfacial area in excess of a hypothetical reference state, in which the adjoining bulk phases maintain their constant concentrations (figure 3 *c*) up until the surface. The position of the surface itself is arbitrary, and is typically chosen such that the surface excess concentration of the solvent is zero.

It is conceptually simple to appreciate the surface-active nature of molecules with physically distinct hydrophilic and hydrophobic portions, as depicted in figure 3 (*a*). Such clearly differentiated portions, however, are not necessary for surface-activity. The basic surfactant argument holds just as well for chemically homogeneous molecules or particles that possess an intermediate wettability with respect to the fluids on either side of the interface (Binks 2002).

Any species (molecular or particulate) that has a positive surface excess is – by definition – a surfactant. And so – what are the options? How much do they reduce surface tension? What time scales emerge? The *equilibrium* properties of different classes of surfactants can differ substantially, as shown in figure 4. All cases depict a spherical liquid drop of surface area A_i whose shape is deformed and held at a final surface area A_f, for an increase of ΔA. The

clean, surfactant-free drop (figure 4 *a*) serves as a base case: the extra surface area ΔA created by deforming at the interface comes at the cost of the 'clean' surface tension γ_0 of the liquid/liquid interface, requiring an additional energy $\Delta U = \gamma_0 \Delta A$.

Many surfactants are *soluble*, meaning that the surface excess concentration Γ of adsorbed surfactant equilibrates with the dissolved concentration C according to an *isotherm* (table 1). When a drop is initially coated with soluble surfactant at surface coverage Γ_{eq} and then deformed to create extra area ΔA, the interfacial concentration Γ drops below its equilibrium with the bulk concentration C. Bulk surfactant is then driven to adsorb to the interface, until the equilbrium surface coverage ($\Gamma_f = \Gamma_{eq}$) is restored (figure 4 *b*). At steady state, the surface tension of the drop is thus equal to the initial, equilibrium value $\gamma_{eq}(C)$, which is lower than the clean surface tension γ_0. The energetic cost of this deformation is thus reduced to $\Delta U = \gamma_{eq} \Delta A$.

Some surfactants are *insoluble* in the bulk solution, meaning that there are no surfactants dissolved in the 'reservoir,' and the number N of surfactants on an interface remains constant. Deforming a drop coated with *insoluble* surfactants (figure 4 *c*) decreases the surface concentration to $\Gamma_f = \Gamma_i A/(A+\Delta A)$, which typically *increases* the surface tension according to an equilibrium isotherm $\gamma(\Gamma)$ (§2.3). The change in surface energy is then $\Delta U = \int \gamma(\Gamma)\, \mathrm{d}A$.

Small particles with intermediate wettability can also act like surfactants – forming the basis for so-called 'Pickering' emulsions (Binks 2002). Nanoparticles often adsorb *extremely* strongly to fluid interfaces – with millions or billions of $k_B T$ in binding energy. However strong this binding energy may be, deforming a particle-laden drop creates 'clean' interface, at a cost given by the clean liquid surface tension γ_0 (figure 4 *d*). Therefore, particles do not affect the surface tension in any appreciable way if they do not interact with each other. Mutually repulsive interfacial particles, for example, relax and separate when the drop is deformed (figure 4 *e*). Clean fluid interface is created at a cost γ_0, but reducing interparticle repulsion 'returns' some energy per area $\Pi_{int}(\Gamma)$, giving a net surface tension $\gamma_{eff}(\Gamma) = \gamma_0 - \Pi_{int}(\Gamma)$, and the energetic cost of deformation takes the same form as for an insoluble surfactant.

Figure 4 gives some sense for the diverse ways that surfactants behave when one waits 'long enough'. In what follows (§2.3–3), we address questions raised by this figure. What differentiates soluble surfactants from insoluble ones? What determines the surface tension $\gamma(\Gamma)$ or $\gamma(C)$? How long is 'long enough,' and what happens 'in between'?

2.3. Insoluble surfactants: Langmuir monolayers

A lot of salt can be dissolved in water – but not an infinite amount. Above some solubility limit C_{sol}, additional salt does not dissolve, but remains in solid form and sediments. Substances with extremely low solubility in a liquid – like wax in water – are said to be 'insoluble', meaning that the concentration of dissolved molecules is immeasurably small. Likewise, surfactants can be insoluble when the precipitated (aggregated) form is energetically so much more favorable than the dissolved form. Surfactants may gain entropy by dissolving, but this comes at the cost of disrupting attractive interactions between

surfactants, and also entropic loss of solvent molecules. Crudely speaking, the larger the hydrophobic component, the lower the solubility of a surfactant in water. Phospholipids represent one class of surfactants that is frequently insoluble in water owing to the two (hydrophobic) hydrocarbon tails attached to each hydrophilic head group. The insolubility of phospholipids is essential for important biological functions: biological membranes typically consist of phospholipid bilayers – two 'sheets' of phospholipids, oppositely oriented, so that the hydrophilic heads face the water, and hydrophobic tails are buried internally.

Monolayers formed by insoluble surfactants are called *Langmuir monolayers*, and can be prepared and controlled by literally spreading a known number N of surfactant molecules onto a fluid surface of area A, to give a surface concentration

$$\Gamma = \frac{N}{A}. \tag{2.7}$$

Langmuir troughs allow this surface concentration Γ of insoluble surfactants to be controlled using mobile barriers to change the area A available to the N surfactants on the monolayer.

Any fluid mechanician should expect that spreading some number N of insoluble surfactants onto a fluid interface of area A will lower its surface tension. Real questions lie just beyond this qualitative, 'binary' expectation. How much does the surface tension change? Why do different surfactants behave differently, both in static and dynamic situations?

The simplest Langmuir monolayer consists of 'ideal' surfactants that are so dilute that they behave as point-like and non-interacting. The free energy required to assemble such ideal monolayers reflects the contribution from mixing entropy alone:

$$\mathcal{F}_s^{\text{ideal}} = N\mu_s^0 + k_B T\left[N\ln\left(\frac{N}{\Gamma_0 A}\right) - N\right], \tag{2.8}$$

where μ_s^0 is the free energy per surfactant (chemical potential) of a reference monolayer of surfactant concentration Γ_0. Equation (2.8) represents the 2D analog of an (3D) ideal gas.

Just like the pressure of a 3D material is defined by the energy required to compress it isothermally,

$$P = -\left.\frac{\partial \mathcal{F}}{\partial V}\right|_{T,N}, \tag{2.9}$$

the *surface pressure* Π exerted by a species bound to a surface is determined by the energy required to compress it isothermally, in 2D:

$$\Pi = -\left.\frac{\partial \mathcal{F}_s}{\partial A}\right|_{T,N}. \tag{2.10}$$

The surface pressure of an *ideal* Langmuir monolayer (2.8) can then be computed using (2.10) to give

$$\Pi_{\text{ideal}} = k_B T \Gamma, \tag{2.11}$$

as should be expected for an ideal, 2D gas.

Despite its clear analogy to 3D pressure, and its clear thermodynamic status, the surface pressure Π is largely unfamiliar to the fluid mechanics community. It can, however, be simply connected to more familiar terrain. Namely, the surface tension γ_0 of clean fluid interfaces pulls on interfaces, acting to *reduce* interfacial area. At the same time, the surface pressure Π of adsorbed surfactant *pushes outward* on interfaces, acting to *increase* interfacial area. The net effect is what a fluid mechanician would simply call the surface tension $\gamma(\Gamma)$:

$$\gamma(\Gamma) = \gamma_0 - \Pi(\Gamma). \tag{2.12}$$

In other words, the surface pressure $\Pi(\Gamma)$ exerted by a surfactant monolayer represents the *reduction* in surface tension caused by the surfactant.

Although intuitive and straightforward, the ideal gas model, (2.8) and (2.11), is almost never appropriate in describing real surfactants. This can be seen by evaluating (2.11) to determine the surface concentration Γ_1 required for an ideal gas surfactant to reduce surface tension by a nominal amount, e.g. $\Pi_1 \sim 1$ mN/m, which is just over 1% of the surface tension of clean water:

$$\Gamma_1^{\text{ideal}} = \frac{\Pi_1}{k_B T} \approx \frac{1\,\text{mN/m}}{4\,\text{pN nm}} \approx \frac{1\,\text{surfactant}}{4\,\text{nm}^2}. \tag{2.13}$$

Ideal gas surfactants must be packed to surface concentrations of at least one per few square nanometers to exert even a small surface pressure, but must nonetheless obey the ideal gas conditions. First, each surfactant must behave as 'point-like,' meaning that its molecular radius must be *signficantly* smaller than 2 nm. This restriction effectively renders the ideal gas description invalid for proteins, nanoparticles, and colloids. Second, intermolecular interactions must be negligible over ~nm length scales – also a rarity, given the strength of van der Waals interactions between hydrophobic tails, interfacial electrostatic dipoles, and electrostatic repulsions between headgroups at nm length scales.

If surfactant monolayers can not be described by ideal gas behavior, then how can one describe them? In many cases, Π versus Γ isotherms are simply *measured*. However, 'simple' violations of the point-like and non-interacting assumptions in the ideal gas model can be accommodated analogous to treatments of 3D gasses.

For example, the Langmuir isotherm accounts for finite surfactant size $A_0 \equiv 1/\Gamma_\infty$ by effectively allowing them to occupy sites on a lattice. Assuming N surfactants to occupy a fraction of $N_\infty = \Gamma_\infty A$ such sites, the free energy of the interface is (Diamant & Andelman 1996; Kralchevsky *et al.* 2008)

$$\mathcal{F}_s^{\text{L}} = N\mu_s^0 + k_B T\left[N \ln\left(\frac{N}{\Gamma_\infty A}\right) + (\Gamma_\infty A - N)\ln\left(\frac{\Gamma_\infty A - N}{\Gamma_\infty A}\right)\right], \tag{2.14}$$

where μ_s^0 is the chemical potential at half maximum packing ($\Gamma_\infty/2$). As with the ideal gas, (2.14) omits all interactions between surfactants, but instead accounts only for the free energy of mixing of both the occupied and unoccupied sites.

Computing surface pressure using (2.10) for the lattice gas (2.14) gives the so-called *Langmuir isotherm*,

$$\Pi^{\mathrm{L}} = k_B T \Gamma_\infty \ln\left(\frac{1}{1-\Gamma/\Gamma_\infty}\right). \tag{2.15}$$

At low surfactant concentrations $\Gamma \ll \Gamma_\infty$, Π^{L} reduces to Π^{ideal}. As surfactant concentration Γ approaches Γ_∞, however, the surface pressure diverges.

Rather than constraining surfactants to a lattice, surfactants with finite size might simply reduce the area available for surfactants to explore. Placing N surfactants, each of area $A_0 \equiv 1/\Gamma_\infty$, onto a surface of area A leaves an unoccupied area $A' = A - N/\Gamma_\infty$. Replacing A in the ideal gas expression $\mathcal{F}_s^{\mathrm{ideal}}$ with A',

$$\mathcal{F}_s^{\mathrm{V}} = N\mu_s^0 + k_B T\left[N\ln\left(\frac{N}{\Gamma_\infty A - N}\right) - N\right], \tag{2.16}$$

gives the *Volmer isotherm*,

$$\Pi^{\mathrm{V}} = \frac{k_B T \Gamma}{1-\Gamma/\Gamma_\infty}. \tag{2.17}$$

Like the Langmuir isotherm, the Volmer pressure recovers the ideal gas pressure as $\Gamma \ll \Gamma_\infty$, and diverges as $\Gamma \to \Gamma_\infty$, but in a different way than Π^{L}.

One might think it would be straightforward to distinguish between the Langmuir and Volmer forms for the divergence, but interactions between surfactants become significant and alter this form considerably.

The simplest way to include interactions between surfactants is perturbatively, i.e., adding a term to either the Langmuir (2.14) or Volmer (2.16) expressions

$$\Delta\mathcal{F}_s^{\mathrm{int}} = -N\frac{\beta}{2}\Gamma \tag{2.18}$$

that *reduces* the free energy to assemble a monolayer of mutually *attractive* surfactants (when $\beta > 0$), or vice-versa for repulsive interactions. For example, adding (2.18) to the Volmer free energy $\mathcal{F}_s^{\mathrm{V}}$ gives the *van der Waals* monolayer,

$$\mathcal{F}_s^{\mathrm{vdW}} = N\mu_s^0 + k_B T\left[N\ln\left(\frac{N}{\Gamma_\infty A - N}\right) - N\right] - \beta\frac{N^2}{2A}, \tag{2.19}$$

with surface pressure

$$\Pi^{\mathrm{vdW}} = \frac{k_B T \Gamma}{1 - \Gamma/\Gamma_\infty} - \beta \frac{\Gamma^2}{2}. \tag{2.20}$$

Equation (2.20) is the precise two-dimensional analog of the 3D van der Waals equation of state. Similarly, adding the interaction term (2.18) to the Langmuir surface free energy $\mathscr{F}_s^{\mathrm{L}}$ (2.14) gives the *Frumkin* isotherm (see table 1). Kralchevsky *et al.* (2008) provide a detailed thermodynamic derivation of each of these commonly used models, the results of which are summarized in table 1 and illustrated in figure 5.

2.3.1. Compressibility: Gibbs (E) and Marangoni (E_0) moduli—The surface compressional (or dilatational) modulus,

$$E = -A\frac{\partial \Pi}{\partial A}, \tag{2.21}$$

measures the resistance of the surface to compression, completely analogous to 3D materials. For insoluble surfactants, the number of surfactants in a monolayer does not change during compression, meaning A can be replaced with N/Γ in (2.21) to give the insoluble dilatational modulus:

$$E_0 = \Gamma \frac{\partial \Pi}{\partial \Gamma}\bigg|_N. \tag{2.22}$$

The nomenclature of (2.21) and (2.22) varies across the surfactant literature, with the names of Gibbs, Marangoni, Gibbs-Marangoni, or simply dilatational modulus used for both E and E_0. For the purposes of this review, we will consistently call E the Gibbs modulus and E_0 the Marangoni modulus.

The Marangoni modulus E_0 measures the work done in squeezing surfactant molecules together, and generally increases with surfactant concentration. For example, ideal gas monolayers have Marangoni modulus

$$E_0^{\mathrm{ideal}} = k_B T \Gamma, \tag{2.23}$$

with expressions for other isotherms given in table 1. Notably, the Marangoni modulus for the van der Waals isotherm,

$$E_0^{\mathrm{vdW}} = \frac{k_B T \Gamma}{(1 - \Gamma/\Gamma_\infty)^2} - \beta \Gamma^2, \tag{2.24}$$

becomes *negative* for a range of Γ whenever $\beta\Gamma_\infty/k_BT > 27/4$. Just like in 3D, a monolayer with negative compressibility is mechanically unstable, and undergoes phase separation to a two-phase coexistence between a high-Γ condensed phase, and a low-Γ expanded phase.

In what follows (§2.4.2 and §3.2), we will find that monolayers (soluble or insoluble) do not always react instantaneously following compression – finite time scales are required for phase transitions to occur, for surfactants to adsorb or desorb to equilibrate with the

surrounding bulk fluid, or for surfactant gradients in the surroundings to diffusively relax. In this regard, the Marangoni modulus E_0 reflects an intrinsic material property, whereas the Gibbs modulus E describes the dynamic response of a macroscopic interface, which additionally depends on the shape, size, and time scales of the forcing.

2.3.2. The chemical potential—In preparation for the upcoming transition to *soluble* surfactants, we discuss one final thermodynamic property of Langmuir monolayers. The chemical potential represents the free energy cost of adding one additional molecule to the monolayer, holding temperature and area constant:

$$\mu_s(\Gamma) = \left.\frac{\partial \mathcal{F}_s}{\partial N}\right|_{T,A}. \tag{2.25}$$

The chemical potential of a monolayer of ideal surfactants – as described by (2.8) – is

$$\mu_s^{\text{ideal}}(N) = \mu_s^0 + k_B T \ln\left(\frac{N}{\Gamma_0 A}\right), \tag{2.26}$$

or, equivalently,

$$\mu_s^{\text{ideal}}(\Gamma) = \mu_s^0 + k_B T \ln\left(\frac{\Gamma}{\Gamma_0}\right). \tag{2.27}$$

where μ_s^0 is a reference chemical potential, valid at a particular concentration Γ_0. In what follows, we will frequently use the Langmuir (lattice) isotherm as a model; its chemical potential is

$$\mu_s^{\text{L}}(\Gamma) = \mu_s^0 + k_B T \ln\left(\frac{\Gamma}{\Gamma_\infty - \Gamma}\right). \tag{2.28}$$

where μ_s^0 is the chemical potential at $\Gamma = \Gamma_\infty/2$.

2.4. Soluble surfactants: Gibbs monolayers

We now turn to *soluble* surfactants, which can dissolve into the liquid below the interface. Monolayers of soluble surfactants – called *Gibbs monolayers* – represent an equilibrium between surfactants adsorbed at the interface (with surface concentration Γ) and those dissolved in the bulk (with concentration C).

Detailed balance must hold for adsorbed and dissolved surfactants to be in equilibrium: as many surfactants must adsorb to a surface as desorb in any given time. For this to happen spontaneously, the two states must be equivalent from a free energy standpoint. Adding one surfactant to the monolayer costs energy – the chemical potential $\mu_s(\Gamma)$ of the adsorbed surfactant. This free energy cost must be *identical* to the free energy liberated by removing that surfactant from the subphase – represented by the chemical potential $\mu_b(C)$ of the surfactant in the bulk. In short, equilibrium between dissolved and adsorbed surfactant requires

$$\mu_s(\Gamma) = \mu_b(C), \tag{2.29}$$

which defines the equilibrium isotherm $\Gamma(C)$.

For example, surfactants that are sufficiently dilute in solution have 'ideal' chemical potential

$$\mu_b = \mu_b^0 + k_B T \ln\left(\frac{C}{C_0}\right), \tag{2.30}$$

where μ_b^0 is the chemical potential at a reference concentration C_0.

If adsorbed surfactants also form an ideal gas monolayer, with μ_s given by (2.27), then equating chemical potentials (2.29) reveals a linear relation between adsorbed and bulk concentrations:

$$\Gamma^{\text{ideal}} = \left(\frac{\Gamma_0}{C_0}\right)\exp\left(\frac{\mu_b^0 - \mu_s^0}{k_B T}\right)C, \tag{2.31}$$

or

$$\Gamma^{\text{ideal}} = K^{\text{ideal}} C, \tag{2.32}$$

which is called the Henry isotherm (table 1. Here

$$K^{\text{ideal}} = \left(\frac{\Gamma_0}{C_0}\right)\exp\left(\frac{\mu_b^0 - \mu_s^0}{k_B T}\right) \tag{2.33}$$

is an equilibrium constant for adsorption. The adsorption free energy $\Delta\mu_{\text{ads}}^0 = \mu_b^0 - \mu_s^0$ indicates the drop in free energy when a surfactant (at reference concentrations) adsorbs to the interface. As expected from statistical mechanics, the equilibrium constant K grows exponentially with $\Delta\mu_{\text{ads}}^0$. Different choices of either reference concentration (Γ_0 or C_0), both of which are chosen arbitrarily, would change the corresponding reference chemical potentials (μ_s^0 or μ_b^0, respectively), giving the same adsorption constant K.

Given $\Gamma(C)$ for a Gibbs monolayer of soluble surfactant, other monolayer properties like $\Pi(C)$ and $E_0(C)$ can be determined following the thermodynamic arguments for the insoluble surfactants given above. Surface pressure Π is still defined from the surface free energy via (2.10), so that the Gibbs monolayer defined by (2.32) has

$$\Pi^{\text{ideal}} = k_B T K^{\text{ideal}} C, \tag{2.34}$$

with K^{ideal} defined by (2.33). The Marangoni modulus, defined by (2.22), is also $E_0^{\text{ideal}} = k_B T K^{\text{ideal}} C$.

More complex isotherms arise for more complex monolayers or solutions. For example, soluble surfactants that adsorb to Langmuir (lattice) monolayers have surface chemical potentials of the Langmuir form (2.28), and equilibrate with an ideal bulk solution of surfactant (2.30) to give

$$\frac{\Gamma^L}{\Gamma_\infty} = \frac{K^L C}{1 + K^L C}, \tag{2.35}$$

where

$$K^{\mathrm{L}} = \left(\frac{1}{C_0}\right)\exp\left(\frac{\mu_b^0 - \mu_s^0}{k_B T}\right) \tag{2.36}$$

is the equilibrium constant for Langmuir adsorption, with units of [concentration]$^{-1}$. The surface pressure for the Langmuir isotherm then follows by inserting Γ^L from (2.35) into $\Pi^L(\Gamma)$ from (2.15) to give

$$\Pi^{\mathrm{L}}(C) = k_B T \Gamma_\infty \log\left(1 + K^L C\right), \tag{2.37}$$

The desorption constant, $K_D^L = \left(K^L\right)^{-1}$, represents a characteristic subphase concentration, at which the interface is half-saturated. The Langmuir adsorption isotherm (2.35) reduces to the ideal gas isotherm (2.34) for concentrations significantly below K_D^L (*i.e.* $C \ll 1/K^L$). Similar to insoluble monolayers, adding an interaction term to the surface chemical potential of the Langmuir form gives the Frumkin isotherm. Other models of monolayers that equilibrate with ideal surfactant solutions are reviewed by Kralchevsky *et al.* (2008), summarized in table 1, and illustrated in figure 5. All but the (purely empirical) Freundlich isotherm reduce to ideal gas monolayers at sufficiently low C.

Alternatively, surfactants dissolved in solution may show non-ideal behavior. The most common example is micellization: above a critical micelle concentration (CMC), some surfactants spontaneously aggregate to form micelles. Spherical micelles are most common, but cylinders ('wormlike micelles'), lamellae and vesicles can also form, depending on molecular morphology and intermolecular forces (Myers 2006; Israelachvili 2011). The energetics, kinetics, and morphology of micelles is a broad and well-studied topic that is beyond the scope of this review. We will merely point out that at equilibrium and above the CMC, the chemical potential of surfactant monomers, $\mu_b(C)$, must equal the chemical potential of surfactant molecules in micelles, $\mu_{\mathrm{mic}}(C)$, both of which in turn must equal the chemical potential $\mu_s(\Gamma)$ of adsorbed surfactant molecules. In other words, micellization provides an energetic alternative to further interfacial adsorption: once conditions favor micelle formation, adding further surfactant to solution tends to form additional micelles, rather than increase interfacial concentration. Indeed, identifying the bulk concentration at which the surface tension, and ostensibly the surface concentration, becomes approximately constant is a common method for measuring the CMC.

2.4.1. Gibbs Isotherm—It is frequently difficult to *measure* the surface concentration Γ of soluble surfactants; more common is to measure surface pressure Π (or, equivalently, surface tension γ) as a function of subphase concentration C. In such cases, the Gibbs adsorption isotherm allows Γ to be derived from measured $\Pi(C)$ relations (Martínez-Balbuena *et al.* 2017). The Gibbs relation connects changes in surface pressure Π to changes in the chemical potential μ_s of adsorbed surfactants at concentration Γ, via (Adamson 1990; Myers 2006; Kralchevsky *et al.* 2008):

$$\mathrm{d}\Pi = -\mathrm{d}\gamma = \Gamma \mathrm{d}\mu_s . \tag{2.38}$$

The chemical potential of adsorbed surfactants μ_s is difficult to determine directly since Γ is unknown for soluble surfactants. However, when bulk and adsorbed surfactants are equilibrated, μ_s must be equal to μ_b for the dissolved surfactants. In cases where the surfactant solution is dilute enough to behave as ideal, $\mu_b(C)$ is given by (2.30), in which case

$$\mathrm{d}\mu = \mathrm{d}\mu_s = k_B T \mathrm{d}\ln C . \tag{2.39}$$

The Gibbs relation (2.38) then gives

$$\Gamma(C) = \frac{1}{k_B T} \frac{\partial \Pi}{\partial \ln C}\bigg|_T . \tag{2.40}$$

In other words, the adsorbed surfactant concentration Γ can be determined from measurements of surface pressure Π as a function of dissolved surfactant concentration C, so long as the system has equilibrated, and the concentration is well below the CMC (Martínez-Balbuena *et al.* 2017).

2.4.2. Compressibility: E and E_0 for soluble surfactants—The distinction between the Gibbs and Marangoni moduli, E and E_0, defined by (2.21) and (2.22) respectively, becomes significant for soluble monolayers. Recall that E tracks surface pressure changes when the monolayer area A is changed, whereas E_0 *additionally* holds the number N of adsorbed surfactant molecules fixed – meaning Γ changes when A does. Compressing monolayers of soluble surfactants raises the chemical potential μ_s of the adsorbed surfactants, without changing the concentration or chemical potential $\mu_b(C)$ of the dissolved surfactant. A thermodynamic force drives adsorbed surfactants to desorb, until Γ returns to the value predicted by (2.29). Once equilibrium is re-established, Γ returns to its initial value, so that

$$E^{\mathrm{soluble}}(t \to \infty) = -A \frac{\partial \Pi}{\partial A}\bigg|_{t \to \infty} = 0. \tag{2.41}$$

How quickly the interface re-equilibrates cannot be determined from thermodynamic properties alone, as discussed in §3.2.

Soluble surfactant monolayers do have a non-zero Marangoni modulus E_0, however. After all, Γ (and therefore Π) must increase during a rapid compression of a Gibbs monolayer,

before the surfactants have had the chance to desorb. The Gibbs adsorption equation (2.40), however, offers a route to E_0 for soluble surfactant monolayers from measured $\Pi(C)$ isotherms:

$$E_0 = \Gamma \frac{\partial \Pi}{\partial \Gamma} = \Gamma \frac{\partial \Pi}{\partial \ln C} \frac{\partial \ln C}{\partial \Gamma}. \tag{2.42}$$

Substituting Γ and $\partial\Gamma/\partial \ln C$ using (2.40) gives

$$E_0 = \frac{(\Pi')^2}{\Pi''}, \quad \text{or} \quad \frac{1}{E_0} = -\left(\frac{1}{\Pi'}\right)', \tag{2.43}$$

where primes denote differentiation with respect to ln C.

While the Gibbs modulus E describes the monolayer's mechanical response to macroscopic compression or expansion (dA), the Marangoni modulus E_0 reflects sensitivity to intrinsic molecular concentrations Γ, and will play an important role in establishing an effective surface dilatational viscosity for surfactant monolayers, as shown in §4.2.

2.4.3. Soluble isotherms via dynamic equilibrium—Equilibrium between surfactants adsorbed at an interface and dissolved in the subphase can also be determined by explicitly balancing adsorption and desorption fluxes. This approach holds particular value to the fluid mechanics community, as it connects the equilibrium arguments and measurements made above to Marangoni stresses and dynamical processes in surfactant systems.

The simplest expressions for adsorption and desorption fluxes – which one should expect to hold for ideal mixtures in both the monolayer and in the bulk – is to take the adsorption flux, j_a, to be proportional to the bulk concentration C, and the desorption flux j_d to be proportional to the adsorbed concentration Γ:

$$j_a = k_a C, \tag{2.44}$$

$$j_d = k_d \Gamma. \tag{2.45}$$

These fluxes balance at equilibrium, $j_a = j_d$, giving

$$\Gamma^{\text{ideal}} = \frac{k_a}{k_d} C \equiv K^{\text{ideal}} C, \tag{2.46}$$

reproducing the Henry isotherm (2.32). Previously, the adsorption constant K^{ideal} was shown to depend upon the free energy of adsorption $\Delta\mu = \mu_b^0 - \mu_s^0$ via (2.33). Eq. (2.46) additionally relates K^{ideal} to the ratio of adsorptive to desorptive rate constants k_a/k_d. Each individual rate constant k_a and k_d can *not* be determined from an equilibrium quantity like K; however, the ratio of the two is set by thermodynamics.

Other isotherms require different adsorption and/or desorption rate kinetics. For example, the Langmuir isotherm (2.35) is formed when dissolved surfactants adsorb to *vacant* lattice sites (Levich 1962; Adamson 1990; Kralchevsky *et al.* 2008), modifying the adsorption flux (2.44) to

$$j_a^L = k_a C(\Gamma_\infty - \Gamma). \tag{2.47}$$

At equilibrium, $j_a^L = j_d$, so that

$$\frac{k_a C}{k_d} = \frac{\Gamma^L}{\Gamma_\infty - \Gamma^L}, \tag{2.48}$$

recovering (2.35) with $K = k_a/k_d$. Adsorption and desorption fluxes for other common isotherms are listed in table 2.

This dynamic equilibrium approach forms a natural transition into §3, which addresses the dynamic response of surfactant-laden interfaces when they are driven out of equilibrium. Specifically, we will describe how fluid flow transports surfactant molecules in the bulk and on the interface, and how the tendency of surfactant molecules to re-equilibrate in turn impacts interfacial fluid dynamics.

3. Dynamic Properties

So far, we have assumed that interfacial deformations have been ‘slow enough,’ or that we have waited long enough, that the surfactants have remained in quasi-steady equilibrium, instantaneously redistributing and/or adsorbing and desorbing to equilibrate with the bulk liquid beneath them. However, these processes take time. Various *dynamic* surfactant processes arise in systems driven out of equilibrium, modifying the behavior of even the simplest systems. Figure 1, for example, highlights the dynamic surfactant processes that impact a rising gas bubble. Convective flow along the fluid interface sweeps surfactants to the rear as the bubble rises. The resulting concentration gradients generate Marangoni stresses that act to oppose the motion that created them. Surface diffusion smooths out non-uniform distributions of surface concentration, as does surfactant exchange with the bulk, thereby reducing the strength of Marangoni flows. Additionally, surface excess rheological stresses might arise as insoluble surfactant monolayers are sheared or compressed.

Interpreting, predicting, and engineering these surfactant systems then necessitates a thorough understanding of the interplay between physically distinct transport processes. Our objective in this section is to provide an introduction to the physics and the mathematical machinery that govern the out-of-equilibrium behavior of surfactant systems. We will start with the governing equations of surfactant transport (§3.1), discuss the competition between diffusion- and adsorption/desorption kinetics in surfactant exchange between bulk and adsorbed states (§3.2), outline the origins of Marangoni stresses and characterize its strength relative to other processes (§3.3), and finally describe the fluid mechanics of systems with a non-zero surface excess viscosities (§3.4).

3.1. Governing equations

Our discussion thus far has centered on the equilibrium properties of surfactants. Of particular interest to the fluid dynamics community, on the other hand, is the coupling between the surfactants and the fluids surrounding the interface. Conservation equations for the mass and momentum of the bulk fluid are well-known,

$$\rho \frac{\mathrm{D}\boldsymbol{v}}{\mathrm{D}t} = -\boldsymbol{\nabla} p + \eta \nabla^2 \boldsymbol{v}, \tag{3.1a}$$

$$\boldsymbol{\nabla} \cdot \boldsymbol{v} = 0, \tag{3.1b}$$

with ρ the fluid density, η the shear viscosity, $\boldsymbol{v}$ the fluid velocity, and p the pressure.

At first glance, boundary conditions seem to be fairly straightforward. The kinematic boundary condition relates the fluid velocity *normal* to an interface to the deformation velocity of that interface (Leal 2007): a fluid interface located at $\boldsymbol{r}_s(t)$ is defined by

$$\Phi(\boldsymbol{r}_s, t) = 0, \tag{3.2}$$

with unit normal

$$\boldsymbol{n} = \left. \frac{\boldsymbol{\nabla}\Phi}{|\boldsymbol{\nabla}\Phi|} \right|_{\boldsymbol{r}_s}, \tag{3.3}$$

and requires

$$\boldsymbol{n} \cdot \boldsymbol{v}(\boldsymbol{r}_s) = -\left. \frac{1}{|\boldsymbol{\nabla}\Phi|} \frac{\partial \Phi}{\partial t} \right|_{\boldsymbol{r}_s}. \tag{3.4}$$

Likewise, the fluid velocity at the interface, $\boldsymbol{u}$, generally obeys the no-slip condition:

$$\boldsymbol{u}(\boldsymbol{r}_s) = \boldsymbol{v}(\boldsymbol{r}_s). \tag{3.5}$$

In general, the stress boundary condition is more complicated. Conservation of momentum at the interface gives (Slattery *et al.* 2007)

$$\rho_s \frac{\mathrm{D}\boldsymbol{u}}{\mathrm{D}t} = \boldsymbol{n} \cdot [\![\boldsymbol{\sigma}]\!] + \boldsymbol{\nabla}_s \cdot \boldsymbol{\sigma}_s, \tag{3.6}$$

where ρ_s is the surface mass density, $[\![\boldsymbol{\sigma}]\!] = \boldsymbol{\sigma}_{\text{upper}} - \boldsymbol{\sigma}_{\text{lower}}$ is the hydrodynamic stress jump across the interface with $\boldsymbol{n}$ pointing into the 'upper' fluid, and $\boldsymbol{\nabla}_s = (\boldsymbol{I} - \boldsymbol{nn}) \cdot \boldsymbol{\nabla}$ is the surface gradient operator. The *surface stress* tensor is

$$\boldsymbol{\sigma}_s = \gamma \boldsymbol{I}_s + \boldsymbol{\tau}_{\text{rheol}} \tag{3.7}$$

where γ is the local surface tension, $\boldsymbol{I}_s = \boldsymbol{I} - \boldsymbol{nn}$ is the surface identity tensor, and we have included surface rheological stresses $\boldsymbol{\tau}_{\text{rheol}}$ in anticipation, but defer detailed discussion to §3.4.

Neglecting fluid and surfactant inertia, the interfacial stress balance (3.6) becomes

$$-\boldsymbol{n} \cdot \llbracket \boldsymbol{\sigma} \rrbracket = \boldsymbol{\nabla}_s \gamma - \gamma(\boldsymbol{\nabla}_s \cdot \boldsymbol{n})\boldsymbol{n} + \boldsymbol{\nabla}_s \cdot \boldsymbol{\tau}_{\text{rheol}}. \tag{3.8}$$

The tangential component of (3.8) reveals that imbalances between viscous shear stress can be driven by (or balance) both Marangoni stresses (§3.3) and surface rheological stresses (§3.4). The normal component of (3.8) reduces to the Young-Laplace equation (2.6) in a static system ($\boldsymbol{\sigma} = -p\boldsymbol{I}$) if surface rheological stresses are absent.

The interfacial stress boundary condition (3.8) depends on the surface tension γ (or surface pressure Π), which in turn depends on adsorbed surfactant concentration $\Gamma(\boldsymbol{r}_s, t)$ via some isotherm, as described in §2.3. Still, the concentration profile of adsorbed surfactant Γ changes in space and time, and must therefore be determined. To do so requires addressing *dynamic* questions of surfactant transport: convective and diffusive transport along the interface, adsorption and desorption of surfactant between the interface and the bulk solution(s).

Adsorbed surfactant evolves according to a conservation equation,

$$\frac{\partial \Gamma}{\partial t} = -\boldsymbol{\nabla}_s \cdot (\boldsymbol{j}_D + \boldsymbol{u}\Gamma) + j_n, \tag{3.9}$$

where $\boldsymbol{j}_D$ represents the diffusive flux along the interface, and $\boldsymbol{u}\Gamma$ represents the surface advective flux. The final term j_n accounts for the local 'production' or 'consumption' of adsorbed surfactant, typically driven by adsorptive and desorptive exchange between the bulk solution and the interface. If more surfactant adsorbs to a spot on the interface than desorbs from that spot, then Γ grows (and $j_n > 0$) at that spot.

A common form of this equation, as formally derived by Aris (1962) and Stone (1990), assumes constant surface diffusivity D_s, and reads

$$\frac{\partial \Gamma}{\partial t} + \boldsymbol{\nabla}_s \cdot (\Gamma \boldsymbol{u}_s) + \Gamma(\boldsymbol{\nabla}_s \cdot \boldsymbol{n})(\boldsymbol{u} \cdot \boldsymbol{n}) = D_s \nabla_s^2 \Gamma + j_n, \tag{3.10}$$

where $\boldsymbol{u}_s$ is the in-plane surface velocity:

$$\boldsymbol{u}_s = (\boldsymbol{I} - \boldsymbol{nn}) \cdot \boldsymbol{v}(\boldsymbol{r}_s) = (\boldsymbol{I} - \boldsymbol{nn}) \cdot \boldsymbol{u}. \tag{3.11}$$

In what follows, we will discuss subtleties and assumptions built into this expression, as well as generalizations.

3.1.1. Surface advection—The surface advective flux can be decomposed into components *normal* to the interface, and components *along* the interface:

$$\boldsymbol{u}\Gamma = \boldsymbol{n}(\boldsymbol{n}\cdot\boldsymbol{u})\Gamma + (\boldsymbol{I}-\boldsymbol{n}\boldsymbol{n})\cdot\boldsymbol{u}\Gamma, \tag{3.12}$$

and therefore has surface divergence

$$\nabla_s\cdot(\boldsymbol{u}\Gamma) = \Gamma(\nabla_s\cdot\boldsymbol{n})(\boldsymbol{u}\cdot\boldsymbol{n}) + \nabla_s\cdot(\boldsymbol{u}_s\Gamma) \tag{3.13}$$

as in (3.10). The first term captures the compression or dilation of surfactant that occurs when curved interfaces ($\nabla_s\cdot\boldsymbol{n}\neq 0$) themselves deform (due to non-zero normal interfacial velocities), and the second term captures the compression or dilation arising from non-uniform convective flux *within* the plane of the interface.

3.1.2. Surface diffusion—The standard expression for the diffusive flux of adsorbed surfactant along a surface, used to derive (3.10), has a Fickian form,

$$\boldsymbol{j}_D^{\text{Fick}} = -D_s\nabla_s\Gamma, \tag{3.14}$$

A diffusive flux of this form, however, is built on assumptions that are rarely accurate in systems of practical interest.

A brief derivation of the diffusive flux highlights conditions under which the Fickian form holds. Because the chemical potential $\mu(\Gamma,T)$ represents the free energy 'cost' of an adsorbed surfactant at concentration Γ and temperature T, any spatial gradients in μ point toward more 'costly' locations for surfactants to be placed. A chemical potential gradient thus represents a thermodynamic force ($\boldsymbol{f}_s=-\nabla_s\mu$) on an adsorbed surfactant, which drives it to migrate along the interface, with relative velocity

$$\boldsymbol{V}-\boldsymbol{u}_s = -b_s\nabla_s\mu = -\frac{D_s}{k_BT}\nabla_s\mu, \tag{3.15}$$

where b_s is the hydrodynamic mobility of the surfactant along the surface, and is related to its self-diffusivity by the Stokes-Einstein relation (Furst & Squires 2017; Saffman & Delbrück 1975)

$$D_s = k_BTb_s\,. \tag{3.16}$$

Each surfactant molecule moves with velocity (3.15) along the surface, so that a *single-component* monolayer of surface concentration Γ establishes a flux

$$\boldsymbol{j}_D = -\frac{D_s}{k_BT}\Gamma\nabla_s\mu = -\left(\frac{D_s}{k_BT}\Gamma\frac{\partial\mu}{\partial\Gamma}\right)\nabla_s\Gamma \tag{3.17}$$

relative to the interface. In *multi-component* monolayers, the chemical potential of each species depends on the surface concentration of every other component, and the term in brackets in (3.17) is replaced by a generalized Maxwell-Stefan diffusivity tensor (Krishna 1990). In what follows, we restrict our discussion to single-component monolayers.

The Fickian form (3.14) holds only for the ideal gas monolayer, for which $\mu = \mu_s^{\text{ideal}}(\Gamma)$ from (2.27), and therefore

$$\frac{\partial \mu_s^{\text{ideal}}}{\partial \Gamma} = \frac{k_B T}{\Gamma}, \tag{3.18}$$

so that the diffusive flux (3.17) reduces to Fick's law (3.14). As discussed in §2.3, however, it is rare for any surfactant that reduces surface tension in any appreciable way to behave as an ideal gas. The Fickian form, then, rarely holds as explicitly derived. Of course, one can define an effective diffusivity

$$D_s^{\text{eff}}(\Gamma) = \frac{D_s}{k_B T} \Gamma \frac{\partial \mu}{\partial \Gamma}, \tag{3.19}$$

which differs from the true self-diffusivity of each surfactant molecule. If gradients are small enough that D_s^{eff} is approximately constant, then the Fickian form would be appropriate, albeit with a modified diffusivity.

The effective surface diffusivity D_s^{eff} can be shown using (2.22) and (2.23) to exceed the Fickian self-diffusivity by the Marangoni modulus $E_0(\Gamma)$ relative to an ideal gas monolayer:

$$\boldsymbol{j}_D = -D_s \frac{E_0(\Gamma)}{k_B T \Gamma} \boldsymbol{\nabla}_s \Gamma \equiv -D_s \frac{E_0(\Gamma)}{E_0^{\text{ideal}}} \boldsymbol{\nabla}_s \Gamma . \tag{3.20}$$

The diffusive flux expressions for the Langmuir and Volmer isotherms (table 1), for example, become

$$\boldsymbol{j}_D^L = -\frac{D_s}{1 - \Gamma/\Gamma_\infty} \boldsymbol{\nabla}_s \Gamma, \quad \text{and} \quad \boldsymbol{j}_D^V = -\frac{D_s}{(1 - \Gamma/\Gamma_\infty)^2} \boldsymbol{\nabla}_s \Gamma . \tag{3.21}$$

Curiously, the diffusive flux of adsorbed surfactant within single-component monolayers can be expressed in terms of surface pressure gradients alone. The Gibbs adsorption relation (2.38) directly implies

$$\Gamma \boldsymbol{\nabla}_s \mu = \boldsymbol{\nabla}_s \Pi, \tag{3.22}$$

which can be substituted for $\Gamma \boldsymbol{\nabla}_s \mu$ in (3.17) to give a diffusive flux

$$\boldsymbol{j}_D = -b_s \boldsymbol{\nabla}_s \Pi . \tag{3.23}$$

which appears to be independent of the surface concentration Γ! Although this result seems counter-intuitive at first, it can be understood physically as follows. The surface pressure gradient gives the force *per unit area* exerted on the surfactant monolayer, which is divided among Γ molecules per unit area. The greater the concentration Γ of adsorbed surfactant, the weaker the force on each ($\boldsymbol{F}_s \sim \boldsymbol{\nabla} \Pi / \Gamma$), and the slower each migrates: $\boldsymbol{V} \sim b_s (\boldsymbol{\nabla}_s \Pi / \Gamma)$. Ultimately, the concentration Γ cancels out of the flux $\Gamma \boldsymbol{V}$ in (3.23).

3.2. Adsorption/desorption

The final term in the surfactant conservation equation, j_n, accounts for exchange of molecules between the bulk and the interface. At equilibrium, adsorption and desorption fluxes balance each other (§2.4.3). For an interface out of equilibrium, the difference between j_a and j_d represents a kinetic flux of surfactant entering or leaving the interface:

$$j_{\text{kin}} = j_a(\Gamma, C_s) - j_d(\Gamma, C_s), \tag{3.24}$$

where

$$C_s = C(\boldsymbol{r}_s, t) \tag{3.25}$$

is the surfactant concentration in the bulk fluid, evaluated at the interface (figure 6 *e*). Table 2 gives j_a and j_d corresponding to the common isotherms described in § 2.3 and table 1.

Departures from a constant equilibrium concentration C_0 also drive surfactant transport in the bulk, governed by the convection-diffusion equation

$$\frac{\partial C}{\partial t} = D\nabla^2 C - \boldsymbol{v} \cdot \boldsymbol{\nabla} C\,. \tag{3.26}$$

Concentration gradients in the bulk may drive a diffusive flux of surfactants onto or off the interface, via

$$j_{\text{diff}} = D\boldsymbol{n} \cdot \boldsymbol{\nabla} C|_{\boldsymbol{r}_s}, \tag{3.27}$$

where $\boldsymbol{n}$ is normal to the interface and points into the bulk fluid containing the surfactant. Surfactant conservation requires this diffusive flux (3.27) to balance the kinetic flux of adsorption/desorption to the interface (3.24), both of which equal the source term in the surface conservation equation (3.10):

$$j_n = j_{\text{kin}} = j_{\text{diff}}\,. \tag{3.28}$$

If either adsorption kinetics or diffusion is so slow as to act as the rate-limiting step, then the surfactant exchange flux j_n may be approximated by that process alone. In diffusion-limited adsorption, for example, the timescale τ_k associated with adsorption kinetics is negligibly short compared to the timescale τ_d for diffusion from the bulk. In that limit, the concentrations $\Gamma(\boldsymbol{r}_s, t)$ and $C(\boldsymbol{r}_s, t)$ of adsorbed and bulk surfactant are assumed to equilibrate instantaneously, so that j_{kin} is ignored and diffusion-limited adsorption is governed by (3.26)–(3.27) alone. By contrast, adsorption is kinetically-limited when $\tau_d \ll \tau_k$, in which case diffusion smooths bulk concentration gradients instantly, so that $C_s(t) \approx C_0$ and adsorption is governed by (3.24) alone.

In what follows, we examine dynamic adsorption in a model system that is particularly illustrative and relatively straightforward: surfactant dynamics on the interface of an oscillating gas bubble (Lucassen & van den Tempel 1972; Johnson & Stebe 1994; Ravera *et*

al. 2010; Kotula & Anna 2016). Beyond its pedagogic value, pulsing bubbles form the basis for a powerful experimental technique to characterize complex fluid interfaces.

3.2.1. Adsorption/desorption to an oscillating bubble—Here we adapt the work of Johnson & Stebe (1994), who considered oscillations of a bubble with rest radius R_0 and equilibrium surface concentration Γ_0 in a liquid containing dissolved surfactant at concentration C_0 (figure 7). The bubble radius changes in response to a controlled oscillation of gas volume or pressure. Assuming departures from equilibrium to be small, the radius, surface concentration and bulk concentration are perturbed via

$$R(t) = R_0 + \delta R e^{i\omega t}, \quad \Gamma(t) = \Gamma_0 + \delta\Gamma e^{i\omega t}, \quad C(r,t) = C_0 + \delta C(r) e^{i\omega t}. \tag{3.29}$$

The surfactant conservation equation (3.10) for purely radial oscillations becomes

$$\frac{\partial \Gamma}{\partial t} + \frac{2u_r\Gamma}{R} = j_n, \tag{3.30}$$

where $u_r = \mathrm{d}R/\mathrm{d}t$ is the radial velocity at the interface. Perturbing (3.30) via (3.29) gives

$$\left[i\omega\delta\Gamma + i\omega\delta R\frac{2\Gamma_0}{R_0}\right]e^{i\omega t} = j_n. \tag{3.31}$$

In systems where the surfactant is insoluble (for which $j_n = 0$), the change in surface concentration is

$$\delta\Gamma_{\mathrm{insol}} = -\frac{2\Gamma_0}{R_0}\delta R. \tag{3.32}$$

We define C_s and δC_s as the bulk concentration and the amplitude of its oscillatory perturbation at the interface:

$$C_s(t) = C(R,t), \quad \text{and} \quad \delta C_s = \delta C(R). \tag{3.33}$$

Because the convective term in the bulk transport equation (3.26) is quadratic in perturbed quantities, the bulk concentration C obeys the diffusion equation to leading order, with solution

$$C(r,t) = C_0 + \delta C_s \frac{R}{r} e^{\sqrt{i\omega/D}(R-r)} e^{i\omega t}, \tag{3.34}$$

where δC_s is as yet unknown. The diffusive flux (3.27) onto the interface,

$$j_{\mathrm{diff}} = D\frac{\partial C}{\partial r}\bigg|_{R(t)} = D\delta C_s\left[-\frac{1}{R_0} - \sqrt{\frac{i\omega}{D}}\right]e^{i\omega t}, \tag{3.35}$$

must equal the kinetic flux j_{kin} (3.24), which is given to leading order by

$$j_{\text{kin}} = (k_C \delta C_s - k_\Gamma \delta\Gamma) e^{i\omega t}. \tag{3.36}$$

Here

$$k_C(C_0, \Gamma_0) = \left.\frac{\partial j_a}{\partial C}\right|_{\Gamma_0, C_0} - \left.\frac{\partial j_d}{\partial C}\right|_{\Gamma_0, C_0}, \tag{3.37a}$$

$$k_\Gamma(C_0, \Gamma_0) = \left.\frac{\partial j_a}{\partial \Gamma}\right|_{\Gamma_0, C_0} - \left.\frac{\partial j_d}{\partial \Gamma}\right|_{\Gamma_0, C_0} \tag{3.37b}$$

are effective rate constants associated with the equilibrium exchange fluxes (e.g. table 2). The ratio of k_C and k_Γ has units of length and is defined as the *depletion depth*:

$$L_d = \frac{k_C}{k_\Gamma}. \tag{3.38}$$

For example, the (linear) Henry isotherm (table 1) has $k_C = k_a$ and $k_\Gamma = k_d$, so that the depletion depth is a constant equal to the equilibrium adsorption constant: $L_d = K^{\text{ideal}}$.

Equating the diffusive (3.35) and kinetic fluxes (3.36) relates δC_s to $\delta\Gamma$:

$$\delta C_s = \frac{k_\Gamma R_0}{D + k_C R_0 + \sqrt{i\omega R_0^2 D}} \delta\Gamma = \frac{Da}{1 + Da + \sqrt{iWo}} \frac{\delta\Gamma}{L_d}, \tag{3.39}$$

where the mass transfer Womersley number Wo and Damköhler number Da are

$$Wo = \frac{\text{diffusion time}}{\text{oscillation period}} = \frac{\omega R_0^2}{D}, \tag{3.40a}$$

$$Da = \frac{\text{diffusion time}}{\text{adsorption time}} = \frac{k_C R_0}{D}. \tag{3.40b}$$

Then, using (3.39) in (3.35) or (3.36) to eliminate δC_s and determine j_n in terms of $\delta\Gamma$, and substituting into the surface conservation equation (3.31) reveals $\delta\Gamma$ to be

$$\frac{\delta\Gamma}{\delta\Gamma_{\text{insol}}} = \left[1 - i\,St\left(\frac{1 + \sqrt{iWo}}{1 + \sqrt{iWo} + Da}\right)\right]^{-1}, \tag{3.41}$$

where the Stanton number St is defined by

$$St = \frac{\text{oscillation period}}{\text{desorption time}} = \frac{k_\Gamma}{\omega}. \tag{3.42}$$

The Damköhler number controls the transition from kinetically-limited ($Da \ll 1$) to diffusion-limited ($Da \gg 1$) surfactant exchange. In what follows (§3.2.2–3.2.3), we consider

kinetically- and diffusion-controlled regimes separately. For later use, we rewrite the surfactant exchange flux, from (3.35) or (3.36), as

$$j_n = j_{\text{diff}} = j_{\text{kin}} = -\left[\frac{1+\sqrt{iW_O}}{1+\sqrt{iW_O}+Da}\right] k_\Gamma \delta\Gamma e^{i\omega t}. \tag{3.43}$$

3.2.2. Kinetically-limited mass transfer (Da ≪ 1)—Adsorption is kinetically-limited ($Da \ll 1$) when molecular exchange between the interface and the subsurface layer is significantly slower than surfactant diffusion through the bulk. In this limit, the subphase concentration is approximately uniform: (3.39) gives $\delta C_s \to 0$ as $Da \to 0$, implying $C_s(t) \approx C_0$ (figure 7 *e*).

Setting $Da = 0$ in (3.41) gives the perturbed surface concentration:

$$\frac{\delta\Gamma_{\text{kin}}}{\delta\Gamma_{\text{insol}}} = \frac{1}{1-iSt} = \frac{1}{1+St^2} + i\frac{St}{1+St^2}. \tag{3.44}$$

The $St \to 0$ limit corresponds to oscillations so rapid that surfactants do not have the times to adsorb or desorb, so that the monolayer behaves as if it were insoluble: $\delta\Gamma_{\text{kin}} \to \delta\Gamma_{\text{insol}}$. By contrast, the $St \to \infty$ limit occurs when surfactants adsorb/desorb much faster than bubble oscillations. In that case, $\delta\Gamma_{\text{kin}} \to 0$ and the interface maintains its equilibrium concentration $\Gamma(t) \approx \Gamma_0$.

Timescales for bubble oscillation and adsorption/desorption are comparable when $St \sim O(1)$, which defines the characteristic timescale for kinetically-limited adsorption,

$$\tau_k = \frac{1}{k_\Gamma}. \tag{3.45}$$

For finite τ_k (or finite St), $\delta\Gamma_{\text{kin}}$ is always smaller than $\delta\Gamma_{\text{insol}}$ (figure 8 *a*). Additionally, the surface concentration lags the bubble radius by a phase shift $\tan^{-1}(St)$.

When kinetically-limited ($Da \to 0$), the adsorption flux (3.43) becomes

$$j_n(Da \to 0) = -k_\Gamma \delta\Gamma e^{i\omega t} = \frac{\Gamma_0 - \Gamma(t)}{\tau_k}. \tag{3.46}$$

Throughout this work, we will use (3.46) as the kinetically-limited sorptive flux for small departures from equilibrium.

3.2.3. Diffusion-limited mass transfer (Da ≫ 1)—In diffusion-controlled surfactant exchange, adsorption kinetics are so fast that Γ equilibrates with the subsurface concentration C_s effectively instantaneously, via the appropriate isotherm $\Gamma(C_s)$ (figure 7 *d*). In this limit, j_{kin} can be ignored, so that $j_n = j_{\text{diff}}$. The depletion depth L_d follows by expanding $\Gamma(C_s)$ around $\Gamma_0(C_0)$, and taking the $Da \to \infty$ limit of (3.39) to give

$$\left.\frac{\partial \Gamma}{\partial C_s}\right|_{\Gamma_0, C_0} = \left.\frac{\delta \Gamma}{\delta C_s}\right|_{Da \to \infty} = L_d, \tag{3.47}$$

which we non-dimensionalize by the bubble radius R_0 to give

$$\Lambda_d = \frac{L_d}{R_0} = \frac{Da}{St\,Wo}. \tag{3.48}$$

The perturbed surface concentration (3.41) in the diffusion-controlled limit ($Da \to \infty$) is then

$$\frac{\delta \Gamma_{\text{diff}}}{\delta \Gamma_{\text{insol}}} = \frac{\Lambda_d W o}{\Lambda_d W_O - i - i\sqrt{i W_O}}, \tag{3.49}$$

which can be expressed as

$$\frac{\delta \Gamma_{\text{diff}}}{\delta \Gamma_{\text{insol}}} = \frac{1 + \zeta_d + i\zeta_d(1 + 2\Lambda_d \zeta_d)}{1 + 2\zeta_d + 2\zeta_d^2\left(1 + 2\Lambda_d \zeta_d + 2\Lambda_d^2 \zeta_d^2\right)}, \tag{3.50}$$

where

$$\zeta_d = \frac{1}{\Lambda_d}\sqrt{\frac{1}{2W_O}} = \frac{1}{L_d}\sqrt{\frac{D}{2\omega}} \tag{3.51}$$

is a dimensionless ratio of the diffusive oscillatory boundary layer thickness $\delta_{\text{BL}} = \sqrt{D/2\omega}$ to the depletion depth L_d.

Bubbles with radii much larger than the depletion depth ($\Lambda_d \ll 1$) behave like planar interfaces. Indeed, (3.50) recovers the celebrated results of Lucassen & van den Tempel (1972) in the $\Lambda_d \to 0$ limit, which we examine in detail in §4.2.1. Adsorbed surfactants on a planar interface ($\Lambda_d \to 0$) act as effectively insoluble if molecules in the subphase diffuse far less than the depletion depth in one oscillation ($\zeta_d \ll 1$). Conversely, the surface concentration remains close to its equilibrium value ($\delta\Gamma_{\text{diff}} \to 0$) if molecules diffusively escape L_d during an oscillation ($\zeta_d \gg 1$). Interfacial oscillations and diffusive mass transfer are comparable when $\zeta_d = O(1)$, which reveals the characteristic timescale for diffusion-limited mass transfer in the planar limit ($\Lambda_d \to 0$) to be

$$\tau_{d,\,p} = \tau_d(\Lambda_d \to 0) = \frac{L_d^2}{D}. \tag{3.52}$$

Diffusive mass transfer is sensitive to interfacial curvature when $\Lambda_d \gtrsim 1$, as shown in figure 8 *b*. The perturbed surface concentration $\delta\Gamma_{\text{diff}}$ still vanishes if diffusion is fast ($\zeta_d \gg 1$) and approaches the insoluble limit if diffusion is slow ($\zeta_d \ll 1$). However, the transition occurs around $\Lambda_d \zeta_d^2 = O(1)$, where

$$2\Lambda_d\zeta_d^2 = \frac{D/L_dR_0}{\omega} \sim \frac{\text{oscillation period}}{\text{diffusion time across } \sqrt{L_dR_0}}, \tag{3.53}$$

which reveals the characteristic time scale of diffusive-controlled surfactant exchange for small bubbles ($\Lambda_d \gtrsim 1$):

$$\tau_{d,s} = \tau_d(\Lambda_d \gtrsim 1) = \frac{L_dR_0}{D} = \frac{\tau_{d,p}}{\Lambda_d}. \tag{3.54}$$

Indeed, experiments and simulations show a smooth transition from $\tau_{d,p}$ to $\tau_{d,s}$ with decreasing bubble radius (Alvarez *et al.* 2010*a*, b).

Finally, the diffusion-limited surfactant exchange flux follows from the $Da \to \infty$ limit of (3.43). For small bubbles ($R_0^2 \ll D/\omega$, or $Wo \ll 1$), the net adsorption flux is

$$j_n(Da \to \infty) \approx -\frac{k_\Gamma}{Da}\delta\Gamma e^{i\omega t} = -\frac{D}{L_dR_0}\delta\Gamma e^{i\omega t} = \frac{\Gamma_0 - \Gamma(t)}{\tau_{d,s}}, \tag{3.55}$$

which has the same form as (3.46), but with the diffusion-controlled timescale $\tau_{d,s}$ in place of the kinetically-controlled timescale τ_k. For the same reasons, $\delta\Gamma_{\text{diff}}(\Lambda_d \gg 1)$ from (3.50) is identical to $\delta\Gamma_{\text{kin}}$ from (3.44) with $2\Lambda_d\zeta_d^2$ in place of St. In other words, diffusion-limited mass transfer to small bubbles 'looks like' it is kinetically-limited, albeit with a characteristic timescale $\tau_{d,s}$ that depends on the bubble radius via (3.54).

To summarize, the characteristic sorption time τ_s is

$$\tau_s = \begin{cases} \tau_k = 1/k_\Gamma, & Da \ll 1, \\ \tau_{d,p} = L_d^2/D, & Da \gg 1 \quad \& \quad R_0 \gg L_d, \\ \tau_{d,s} = L_dR_0/D, & Da \gg 1 \quad \& \quad R_0 \lesssim L_d. \end{cases} \tag{3.56}$$

In systems with dynamic interfaces, the mechanical response of a surface to deformation depends not only on the equilibrium properties of the surfactant (such as E_0, §2.3.1), but also on the adsorbed concentration profile $\Gamma(\boldsymbol{r}_s, t)$ at any particular position and time. In §4.2, we will again use the oscillating gas bubble example to quantify the apparent viscoelasticity of soluble monolayers, and its dependence on surfactant properties such as k_Γ, k_C, D, and E_0.

3.2.4. Adsorption to a clean interface—So far, we have discussed surfactant transport on interfaces that are perturbed only slightly from equilibrium. Ward & Tordai (1946) pursued a complementary problem: the diffusion-limited mass transfer to an initially clean planar interface. More recently, Jin *et al.* (2004) and Alvarez *et al.* (2010*a*,b) established the critical role of interfacial curvature on surfactant transport. In what follows, we explore their calculations of surfactant exchange to an initially clean static bubble, in both diffusion- and kinetically-limited regimes.

The system is the same as in § 3.2.1, except that the bubble interface is stationary, $R(t) = R_0$, and is initially clean: $\Gamma(0) = 0$. Surfactant is dissolved in the bulk at concentration C_0, and

the subsurface concentration is $C(R, t) = C_s(t)$. The surface conservation equation (3.10) with the diffusive flux j_{diff} from the bulk is

$$\frac{\partial \Gamma}{\partial t} = D\frac{\partial C}{\partial r}\bigg|_{r=R}, \tag{3.57}$$

where $C(R, t)$ follows from the solution of the bulk diffusion equation. Laplace transforming (3.57), denoted by tildes, gives

$$s\tilde{\Gamma} = D\frac{\partial \tilde{C}}{\partial r}\bigg|_{r=R}, \tag{3.58}$$

where s is the Laplace transform variable. Laplace transforming the bulk diffusion equation gives

$$s\tilde{C} - C_0 = D\nabla^2\tilde{C}, \tag{3.59}$$

with solution

$$\tilde{C}(r, s) = \frac{C_0}{s} + \frac{C_1}{r}e^{-r\sqrt{s/D}}, \tag{3.60}$$

where C_1 is as yet unknown. Evaluating (3.58) with (3.60), then eliminating C_1 in (3.60) in favor of C_s gives

$$\tilde{\Gamma}(s) = \sqrt{D}\left[\frac{C_0}{s^{3/2}} - \frac{\tilde{C}_s(s)}{\sqrt{s}}\right] + \frac{D}{R}\left[\frac{C_0}{s^2} - \frac{\tilde{C}_s(s)}{s}\right], \tag{3.61}$$

Finally, inverting the Laplace transform of (3.61) gives

$$\Gamma(t) = \sqrt{\frac{D}{\pi}}\left[2C_0\sqrt{t} - \int_0^t \frac{C_s(t')}{\sqrt{t-t'}}\mathrm{d}t'\right] + \frac{D}{R}\left[C_0 t - \int_0^t C_s(t')\mathrm{d}t'\right]. \tag{3.62}$$

The first term on the right hand side reflects the solution of Ward & Tordai (1946) for adsorption onto a clean planar interface, whereas the last two terms reflect interfacial curvature (Jin *et al.* 2004; Alvarez *et al.* 2010*a*).

The generalized Ward-Tordai result (3.62) is an implicit integral relation between $\Gamma(t)$ and the yet undetermined subsurface concentration $C_s(t)$. Solving for the surface concentration requires another relationship between $\Gamma(t)$ and $C_s(t)$, which follows from the kinetic flux condition (3.24). However, inverting this relation is not straightforward except for the simplest kinetic flux expressions, and is typically solved numerically (Jin *et al.* 2004; Alvarez *et al.* 2010*a*). For example, the 2D ideal gas assumption (table 2) gives

$$\frac{\partial \Gamma}{\partial t} = k_a C_s - k_d \Gamma, \tag{3.63}$$

with Laplace transform

$$s\tilde{\Gamma} = k_a\tilde{C}_s - k_d\tilde{\Gamma}. \tag{3.64}$$

In principle, eliminating $\tilde{C}_s$ between (3.64) and (3.61), and inverse Laplace transforming $\tilde{\Gamma}(s)$ gives an explicit expression for $\Gamma(t)$. In fact, Hansen (1961) employs this strategy to examine adsorption to a planar interface ($R \to \infty$).

Even for the simplest kinetic flux (3.63), however, adsorption to a spherical interface is intractable at arbitrary Damköhler number. Instead, we highlight the kinetically-controlled ($Da \ll 1$) and diffusion-controlled ($Da \gg 1$) limits individually, by ignoring j_{diff} and j_{kin}, respectively. These limits are easier to calculate, and are illustrative in light of the discussion around oscillating bubbles in the previous section. For later use, we note that the equilibrium surface concentration following (3.63) is

$$\Gamma_{\text{eq}} = L_d C_0, \tag{3.65}$$

with depletion depth

$$L_d = \frac{k_a}{k_d} = K^{\text{ideal}}. \tag{3.66}$$

When surfactant transport is kinetically-limited, diffusion in the bulk is assumed to be instantaneous, so that $C_s(t) = C_0$. Laplace transforming (3.63) with $C_s = C_0$ and using (3.65) gives

$$\frac{\tilde{\Gamma}_{\text{kin}}(s)}{\Gamma_{\text{eq}}} = \frac{k_d}{s(s + k_d)}, \tag{3.67}$$

with inverse

$$\frac{\Gamma_{\text{kin}}(t)}{\Gamma_{\text{eq}}} = 1 - e^{-k_d t}, \tag{3.68}$$

which recovers the kinetically-limited sorption time $\tau_k = 1/k_d$ (3.45). At short times, Γ_{kin} grows linearly with time, whereas Γ_{kin} approaches Γ_{eq} exponentially for $t \gg \tau_k$ (figure 9 *a*). Like with adsorption to an oscillating bubble, kinetically-limited mass transfer is independent of bubble size.

By contrast, contact equilibrium is assumed between $\Gamma(t)$ and $C_s(t)$ when adsorption is diffusion-controlled, so that

$$\Gamma_{\text{diff}}(t) = L_d C_s(t). \tag{3.69}$$

Using the Laplace transform of (3.69) to eliminate $\tilde{C}_s$ in (3.61) gives

$$\frac{\tilde{\Gamma}_{\mathrm{diff}}(s)}{\Gamma_{\mathrm{eq}}} = \frac{s^{1/2} + \sqrt{D/R^2}}{s^{3/2} + s\sqrt{D/R^2} + s^2\sqrt{L_d^2/D}}. \tag{3.70}$$

Inverting (3.70) is laborious but straightforward, and yields:

$$\frac{\Gamma_{\mathrm{diff}}(t)}{\Gamma_{\mathrm{eq}}} = 1 + \frac{1}{\beta - \alpha}\left[\alpha e^{\alpha^2 t}\,\mathrm{erfc}(\alpha\sqrt{t}) - \beta e^{\beta^2 t}\,\mathrm{erfc}(\beta\sqrt{t})\right], \tag{3.71}$$

where

$$\alpha = \frac{\sqrt{D}}{2L_d}(1 + \sqrt{1 - 4\Lambda_d}), \quad \beta = \frac{\sqrt{D}}{2L_d}(1 - \sqrt{1 - 4\Lambda_d}), \tag{3.72}$$

and $\Lambda_d = L_d/R$ (3.48).

The large- and small-bubble limits of (3.70) are particularly illustrative. Bubbles with radii much larger than the depletion depth ($\Lambda_d \to 0$) have

$$\left.\frac{\Gamma_{\mathrm{diff}}(t)}{\Gamma_{\mathrm{eq}}}\right|_{\Lambda_d \to 0} = 1 - e^{Dt/L_d^2}\,\mathrm{erfc}\left(\sqrt{Dt}/L_d\right), \tag{3.73}$$

recovering the result of Hansen (1961) for a planar interface. Indeed, the characteristic diffusion time in (3.73) is $\tau_{d,p} = L_d^2/D$, like in diffusion-limited adsorption to large oscillating bubbles (3.52). Γ_{diff} approaches Γ_{eq} algebraically at long times (figure 9 *b*), much more slowly than the exponential approach during kinetically-controlled adsorption (3.68).

When the bubble is much smaller than the depletion depth ($\Lambda_d \gg 1$), however, surface concentration approaches equilibrium exponentially, via

$$\left.\frac{\Gamma_{\mathrm{diff}}(t)}{\Gamma_{\mathrm{eq}}}\right|_{\Lambda_d \gg 1} = 1 - e^{-Dt/L_d R}. \tag{3.74}$$

The characteristic diffusion time $\tau_{d,s} = L_d R/D$ that emerges is the same (eq. 3.54) that controls small, oscillatory bubbles. Like with oscillating bubbles, diffusion-limited adsorption to small bubbles ($R \ll L_d$) has the same form as kinetically-limited adsorption (3.68), except with $\tau_{d,s}$ replacing τ_k. As shown in figure 9 (*b*), diffusion-limited adsorption is faster for smaller bubbles, and Γ_{diff} approaches Γ_{eq} exponentially rather than algebraically over long times.

Finally, convection in the bulk fluid further enhances the rate of diffusive adsorption by 'screening' the characteristic diffusion length by the thickness of the diffusion boundary layer δ_{BL}. Alvarez *et al.* (2012) demonstrated that the diffusion time is indeed $\tau_{d,p}^{\mathrm{conv}} \propto \delta_{\mathrm{BL}}^2$ for large bubbles, and $\tau_{d,p}^{\mathrm{conv}} \propto \delta_{\mathrm{BL}}$ for smaller bubbles. This scaling suggests strategies to further speed up diffusive surfactant transport using flow, as the boundary layer thickness decreases with increasing bulk convection, thereby increasing the range of measurable kinetic-limited adsorption (Alvarez *et al.* 2012).

3.3. Marangoni flows

Marangoni flows are driven by excess surface stresses due to gradients in surface tension. Scriven & Sternling (1960) provide a historical perspective, beginning with Plateau's oscillating needle experiments on fluid interfaces, and subsequent explanations by Marangoni and Gibbs. Non-uniform surface tension may arise on surfactant monolayers due to surface convection of adsorbed surfactants or inhomogeneous adsorption from the bulk. Surface tension gradients can also be established by externally inducing gradients in properties that affect γ. For instance, interfaces of droplets suspended in a fluid with background gradients in temperature, surfactant concentration, or electrostatic potential exhibit Marangoni flows, leading to, respectively, thermo-, soluto-, or electrocapillary motion (Squires & Quake 2005). For simplicity, we assume throughout this article that gradients in temperature or electrical charge do not arise on fluid interfaces, such that Marangoni flows are driven by surfactant transport alone.

3.3.1. Surface concentration gradients and hydrodynamic coupling—Recall from §3.1.2 that spatial gradients in the surface chemical potential μ_s point to energetically unfavorable locations to place adsorbed surfactants. A thermodynamic force $\boldsymbol{f}_s = -\boldsymbol{\nabla}\mu_s$ drives surfactants *down* the gradient with a velocity given by the molecule's hydrodynamic mobility (3.15). However, a molecule moves not only because it is forced, but also because its neighbors are forced, and drive fluid flows that entrain the molecule. Readers familiar with suspension dynamics will recognize hydrodynamic coupling in a 3D fluid with background velocity $\boldsymbol{V}_\infty$:

$$\boldsymbol{V}_i - \boldsymbol{V}_\infty(\boldsymbol{r}_i) = \frac{\boldsymbol{F}_i}{6\pi\eta R_i} + \sum_{j\neq i} \boldsymbol{G}(\boldsymbol{r}_i - \boldsymbol{r}_j)\cdot\boldsymbol{F}_j, \tag{3.75}$$

where the tensor $\boldsymbol{G}(\boldsymbol{r}_i-\boldsymbol{r}_j)$ gives the velocity at $\boldsymbol{r}_i$ in response to a force $\boldsymbol{F}_j$ on a particle centered at $\boldsymbol{r}_j$ (Guazzelli & Morris 2012; Happel & Brenner 1965). In many cases (e.g. sedimentation), the hydrodynamic coupling sum may overwhelm the 'self-mobility' term.

The precise analog occurs at surfactant interfaces: the velocity of a surfactant molecule at $\boldsymbol{r}_i$ is a combination of the background velocity $\boldsymbol{u}_s$, the 'self' mobility, and the hydrodynamic coupling, so that (3.15) is modified to include

$$\boldsymbol{V}_i - \boldsymbol{u}_s(\boldsymbol{r}_i) = -\frac{D_s}{k_B T}\boldsymbol{\nabla}_s\mu(\boldsymbol{r}_i) - \sum_{j\neq i}\boldsymbol{G}(\boldsymbol{r}_i-\boldsymbol{r}_j)\cdot\Gamma(\boldsymbol{r}_j)\boldsymbol{\nabla}_s\mu(\boldsymbol{r}_j), \tag{3.76}$$

where the final term reflects the surface velocity at $\boldsymbol{r}_i$, established by all neighboring surfactant molecules – with concentration Γ, each forced by $-\boldsymbol{\nabla}_s\mu$. The Green's function $\boldsymbol{G}(\boldsymbol{r}_i-\boldsymbol{r}_j)$ in this case gives the fluid velocity on the interface at $\boldsymbol{r}_i$, driven by a force at $\boldsymbol{r}_j$ on the fluid interface. The precise form of the Green's function depends on the geometry of the interface, the subphase depth, etc. (§3.4.2) The added velocity due to hydrodynamic interactions, however, corresponds to a boundary integral solution (Pozrikidis 1992) to the Stokes equations, where the fluid interface is driven by a specified traction:

$$\boldsymbol{f}_M \equiv \boldsymbol{n}\cdot\boldsymbol{\sigma}\big|_{\text{interface}} = -\Gamma\boldsymbol{\nabla}_s\mu, \tag{3.77}$$

which, using the Gibbs adsorption relation (3.22), becomes

$$\boldsymbol{f}_M = -\boldsymbol{\nabla}_s\Pi = \boldsymbol{\nabla}_s\gamma\,. \tag{3.78}$$

The hydrodynamic coupling (3.76) between surfactant molecules is precisely equal to the net convective velocity driven by surface tension gradients. In other words, hydrodynamic coupling between surfactants is equivalent to the Marangoni flow driven on the interface by the surfactant monolayer.

Surface pressure gradients can drive or balance viscous shear stress following (3.78). Figure 10 illustrates two examples of the conjugate effects that usually go by the name of Marangoni, both of which involve surfactant gradients. Gradients in surface pressure may arise due to non-uniform surface concentrations $\Gamma(\boldsymbol{r}_s)$, or due to surface convective transport $\boldsymbol{u}_s\Gamma$ that establishes a concentration gradient. Depositing surfactant on an initially clean interface (figure 10 *a*) introduces a surface concentration gradient $\boldsymbol{\nabla}_s\Gamma$, and therefore a surface pressure gradient that exerts a traction

$$\boldsymbol{f}_M = \eta\frac{\partial\boldsymbol{v}}{\partial z}\bigg|_{z=0} = -\boldsymbol{\nabla}_s\Pi = -\frac{\partial\Pi}{\partial\Gamma}\boldsymbol{\nabla}_s\Gamma\,. \tag{3.79}$$

Flows are therefore driven down surface pressure (or surface concentration) gradients.

The functional form of $\Pi(\Gamma)$ depends on the particular surfactant isotherm (§2.4). It is common practice to assume an ideal gas monolayer, for which the Marangoni traction is

$$\boldsymbol{f}_M^{\text{ideal}} = -k_BT\boldsymbol{\nabla}_s\Gamma\,. \tag{3.80}$$

As discussed in §2.3, however, the ideal gas assumption rarely holds in practice, and more accurate models or measured values of $\partial\Pi/\partial\Gamma$ would be more appropriate. For example, the Langmuir and Volmer isotherms give tractions

$$\boldsymbol{f}_M^L = -\frac{k_BT}{1-\Gamma/\Gamma_\infty}\boldsymbol{\nabla}_s\Gamma, \quad \text{and} \quad \boldsymbol{f}_M^V = -\frac{k_BT}{(1-\Gamma/\Gamma_\infty)^2}\boldsymbol{\nabla}_s\Gamma, \tag{3.81}$$

both of which recover the ideal gas limit when $\Gamma \ll \Gamma_\infty$.

The second example, shown in figure 10 (*b*), resembles the so-called ‘Reynolds ridge’ (Scott 1982) and involves flows that compress (or dilate) a surfactant-laden fluid interface against a floating barrier. Such a flow creates surface concentration gradients that act against the interfacial compression (or dilatation). Marangoni stresses therefore act like surface excess elasticity (Langevin 2014), working to lessen surface compression or dilatation. In what follows, we quantify the degree to which reverse Marangoni flows resist inhomogeneous surface compression.

3.3.2. Marangoni numbers and surface incompressibility—Surfactant monolayers are far more compressible than 3D fluids. Compressing an insoluble surfactant increases the surface concentration Γ and thus the surface pressure Π. Additionally, many surfactants exhibit phase transitions (Kaganer *et al.* 1999) and surface-pressure-dependent surface viscosity (Kurtz *et al.* 2006; Kim *et al.* 2011) even under facile compression, as discussed in §5. However, *inhomogeneous* compression of a surfactant monolayer drives reverse Marangoni flows that resist such deformations.

For example, a disk of radius R translating at velocity U within a planar surfactant-laden interface compresses the monolayer ahead of the disk, and dilates the monolayer in its rear (figure 11). The surfactant conservation equation for insoluble surfactants (3.10) at steady state, in the absence of surface diffusion, gives the surface divergence

$$\boldsymbol{\nabla}_s \cdot \boldsymbol{u}_s = -\frac{1}{\Gamma}\boldsymbol{u}_s \cdot \boldsymbol{\nabla}_s \Gamma = -\frac{1}{E_0}\boldsymbol{u}_s \cdot \boldsymbol{\nabla}_s \Pi, \tag{3.82}$$

where E_0 is the Marangoni modulus (2.22). Balancing the surface pressure gradient $\boldsymbol{\nabla}_s \Pi$ in (3.82) with traction on the subphase via the Marangoni boundary condition (3.79) gives

$$\boldsymbol{\nabla}_s \cdot \boldsymbol{u}_s = \frac{\eta}{E_0}\boldsymbol{u}_s \cdot \left.\frac{\partial \boldsymbol{v}}{\partial z}\right|_{z=0}. \tag{3.83}$$

Non-dimensionalizing gives a dimensionless surface divergence

$$\widetilde{\boldsymbol{\nabla}}_s \cdot \tilde{\boldsymbol{u}}_s = \frac{1}{Ma}\tilde{\boldsymbol{u}}_s \cdot \left.\frac{\partial \tilde{\boldsymbol{v}}}{\partial \tilde{z}}\right|_{\tilde{z}=0}, \tag{3.84}$$

where the Marangoni number

$$Ma = \frac{E_0}{\eta U} \tag{3.85}$$

balances surface compressibility E_0/R against viscous traction $\eta U/R$.

In the large Marangoni number limit ($Ma \gg 1$), surfactant molecules resist compression so strongly that the surface flow is effectively divergence-free. In other words, the surface is 2D incompressible when the time scale to establish reverse Marangoni flows

$$\tau_m = \frac{\eta R}{E_0}, \tag{3.86}$$

is much faster than the surface convection time scale $\tau_{\text{flow}} = R/U$, so that $Ma = \tau_{\text{flow}}/\tau_m \gg 1$. Surface pressure then acts as a Lagrange multiplier to maintain surface incompressibility, much like bulk pressure in a 3D fluid (figure 11). In unidirectional surface flows, such as in figure 10 (*b*), surface incompressibility requires $\boldsymbol{u}_s$ to be constant. Marangoni flows then 'immobilize' the interface, effectively modifying the interfacial boundary condition from a free surface ($\partial v/\partial z = 0$) when $Ma \ll 1$ to a rigid surface ($u_s = v(0) = \text{constant}$) when $Ma \gg 1$.

Insoluble surfactants are almost always surface incompressible around translating disks or particles. The Marangoni modulus of incredibly dilute monolayers with $\Gamma \sim 1/(100\ \mathrm{nm}^2)$ in the ideal gas limit is $E_0^{\mathrm{ideal}} = k_B T \Gamma \sim 0.04\ \mathrm{mN/m}$. Even for such dilute monolayers with immeasurably small surface pressures ($\Pi \sim 40\ \mu\mathrm{N/m}$), a disk or particle must translate faster than 4 cm/s before $Ma \lesssim 1$ and the interface compresses. The Marangoni modulus of real surfactants is much larger than E_0^{ideal} (table 1), with typical values of $E_0 \gtrsim 1\ \mathrm{mN/m}$ (Kotula & Anna 2016; Arriaga *et al.* 2010), so that insoluble monolayers are effectively surface incompressible unless $U \gtrsim 1\ \mathrm{m/s}$.

Even the slightest amount of insoluble surfactant, therefore, fundamentally changes the interfacial boundary condition on the bulk fluid flow. Stone & Masoud (2015) illustrated the change in subphase flow by considering the continuity equation for the bulk fluid at the interface,

$$\boldsymbol{\nabla} \cdot \boldsymbol{v}|_{z=0} = \boldsymbol{\nabla}_s \cdot \boldsymbol{v}|_{z=0} + \frac{\partial w}{\partial z} = 0, \tag{3.87}$$

where w is the z-component of subphase fluid velocity $\boldsymbol{v}$. At the interface, the tangential velocity is $\boldsymbol{v} = \boldsymbol{u}_s$, and thus surface incompressibility implies $\partial w/\partial z = 0$. The vertical velocity w vanishes at $z = 0$ for an interface that does not deform out of plane, and along with $\partial w/\partial z = 0$ requires that w be zero throughout the subphase. Surface incompressibility therefore constrains subphase fluid to flow in planes parallel to the interface (figure 11 *d*). Such flows set up stronger velocity gradients, dissipating more energy than in surfactant-free systems, where flow in the bulk is three-dimensional (figure 11 *b*).

Insoluble surfactants therefore substantially modify subphase flow relative to surfactant-free systems, increasing the translational resistance of particles within monolayers. For example, the drag on a circular disk translating in an incompressible monolayer exceeds the drag in a clean interface by a factor of 3/2 (§4.6). In some cases, this increase in translational resistance has been misattributed to surface rheology, going back to Plateau's experiments with oscillating needles on interfaces (Scriven & Sternling 1960), while in fact it arises due to Marangoni flows. Indeed, surface incompressibility increases the hydrodynamic drag on translating probes even for a completely inviscid surfactant, causing significant confusion in the measurement and interpretation of surface rheology of insoluble surfactants (Sickert & Rondelez 2003; Fischer 2004*a*, and §3.4).

Soluble surfactants, on the other hand, may desorb (or adsorb) as the interface is compressed (or dilated) to restore equilibrium coverage (figure 11 *a*). The strength of the Marangoni stress then depends on the balance between surface advective and surfactant exchange fluxes. For small perturbations $\delta\Gamma$ in surface concentration around an equilibrium value Γ_0, the surfactant balance (3.10) becomes

$$\Gamma_0 \boldsymbol{\nabla}_s \cdot \boldsymbol{u}_s = j_n = -\frac{\delta\Gamma}{\tau_s}, \tag{3.88}$$

where τ_s is the longer among kinetic and diffusive surfactant exchange times (3.56). Using (3.88) in the Marangoni boundary condition (3.79) gives

$$\eta \frac{\partial \boldsymbol{v}}{\partial z}\bigg|_{z=0} = -\frac{\partial \Pi}{\partial \Gamma}\nabla_s(\delta\Gamma) = E_0\tau_s\nabla_s(\nabla_s\cdot\boldsymbol{u}_s), \tag{3.89}$$

where E_0 is the Marangoni modulus (2.22). Significantly, any finite adsorption time scale τ_s gives rise to a viscous-like force with *apparent* dilatational surface viscosity $E_0\tau_s$ in (3.89) – a feature we will explore in detail in §3.4.3. Nondimensionalizing (3.89) gives

$$\widetilde{\nabla}_s\left(\widetilde{\nabla}_s\cdot\tilde{\boldsymbol{u}}_s\right) = \frac{1}{Ma_K}\frac{\partial\tilde{v}}{\partial\tilde{z}}\bigg|_{\tilde{z}=0}, \tag{3.90}$$

where

$$Ma_K = \frac{E_0\tau_s}{\eta R} = \frac{\tau_s}{\tau_m} \tag{3.91}$$

is a modified Marangoni number, that now compares the time scale $\tau_m = \eta R/E_0$ to establish Marangoni flow with the time τ_s for the surface to equilibrate via adsorption/desorption.

If a soluble monolayer equilibrates before Marangoni flows can be established ($Ma_K \ll 1$), then the surface behaves as if it is compressible. Equation (3.90) recovers the stress-free boundary condition as $Ma_K \to 0$, and fluid flows behave approximately as though the interface were clean (figure 11 *b*). In this limit, Γ and Π are largely unperturbed from the surfactant's equilibrium isotherm. By contrast, if Marangoni flows are established before surfactants adsorb and desorb to equilibrate with the subphase concentration ($Ma_K \gg 1$), then the surface divergence is

$$\widetilde{\nabla}_s\cdot\tilde{\boldsymbol{u}}_s \approx \text{constant} = \dot{\epsilon}, \tag{3.92}$$

where $\dot{\epsilon}$ is a *uniform* compression or dilatation rate. In fact, interfaces with fixed area require $\dot{\epsilon} = 0$, and the interface acts as incompressible.

Finally, Marangoni flows may also be weakened by other surface processes, leading to alternative definitions of the Marangoni number. Table 3 summarizes common definitions of Marangoni numbers, obtained by comparing the Marangoni timescale τ_m against competing system-specific surfactant processes. In each case, a large Marangoni number implies that the surfactant monolayer resists inhomogeneous surface compression or dilatation, and the interface can be approximated as 2D incompressible. When Marangoni flows are weak, a fully compressible description becomes necessary (Barentin *et al.* 1999; Elfring *et al.* 2016).

3.4. Surface rheology

Thus far, we have focused on surface processes such as adsorption/desorption, Marangoni flows, and surface diffusion, which redistribute surfactants on the interface, and relax surface stresses in doing so. Additionally, however, some surfactants are known to exhibit *surface rheology*, exerting additional stresses when the surfactant layer deforms against itself.

The origin, existence and interpretation of surface rheology have been debated since the mid nineteenth century by the likes of Gibbs, Plateau, Marangoni, and Rayleigh (Scriven & Sternling 1960). Part of the controversy arises because even relatively simple flows excite multiple surfactant processes, or drive mixed surface deformations. For example, translating probes deform the surface via compression and dilatation in addition to shear, driving a combination of surface viscous and Marangoni stresses. Surfactant-induced 2D incompressibility fundamentally changes the subphase flow from the stress-free surface arising in the absence of surfactant, and changes the translational drag of probes substantially, even for completely inviscid surfactant monolayers (Fischer 2004*a*, and §3.3.2). Experimental geometries specifically designed to drive purely shear deformations, like rotating disks (Choi *et al.* 2011) or translating needles (Brooks *et al.* 1999), however, probe surface shear rheology unambiguously.

More subtle difficulties arise when surface viscosity is indirectly inferred from observable phenomena such as the settling velocity of surfactant-covered drops, or the drainage time of thin films. For example, recall from §3.3.2 that Marangoni flows with finite-time adsorption introduces a surface-viscous-like force in the interfacial stress balance (3.89). In such systems, can this apparent surface dissipation alone account for all observed dynamics, or might the surfactant monolayer possess an ‘intrinsic’ surface dilatational viscosity? How does one differentiate between an ‘intrinsic’ and ‘apparent’ surface viscosity if both are present? In many cases, it might not be easy or even possible to deconvolve the origins of surface dissipation, leading to thousandfold discrepancies in surface viscosities interpreted from decades of experiments (Stevenson 2005).

In this section, we will explore the simplest of surface rheological models – monolayers that behave like 2D Newtonian fluids. We use this model to (a) interpret experiments that confirm and characterize ‘intrinsic’ surface shear viscosities, (b) illustrate the relative contributions of subphase and interfacial viscous resistance to flow, and (c) highlight difficulties in determining ‘intrinsic’ surface dilatational viscosities from experiments. The 2D Newtonian model will also set the stage for treating surface rheology in the paradigmatic problems outlined in §4. The richer and more complex surface rheological responses that arise more commonly are described in §5.

3.4.1. The Boussinesq-Scriven model—Boussinesq (1913) was the first to explicitly account for a viscous-like resistance to surface dilatation, using it to explain the anomalous settling velocity of drops (§4.1). Scriven (1960) generalized Boussinesq’s model by treating the interfacial layer as a 2D Newtonian fluid with intrinsic surface shear (η_s) and surface dilatational (κ_s) viscosities, both with dimensions of 3D viscosity × length, so that the extra rheological stress $\boldsymbol{\tau}_{\text{rheo}}$ in (3.8) is Newtonian:

$$\boldsymbol{\tau}_{\text{rheo}} = [(\kappa_s - \eta_s)\boldsymbol{\nabla}_s \cdot \boldsymbol{u})]\boldsymbol{I}_s + \eta_s\left[\boldsymbol{\nabla}_s\boldsymbol{u} \cdot \boldsymbol{I}_s + \boldsymbol{I}_s \cdot (\boldsymbol{\nabla}_s\boldsymbol{u})^T\right], \tag{3.93}$$

where $\boldsymbol{I}_s = \boldsymbol{I} - \boldsymbol{nn}$ is the surface identity tensor. Using (3.93) in the surface stress balance (3.8) for a planar liquid-air interface gives

$$\eta \frac{\partial \boldsymbol{v}}{\partial z}\Big|_{z=0} = -\nabla_s \Pi + \eta_s \nabla_s^2 \boldsymbol{u}_s + \kappa_s \nabla_s (\nabla_s \cdot \boldsymbol{u}_s), \tag{3.94}$$

which is the 2D analog of the Stokes equation for compressible fluids, with viscous traction from the subphase entering as a body force. More generally, out-of-plane deformations and 2D viscous flow along curved interfaces introduce additional forces that have no analog in 3D Newtonian fluids (Scriven 1960; Aris 1962; Edwards *et al.* 1991; Slattery *et al.* 2007).

The Boussinesq-Scriven model simplifies in many typical surfactant systems. As discussed in §3.3.2, insoluble surfactants almost always behave as surface incompressible, in which case (3.94) reduces to the incompressible 2D Stokes equation, forced by viscous traction from the subphase:

$$\nabla_s \Pi = \eta_s \nabla_s^2 \boldsymbol{u}_s - \eta \frac{\partial \boldsymbol{v}}{\partial z}\Big|_{z=0}, \quad \nabla_s \cdot \boldsymbol{u}_s = 0. \tag{3.95}$$

Surface pressure then acts to enforce 2D incompressibility, analogous to bulk pressure in a 3D incompressible fluid.

Solving such problems is generally difficult, because two- and three-dimensional Stokes flows must be solved separately, but coupled via boundary conditions enforcing surface incompressibility and subphase traction. In systems where the subphase is very shallow, though, this coupling simplifies significantly, because the lubrication approximation relates the subphase velocity gradient to interfacial velocity and the subphase depth H,

$$\frac{\partial \boldsymbol{v}}{\partial z}\Big|_{z=0} = \frac{\boldsymbol{u}_s}{H}, \tag{3.96}$$

in which case the subphase flow need not be solved explicitly (Evans & Sackmann 1988). The lubrication approximation is particularly useful for compressible monolayers, where eliminating $\boldsymbol{u}$ permits analytical solutions (Barentin *et al.* 1999; Elfring *et al.* 2016).

3.4.2. 2D vs. 3D hydrodynamics and the Boussinesq number—Momentum propagation through a viscous interfacial layer fundamentally modifies familiar 3D fluid dynamics, even when no other surfactant process is excited. For example, pure shear deformations like the swirling flow driven by rotating a circular disk at an interface (figure 12) do not generate surface concentration gradients, and thus do not give rise to Marangoni stresses. The planar Boussinesq-Scriven equation (3.94) then becomes

$$\eta \frac{\partial \boldsymbol{v}}{\partial z}\Big|_{z=0} = \eta_s \nabla_s^2 \boldsymbol{u}_s, \tag{3.97}$$

which couples to the Stokes equations for $\boldsymbol{u}$ in the subphase. Flow is driven by the rotation of a disk of radius R at constant angular velocity Ω: $\boldsymbol{u}_s(r \leqslant R) = \Omega r \hat{\boldsymbol{\theta}}$.. Nondimensionalizing (3.97) gives

$$\left.\frac{\partial \widetilde{\boldsymbol{v}}}{\partial \widetilde{z}}\right|_{\widetilde{z}=0} = Bq\,\widetilde{\nabla}_s^2 \widetilde{\boldsymbol{u}}_s, \tag{3.98}$$

where the Boussinesq number,

$$Bq = \frac{\eta_s}{\eta R}, \tag{3.99}$$

compares surface and subphase viscous stresses.

Subphase-dominant flows ($Bq \ll 1$) in pure shear recover the stress-free condition at the interface. Solving the Stokes equations in the subphase with a stress-free interface driven driven by a rotating disc gives (Goodrich 1969)

$$\boldsymbol{u}_s(Bq = 0) = \frac{2\Omega R}{\pi}\left[\frac{r}{R}\sin^{-1}\left(\frac{R}{r}\right) - \left(1 - \frac{R^2}{r^2}\right)^{1/2}\right]\widehat{\boldsymbol{\theta}} \underrightarrow{r \gg R} \frac{4\Omega}{3\pi}\frac{R^3}{r^2}\widehat{\boldsymbol{\theta}}. \tag{3.100}$$

The velocity field due to rotation decays as $1/r^2$ in the absence of surface excess rheological stresses, as expected in Stokes flow (Guazzelli & Morris 2012).

By contrast, (3.98) implies that $\nabla_s^2 \boldsymbol{u}_s \approx \mathbf{0}$ when the flow is interface-dominant ($Bq \gg 1$), and

$$\boldsymbol{u}_s(Bq \to \infty) = \frac{\Omega R^2}{r}\widehat{\boldsymbol{\theta}}. \tag{3.101}$$

A viscous interfacial layer propagates momentum more extensively within the interface, resulting in a slower decay ($\sim 1/r$) of the surface velocity field relative to (3.100), as shown in figure 12 (*b*). The torque required to sustain constant rotation transitions from $\sim R^3$ for an inviscid interface ($Bq = 0$) to $\sim R^2$ for a viscous monolayer ($Bq \to \infty$; see §4.6). This striking difference arises in systems where no other surfactant transport process – e.g. Marangoni flow, adsorption/desorption, surface dilatation – is active. Measurements of the rotational torque and flow field around a rotating disk can thus unambiguously and quantitatively detect surface shear viscosity (Choi *et al.* 2011; Zell *et al.* 2014).

The translation of a particle embedded within a monolayer is more complex, as it deforms the surface via compression, dilation, and extension, in addition to shear. Even in the seemingly simpler case of insoluble (and, therefore, 2D incompressible from §3.3.2) monolayers, translation introduces subtleties due to momentum transfer between a surface-shear-viscous interface and the underlying 3D fluid.

Saffman & Delbrück (1975) noticed this transition from 2D to 3D hydrodynamics in their seminal work on particle diffusion in biological membranes. The incompressible Boussinesq-Scriven equation (3.95) decouples from the subphase in the interface-dominant ($Bq \to \infty$) limit. However, there is no solution for steady translation of a cylinder in 2D creeping flow (Leal 2007, the 'Stokes paradox'). Saffman (1976) recognized that subphase viscous stresses ($\sim \eta U \ell_{\mathrm{SD}}$) eventually catch up with surface viscous stresses ($\sim \eta_s U$) beyond a distance

$$\ell_{\mathrm{SD}} = \frac{\eta_s}{\eta}, \tag{3.102}$$

ultimately regularizing the divergence inherent to 2D Stokes flow. Surface viscous stresses dominate within the Saffman-Delbrück length ℓ_{SD}, and viscous traction from the subphase prevail beyond ℓ_{SD}.

The crossover from 2D to 3D hydrodynamics is evident in the flow driven by a tangential point force on the interface (Lubensky & Goldstein 1996; Levine & MacKintosh 2002; Fischer 2004*b*; Oppenheimer & Diamant 2009). Velocity fields driven by arbitrarily shaped particles moving on an interface can be constructed using appropriate boundary integrals of the point-force solution (§4.6).

An incompressible Newtonian monolayer along the *x*–*y* plane acted upon by an in-plane point force $\boldsymbol{F}$ at $\boldsymbol{x}_0$ is governed by

$$\boldsymbol{\nabla}_s \Pi = \eta_s \boldsymbol{\nabla}_s^2 \boldsymbol{u}_s - \eta \left.\frac{\partial \boldsymbol{v}}{\partial z}\right|_{z=0} + \boldsymbol{F}\delta(\boldsymbol{r}), \quad \boldsymbol{\nabla}_s \cdot \boldsymbol{u}_s = 0, \tag{3.103}$$

where $\boldsymbol{r} = \boldsymbol{x} - \boldsymbol{x}_0$. The two-dimensional Fourier transform,

$$\phi(\boldsymbol{x}) = \int \hat{\phi}(\boldsymbol{k}) e^{i\boldsymbol{k}\cdot\boldsymbol{r}} \mathrm{d}\boldsymbol{k}, \tag{3.104}$$

is defined so that $\boldsymbol{k} \cdot \hat{\boldsymbol{e}}_z = 0$, and transforms (3.103) to give

$$i\boldsymbol{k}\widehat{\Pi} = -\eta_s k^2 \widehat{\boldsymbol{u}}_s - \eta \left.\frac{\partial \widehat{\boldsymbol{v}}}{\partial z}\right|_{z=0} + \boldsymbol{F}, \quad \boldsymbol{k}\cdot\widehat{\boldsymbol{u}}_s = 0. \tag{3.105}$$

The (3D) hydrodynamic pressure field *p* associated with flow on an incompressible surface is a constant everywhere (Stone & Ajdari 1998), such that momentum balance for Stokes flow in the bulk reduces to Laplace's equation: $\boldsymbol{\nabla}^2 \boldsymbol{v} = \boldsymbol{0}$. If the subphase extends to a finite depth *H* such that $\boldsymbol{v}(-H) = \boldsymbol{0}$, then

$$\widehat{\boldsymbol{v}}(\boldsymbol{k}) = \left(\frac{\sinh(kz)}{\tanh(kH)} + \cosh(kz)\right)\widehat{\boldsymbol{u}}_s(\boldsymbol{k}). \tag{3.106}$$

Using (3.106) in (3.105) and eliminating $\widehat{\Pi}$ by premultiplying by $\boldsymbol{I} - \boldsymbol{kk}/k^2$ gives

$$\widehat{\boldsymbol{u}}_s(\boldsymbol{k}) = \widehat{\boldsymbol{G}}(\boldsymbol{k}) \cdot \boldsymbol{F} = \left[\frac{k^2\boldsymbol{I} - \boldsymbol{kk}}{k^4\eta_s + k^3\eta\coth(kH)}\right] \cdot \boldsymbol{F} \tag{3.107}$$

The Green's function $\hat{\boldsymbol{G}}(\boldsymbol{k})$ depends on the ratio $k\eta_s/\eta$, which is the Boussinesq number (3.99) for a length scale $\lambda = 2\pi/k$. In real space, the second-order tensor $\boldsymbol{G}(\boldsymbol{r})$ is the surface analog of the Oseen tensor in classical hydrodynamics. However, inverting $\hat{\boldsymbol{G}}$ is not straightforward except in specific limits. We will focus on the deep subphase limit ($H \rightarrow$

∞), where the inverse transform gives (Fischer 2004*b*; Lubensky & Goldstein 1996; Levine & MacKintosh 2002)

$$\boldsymbol{u}_s(\boldsymbol{x}) = \frac{1}{4\eta_s}\left[\mu_{\parallel}(r)\frac{\boldsymbol{r}\boldsymbol{r}}{r^2} + \mu_{\perp}(r)\left(\boldsymbol{I} - \frac{\boldsymbol{r}\boldsymbol{r}}{r^2}\right)\right]\cdot \boldsymbol{F}, \tag{3.108}$$

where $r = |\boldsymbol{r}|$. The mobility coefficients $\mu_{\parallel}$ and $\mu_{\perp}$ are

$$\mu_{\parallel}(r) = \frac{H_1(d)}{d} - \frac{2}{\pi d^2} - \frac{Y_0(d) + Y_2(d)}{2}, \tag{3.109a}$$

$$\mu_{\perp}(r) = H_0(d) - \frac{H_1(d)}{d} + \frac{2}{\pi d^2} - \frac{Y_0(d) - Y_2(d)}{2}, \tag{3.109b}$$

where H_ν and Y_ν are, respectively, Struve functions and Bessel functions of the second kind of order ν, and

$$d = \frac{r\eta}{\eta_s} = \frac{r}{\ell_{\mathrm{SD}}}, \tag{3.110}$$

is distance scaled by the Saffman-Delbrück length ℓ_{SD} (3.102). Alternatively, non-dimensionalizing r by the probe size R makes d in (3.110) equivalent to

$$d = \frac{\tilde{r}}{Bq}, \tag{3.111}$$

where $Bq = \eta_s/\eta R$ is the Boussinesq number (3.99).

Momentum transport is interface-dominated over length scales smaller than ℓ_{SD} ($d \ll 1$ or $Bq \gg 1$), and the mobility coefficients (3.109) become

$$\mu_{\parallel}(r \ll \ell_{\mathrm{SD}}) \approx \frac{1}{\pi}\left(-\log\left(\frac{d}{2}\right) + \frac{1}{2} - \gamma_E\right), \tag{3.112a}$$

$$\mu_{\perp}(r \ll \ell_{\mathrm{SD}}) \approx \frac{1}{\pi}\left(-\log\left(\frac{d}{2}\right) + \frac{1}{2} - \gamma_E\right). \tag{3.112b}$$

To within an additive constant, the interfacial velocity driven by a point force in the $Bq \to \infty$ (or $d \to 0$) limit is then

$$\boldsymbol{u}_s(\boldsymbol{x}, Bq \to \infty) = \frac{1}{4\pi\eta_s}\left[-\log(r)\boldsymbol{I} + \frac{\boldsymbol{r}\boldsymbol{r}}{r^2}\right]\cdot \boldsymbol{F}, \tag{3.113}$$

which is, indeed, the 2D Stokeslet.

The logarithmic divergence in (3.113) as $r \to \infty$ reflects the Stokes paradox, which is here resolved by viscous traction from the subphase. Subphase viscous stresses become dominant over length scales larger than ℓ_{SD} ($d \gg 1$ or $Bq \ll 1$), in which case

$$\mu_{\parallel}(r \gg \ell_{\mathrm{SD}}) \approx \frac{2}{\pi d} - \frac{2}{\pi d^2}, \tag{3.114a}$$

$$\mu_{\perp}(r \gg \ell_{\mathrm{SD}}) \approx \frac{2}{\pi d^2}. \tag{3.114b}$$

The surface velocity profile becomes

$$\boldsymbol{u}_s(\boldsymbol{x}, Bq \to 0) = \frac{1}{2\pi\eta}\frac{\boldsymbol{rr}}{r^3} \cdot \boldsymbol{F} \tag{3.115}$$

in the surface-inviscid limit ($Bq \to 0$). Notably, (3.115) is *not* a 2D slice of the flow due to a 3D Stokeslet – surface incompressibility (§3.3.2) modifies fluid streamlines to ensure that the resultant velocity profile is surface-divergence free (figure 11).

Prasad *et al.* (2006) experimentally mapped out surface velocities on surface-viscous protein monolayers via passive (colloid-tracking) two-particle microrheology. The displacement correlations between two points on the interface along and perpendicular to the line joining their centers are proportional to mobility coefficients $\mu_{\parallel}$ and $\mu_{\perp}$, respectively. Experiments over a wide range of surface viscosities (from $O(1)$ nNs/m to $O(1)$ μNs/m) clearly show this transition from a logarithmic decay in the interface-dominated regime to $\mu_{\parallel} \sim 1/r$ and $\mu_{\perp} \sim 1/r^2$ when subphase stresses dominate (figure 13). Surface streamlines following (3.108) also transition distinctly between subphase-dominant and interface-dominant flows (figure 14).

3.4.3. Intrinsic and apparent surface viscosity—As discussed in §3.3, surface flows that compress or dilate the interface establish surfactant concentration gradients, generating Marangoni stresses. Surfactant exchange with the subphase returns the system to equilibrium. For small departures from equilibrium, the Marangoni stress due to a soluble surfactant (3.89) is

$$-\boldsymbol{\nabla}_s \Pi = E_0 \tau_s \boldsymbol{\nabla}_s(\boldsymbol{\nabla}_s \cdot \boldsymbol{u}_s), \tag{3.116}$$

where E_0 is the Marangoni modulus (2.22), and τ_s is the characteristic sorption time (3.56). Using (3.116) in the Boussinesq-Scriven equation (3.94) gives

$$-\boldsymbol{n} \cdot [\![\, \boldsymbol{\sigma} \,]\!] = \eta_s \nabla_s^2 \boldsymbol{u}_s + (E_0\tau_s + \kappa_s)\boldsymbol{\nabla}_s(\boldsymbol{\nabla}_s \cdot \boldsymbol{u}_s). \tag{3.117}$$

As noted previously in §3.3.2, adsorption/desorption introduces an *apparent* dilatational surface viscosity $\kappa_s^{\mathrm{ads}} = E_0\tau_s$. Equation (3.117) highlights the pitfalls of inferring a 'true' dilatational surface viscosity of a soluble surfactant. Any measurement that is sensitive to surface viscous dissipation due to pure compression/dilatation would at best report $\kappa_s + E_0\tau_s$. An intrinsic dilatational surface viscosity κ_s, should it exist, can only be established with complementary measurements of E_0 and τ_s.

Furthermore, (3.117) reveals the coupling between surface shear and dilatation in one-dimensional stretching or compression, as occurs in plate coating or thin-film drainage (§4.4). The 1D version of (3.117) corresponding to deformation along the x-direction is

$$\eta \frac{\partial v_x}{\partial z}\bigg|_{z=0} = (E_0\tau_s + \eta_s + \kappa_s)\frac{\partial^2 u_s}{\partial x^2}. \tag{3.118}$$

Surface viscous dissipation in 1D derives from a combination of surface shear viscosity, surface dilatational viscosity, and the apparent viscous-like term $E_0\tau_s$. Surface *shear* viscosity inferred from such systems, therefore, is also prone to mischaracterization when $E_0\tau_s \neq 06$. This rate- and system-dependent viscous-like contribution arising from adsorption/desorption is responsible, at least in part, for widely dissimilar values (spread over four orders of magnitude) reported for the surface viscosity of the same soluble surfactant (Stevenson 2005; Zell *et al.* 2014).

Nondimensionalizing (3.118) gives

$$\frac{\partial \tilde{v}_x}{\partial \tilde{z}}\bigg|_{z=0} = \Psi \frac{\partial^2 \tilde{u}_s}{\partial \tilde{x}^2}, \tag{3.119}$$

wherein Ψ reflects a general 'degree of immobilization' in 1D systems:

$$\Psi = \frac{(E_0\tau_s + \eta_s + \kappa_s)}{\eta L} = Ma_K + Bq_\eta + Bq_\kappa. \tag{3.120}$$

Here, $Bq_{\eta,\kappa}$ are Boussinesq numbers defined separately for the intrinsic surface shear and surface dilatational viscosities. Written this way, the exchange Marangoni number $Ma_K = E_0\tau_s/\eta L$ (table 3) can be interpreted as a modified Boussinesq number defined with the apparent surface dilatational viscosity, $\kappa_s^{\text{ads}} = E_0\tau_s$, in place of an intrinsic surface viscosity.

The immobilization parameter Ψ controls the transition from a stress-free interface ($\Psi \to 0$) to a no-slip surface ($\Psi \to \infty$) in 1D compression/dilatation. In the following sections, we will see this combination appear in the contexts of settling drops, coating flows, and foams. In each of these applications, a macroscopically measureable quantity (such as the velocity of a settling drop) depends on Ψ in a manner that does not differentiate between η_s, κ_s, and $E_0\tau_s$.

4. Surfactant dynamics in paradigmatic problems

Having discussed surfactant properties and their role in modifying fluid flows, we now turn to quantifying the effect of dynamic surfactant properties and processes on a series of paradigmatic problems. In particular, we will explore the motion of surfactant-covered drops and bubbles (§4.1), oscillatory compression of interfaces (§4.2), damping of surface waves (§4.3), coating and drainage of thin films (§4.4), flow through foams (§4.5), and particles and probes on surfactant-laden interfaces (§4.6). In each case, our objective is to identify the distinct ways in which surfactant dynamics impact measurable properties, such as the buoyant rising velocity of a bubble, the thickness of fluid entrained in dip coating, or the

drag on a probe translating on an interface. When possible, we quantify how each effect scales with system properties, geometries, and material parameters. In so doing, we aim to connect common threads that underlie these very different systems. Perhaps more importantly, we will highlight situations where it is difficult, or even impossible, to tease apart these processes in a typical experiment. Complementary experiments might be required to unambiguously identify the 'hidden' surfactant and/or transport variable responsible for the observed dynamics.

4.1. Motion of surfactant covered drops and bubbles

We will start with the 'simple' example that initially motivated this entire perspective – the motion of surfactant covered drops and bubbles (figure 1). Distinct surfactant processes manifest in often indistinguishable ways, even in such a mundane flow. In this section, we will quantitatively examine the impact of surfactant variables – specifically, surface viscous dissipation, Marangoni stresses as impacted by adsorption/desorption, and surface diffusion – in modifying the motion of a drop or bubble at low Reynolds numbers (figure 15).

The translation of a rigid sphere in a viscous fluid is a classic low-Reynolds-number problem. The terminal velocity of a rigid sphere of density ρ' and radius R settling due to its own weight (or rising due to buoyancy) through a liquid with viscosity η and density ρ is

$$U_{\text{rigid}} = \frac{2}{9}\frac{(\rho' - \rho)gR^2}{\eta}, \tag{4.1}$$

where g is the gravitational acceleration. A *clean* drop (or bubble) with viscosity η' of the same size settling (or rising) through the same liquid instead follows the Hadamard-Rybczynski formula (Levich 1962; Happel & Brenner 1965):

$$U_{\text{HR}} = \frac{2}{3}\frac{(\rho' - \rho)gR^2}{\eta}\frac{\eta + \eta'}{2\eta + 3\eta'} = U_{\text{rigid}}\frac{\lambda + 1}{\lambda + 2/3}, \tag{4.2}$$

where

$$\lambda = \frac{\eta'}{\eta} \tag{4.3}$$

is the viscosity ratio. Equation (4.2) recovers the Stokes formula (4.1) when $\lambda \gg 1$. By contrast, $U_{\text{HR}} = (3/2)U_{\text{rigid}}$ when $\lambda \ll 1$, such as an air bubble rising through a viscous fluid.

The picture changes when surfactants populate the interface between the two fluids. The interfacial boundary condition is then controlled by the interplay between convection, kinetics of adsorption/desorption, diffusion both in the bulk and on the interface, and surface viscous stresses (figure 1). Early experiments revealed discrepancies with the Hadamard-Rybczynski formula, and were attributed to impurities that modify the surface tension. In particular, Bond & Newton (1928) established that drops with radius under a critical value settle like rigid spheres, whereas larger drops followed (4.2). They suggested that internal circulation occurs only when the driving force (i.e.gravity) is much larger than the surface tension force, giving the critical radius $R^2 \ll \gamma/(\rho' - \rho)g$. The well-known Bond(-Newton)

number derives directly from this study. However, as we show in what follows, later studies have established that this change in the settling velocity can be attributed to dynamic surfactant processes, rather than the equilibrium surface tension.

4.1.1. Surface immmobilization due to surface viscosity—One of the first quantitative attempts to address the inconsistency between (4.2) and measurements came from Boussinesq (1913), who hypothesized that a thin interfacial layer provides its own 'surface viscous' resistance. In writing the tangential surface stress balance, Boussinesq neglected surface tension gradients and instead introduced a surface viscosity:

$$\boldsymbol{n}\cdot\quad[\![\,\boldsymbol{\sigma}\,]\!]\quad\cdot\boldsymbol{t}=\kappa_s\boldsymbol{t}\cdot\boldsymbol{\nabla}_s(\boldsymbol{\nabla}_s\cdot\boldsymbol{u}_s)\,. \tag{4.4}$$

Here, $\boldsymbol{n}$ and $\boldsymbol{t}$ are the normal and tangent, respectively, to the drop surface, $[\![\,\boldsymbol{\sigma}\,]\!]$ is the stress jump across the interface, and κ_s is an interfacial dilatational viscosity. Solving the boundary-value problem with (4.4) as the boundary condition, the terminal settling velocity of a drop is (Boussinesq 1913; Levich 1962; Agrawal & Wasan 1979)

$$U=U_{\text{rigid}}\frac{3\eta+3\eta'+2\vartheta}{2\eta+3\eta'+2\vartheta}, \tag{4.5}$$

where

$$\vartheta=\frac{\kappa_s}{R} \tag{4.6}$$

is a retardation coefficient due to surface dilatational viscosity. Thus, surface viscosity has an effect analogous to increasing the effective viscosity of the drop from η' to $\eta'+2\vartheta/3$.

The retardation coefficient ϑ has units of bulk shear viscosity, and can be argued based on excess energy dissipation. The energy dissipated in the drop via conventional shear viscosity scales like

$$P\sim\eta'\dot{\epsilon}^2R^3, \tag{4.7}$$

where $\dot{\epsilon}$ is the strain rate within the fluid; the dissipation per unit volume then becomes

$$\Phi\sim\eta'\dot{\epsilon}^2\,. \tag{4.8}$$

By extension, the retardation coefficient ϑ scales like the surface-excess energy P_s dissipated by the surfactant, normalized by the volume of the drop:

$$\Phi_s\sim\frac{P_s}{R^3}\sim\vartheta\dot{\epsilon}^2\,. \tag{4.9}$$

The Boussinesq number quantifies the relative strength of surface and bulk viscous stresses:

$$Bq_\kappa = \frac{\vartheta}{\eta} = \frac{\kappa_s}{\eta R}, \tag{4.10}$$

and the drop settling speed (4.5) can be rewritten as

$$U = U_{\text{rigid}} \frac{\lambda + 1 + 2Bq_\kappa/3}{\lambda + 2/3 + 2Bq_\kappa/3}. \tag{4.11}$$

Surface viscosity is negligible when $Bq_\kappa \ll 1$, whereas the interface is effectively immobilized and the drop behaves like a rigid sphere when surface viscous stresses dominate ($Bq_\kappa \gg 1$). Because Bq_κ decreases as R increases, Boussinesq's calculation reveals that bulk viscous stresses dominate over surface viscous stresses for sufficiently large drops. For fixed λ and κ_s, therefore, the Hadamard-Rybczynski prediction improves with an increase in drop size.

4.1.2. Marangoni stress and adsorption/desorption—The Boussinesq correction due to surface viscosity does not explicitly account for the Marangoni flow associated with surface tension gradients. Levich (1962) accounted for convection, adsorption/desorption and diffusion in both the surface and the bulk. When drops or bubbles translate, the interfacial fluid motion advects adsorbed molecules to the rear (figure 15 *c*), thereby establishing a gradient in Γ. This sets up reverse Marangoni flows, and the tangential stress balance at the interface becomes

$$\boldsymbol{n} \cdot \llbracket \boldsymbol{\sigma} \rrbracket \cdot \boldsymbol{t} = -\boldsymbol{t} \cdot \boldsymbol{\nabla}_s \gamma. \tag{4.12}$$

The strength of Marangoni stresses depends on the speed with which gradients are established, compared with how quickly various processes can cause them to relax. For small departures from equilibrium surface coverage, the terminal velocity takes the same form as (4.5), but with a retardation coefficient ϑ that depends on the dominant surfactant transport process (Levich 1962; Agrawal & Wasan 1979). In what follows, we outline the cases of adsorption and surface diffusion as the rate-limiting steps to illustrate the relative strength of Marangoni flows in immobilizing the interface.

The adsorption/desorption of soluble surfactants contributes an *apparent* dilatational surface viscosity (§3.4.3),

$$\kappa_s^{\text{app,ads}} = E_0 \tau_s, \tag{4.13}$$

where $E_0 = \Gamma_0 |\partial\gamma/\partial\Gamma|$ is the Marangoni modulus and τ_s is the sorption time (3.56). The retardation coefficient in this case is identical to (4.6) but with $\kappa_s^{\text{app,ads}}$ in place of an intrinsic dilatational surface viscosity κ_s (Levich 1962):

$$\vartheta_K = \frac{E_0 \tau_s}{R}. \tag{4.14}$$

The drop settles at a velocity

$$U = U_{\text{rigid}} \frac{\lambda + 1 + 2Ma_K/3}{\lambda + 2/3 + 2Ma_K/3}, \tag{4.15}$$

where the strength of Marangoni-induced retardation relative to bulk viscous drag defines the exchange Marangoni number (table 3):

$$Ma_K = \frac{\vartheta_K}{\eta} = \frac{E_0 \tau_s}{\eta R}. \tag{4.16}$$

Marangoni flows immobilize the interface ($U \to U_{\text{rigid}}$) when surfactant exchange with the bulk fluid is slow ($\tau_s \gg \tau_m = \eta R/E_0$), so that $Ma_K \gg 1$. For the same fluid and surfactant properties, smaller drops (with $R \ll E_0 \tau_s/\eta$) settle like rigid spheres, whereas larger drops follow the Hadamard-Rybczynski prediction.

As discussed in §3.2, the timescale τ_s depends on bulk diffusion gradients if exchange kinetics at the interface are sufficiently fast ($\tau_s \approx \tau_d$, $\tau_k \approx 0$). Additionally, if the bulk concentration C is above the critical micelle concentration (CMC), micelles act as surfactant reservoirs that dissociate to maintain a constant monomer concentration. As bulk concentration gradients vanish, $\tau_s \approx \tau_d \to 0$, and surface concentration gradients also disappear (figure 15 *d*). Micelles thus act to diminish reverse Marangoni flows and reduce adsorption/desorption-based retardation by 'remobilizing' the interface (Stebe & Maldarelli 1994).

4.1.3. Marangoni stress and surface diffusion—Diffusion of surfactant molecules on the interface can also relax surface concentration gradients, particularly when the surfactant is insoluble. Surface diffusion acts against gradients in Γ established by surfactant advection, and the resultant profile $\gamma(\Gamma)$ dictates the strength of the Marangoni reverse flow. Solving for a dilute system that is slightly perturbed from equilibrium, Levich (1962) obtained (4.5) again, but now with the retardation coefficient

$$\vartheta_{\text{sd}} = \frac{RE_0}{D_s}, \tag{4.17}$$

where D_s is the surface diffusivity of the surfactant.

This retardation coefficient captures the work dissipated as surfactant molecules are forced along the interface by chemical potential gradients. The rate of work done by a surfactant molecule of mobility b_s forced to translate along the interface at velocity U is $U^2/b_s \sim \dot{\epsilon}^2 R^2/b_s$, and the surface excess power P_s dissipated by $\sim \Gamma R^2$ surfactants is

$$P_s \sim \frac{\Gamma \dot{\epsilon}^2 R^4}{b_s}. \tag{4.18}$$

Following (4.9), the retardation coefficient ϑ_{sd} is then related to the dissipation Φ per unit volume of the drop,

$$\Phi \sim \frac{P_s}{R^3} \sim \left(\frac{R\Gamma}{b_s}\right)\dot{\epsilon}^2 \sim \vartheta_{sd}\dot{\epsilon}^2 . \tag{4.19}$$

The term within the brackets is the 3D-viscosity-like coefficient ϑ_{sd} associated with dissipation in this process. In the dilute limit, the Marangoni modulus E_0 and surface concentration Γ are related via $\Gamma = E_0/k_BT$, and the surface mobility and diffusivity are related via the Stokes-Einstein relation $D_s = k_BTb_s$. Substituting Γ and b in (4.19) recovers Levich's form (4.17) for the retardation coefficient ϑ_{sd}.

The surface diffusion of insoluble surfactants thus modifies the droplet settling velocity to

$$U = U_{\mathrm{rigid}} \frac{\lambda + 1 + 2Ma_D/3}{\lambda + 2/3 + 2Ma_D/3} . \tag{4.20}$$

where the Marangoni number Ma_D (table 3) is

$$Ma_D = \frac{\vartheta_{\mathrm{sd}}}{\eta} = \frac{RE_0}{\eta D_s} . \tag{4.21}$$

The interface is immobilized by reverse Marangoni flow ($U \to U_{\mathrm{rigid}}$) when the surface diffusive timescale R^2/D_s is much longer than the Marangoni timescale $\eta R/E_0$ (or $Ma_D \gg 1$). By contrast, the surface is mobile if $Ma_D \ll 1$, in which case surface diffusion relaxes surface concentration gradients quickly enough that Marangoni flows do not develop.

It is tempting to express ϑ_{sd} from (4.17) in terms of an *apparent* surface viscosity, following (4.6), giving

$$\kappa_s^{\mathrm{app,sd}} = \frac{R^2E_0}{D_s} = E_0\tau_d, \tag{4.22}$$

where $\tau_d = R^2/D_s$ is the surface diffusive timescale. In this case, however, the apparent surface viscosity $\kappa_s^{\mathrm{app,sd}}$ depends on the size of the drop, and therefore clearly does not represent an intrinsic material property. By extension, the R^2 dependence of $\kappa_s^{\mathrm{app,sd}}$ differs from both intrinsic surface viscosity κ_s and as well as the apparent κ_s^{app} due to other dynamic surfactant processes like adsorption/desorption (4.13), suggesting experimental strategies to differentiate between the possible mechanisms.

4.1.4. Inferring retardation mechanisms from measurements—The three different mechanisms of surface stress relaxation considered here – surface viscosity, Marangoni reverse flow with adsorption/desorption, and Marangoni reverse flow with surface diffusion – all lead to drop settling velocities of the form

$$U = U_{\mathrm{rigid}} \frac{\lambda + 1 + 2\Psi/3}{\lambda + 2/3 + 2\Psi/3} . \tag{4.23}$$

The immobilization parameter Ψ (§3.4.3) acts in way that resembles an increase in the shear viscosity of the drop. The drop settles like a rigid sphere when $\Psi \to \infty$, and like a clean drop when $\Psi \to 0$. Equation (4.23) qualitatively maps out the illustrative plot in figure 1, where Ψ is determined by the 'hidden' surfactant variable(s). More general immobilization parameters $\Psi = \Psi(Ma, Pe, Da, Bq_\kappa)$ arise when surfactant transport in the bulk becomes comparable to surface processes (Levich 1962; Agrawal & Wasan 1979), but the form of (4.23) remains unchanged. Here, the Péclet number $Pe = UR/D$ compares advection and diffusion in the bulk, and the Damköhler number $Da = k_C R/D$ compares adsorption to bulk diffusion.

Experimentally measuring drop settling velocity U alone can not reveal exactly what the surfactant does to the interface. Equation (4.23) links a measured velocity to the parameter Ψ, which could be Bq_κ, some form of Ma, a function of Pe and Da, or some non-trivial combination. How can we, if at all, demarcate the specific process responsible for slowing the drop?

Since one can at best measure the lumped parameter Ψ, one approach is to exploit the scaling of Ψ with experimentally controllable quantities such as the bubble radius or surfactant concentration. If Ψ, interpreted from measurements via (4.23), increases linearly with drop size, then Marangoni flow with surface diffusion would be consistent as the dominant mechanism ($\Psi = Ma_D$). Alternatively, if experiments suggest $\Psi \propto 1/R$, surface viscosity ($\Psi = Bq_\kappa$), adsorption-based retardation ($\Psi = Ma_K$), or both would be consistent. However, one might expect these two mechanisms to scale differently with bulk surfactant concentration C: an intrinsic surface viscosity κ_s likely increases with C or stays constant, whereas $\kappa_s^{\text{app,ads}}$ likely decreases with C, since adsorptive equilibration speeds up as more surfactant is added to the bulk.

4.2. Oscillatory compression of soluble monolayers

The oscillatory compression of surfactant monolayers – whether in Langmuir troughs or in pulsing bubbles – provides an important method to characterize interfaces and the impact of surfactant processes on surface mechanics (Lucassen & van den Tempel 1972; Johnson & Stebe 1994; Ravera *et al.* 2010; Arriaga *et al.* 2010; Kotula & Anna 2016). The mechanical response of a dynamic interface as it is compressed depends not only on the equilibrium properties (via the isotherm) but also on the surface concentration profile $\Gamma(\boldsymbol{r}_s, t)$ at any particular position and time. By extension, the Gibbs modulus E of soluble surfactants depends on the relative timescales of interfacial compression/dilatation and re-equilibration of Γ. For example, during a compression so rapid that surfactants do not have time to desorb, the surface concentration must increase as $\Gamma \sim 1/A$, so that

$$E^{\text{soluble}}(t \to 0) = -A\frac{\partial \Pi}{\partial A}\bigg|_{t\to 0} \approx \Gamma\frac{\partial \Pi}{\partial \Gamma}\bigg|_{t\to 0} = E_0 . \tag{4.24}$$

In other words, the Gibbs modulus E is equal to the Marangoni modulus E_0 in the rapid deformtion limit. By contrast, over long enough time scales, adsorption/desorption returns Γ (and therefore Π) to its equilibrium level, so that

$$E^{\text{soluble}}(t \to \infty) = -A\frac{\partial \Pi}{\partial A}\Big|_{\Pi \approx \text{constant}} \approx 0 \tag{4.25}$$

for slow (or quasi-static) compression.

In general, the Gibbs modulus measured during the oscillatory compression of a soluble monolayer ranges between 0 and E_0. Moreover, $\Gamma(t)$ may oscillate with some phase lag relative to the oscillating surface area A, as discussed in §3.2.1. Just like in shear rheology, out-of-phase responses reflect dissipative processes, meaning that the dynamic Gibbs modulus captures the apparent surface elasticity and the apparent surface dilatational viscosity, both of which depend on frequency. In what follows, we will revisit classic studies that quantified the apparent rate-dependent surface viscoelasticity originating from surfactant exchange between interface and subphase during oscillatory compression.

4.2.1. Apparent oscillatory surface rheology—Lucassen & van den Tempel (1972) computed the surface pressure $\Pi(t)$ on a planar surfactant monolayer whose area $A(t)$ is forced to oscillate, and connected the monolayer response to a rate-dependent surface viscoelasticity. Figure 16 depicts the model system, consisting of a soluble monolayer at $z = 0$ subjected to an oscillatory dilatational deformation at frequency ω (*e.g.* by moving barriers in a Langmuir trough), while surfactants adsorb/desorb over a timescale τ_s.

As discussed in §3.2, the molecular exchange of surfactant between the surface and the subphase can be diffusion- or kinetically-limited. Lucassen & van den Tempel (1972) focused on the diffusion-limited regime ($Da \gg 1$), for which the sorption timescale $\tau_s \approx \tau_d \sim L_d^2/D$. The equilibrium surface area, surface concentration, and bulk concentration fields are perturbed via

$$A(t) = A_0 + \delta A e^{i\omega t}, \tag{4.26a}$$

$$\Gamma(t) = \Gamma_0 + \delta\Gamma e^{i\omega t}, \tag{4.26b}$$

$$C(z,t) = C_0 + \delta C e^{i(\omega t + kz)}, \tag{4.26c}$$

where the disturbance is homogeneous along the interface, and surfactant is dissolved in the bulk fluid below the interface ($z < 0$). The bulk concentration C satisfies the diffusion equation (3.26), with solution

$$k = (1-i)\sqrt{\frac{\omega}{2D}}. \tag{4.27}$$

Both real and imaginary components of $\delta\Gamma$ resist interfacial dilatation, and a convenient measure of the net resistance is the *complex* dilatational modulus

$$E^* = -\frac{\mathrm{d}\Pi}{\mathrm{d}\ln A} = -\frac{\mathrm{d}\Pi}{\mathrm{d}\ln \Gamma}\frac{\mathrm{d}\ln \Gamma}{\mathrm{d}\ln A} = -E_0\frac{\mathrm{d}\ln \Gamma}{\mathrm{d}\ln A}, \tag{4.28}$$

where $E_0 = \mathrm{d}\Pi/\mathrm{d}\ln\Gamma$ is the Marangoni modulus (§2.4.2). We will assume that $\Pi(t)$ is in phase with and uniquely determined by $\Gamma(t)$, so that E_0 is independent of ω. Note, however, that Γ and A may not vary precisely in phase: even monolayers of insoluble surfactant monolayers may relax to equilibrium over surprisingly long times, as discussed in §5. Surfactant transport thus affects E^* via the dynamic behavior of $\Gamma(A)$ in (4.28). The real part of E^* is the dynamic Gibbs modulus, whereas the imaginary or out-of-phase component captures the viscous-like dissipation associated with surfactant exchange.

Surfactant conservation at the interface with diffusion-limited adsorption (§3.2) requires

$$\frac{1}{A}\frac{\partial(\Gamma A)}{\partial t} = j_{\mathrm{diff}} = -D\frac{\partial C}{\partial z}\bigg|_{z=0}. \tag{4.29}$$

Contact equilibrium is assumed between the surface concentration $\Gamma(t)$ and the bulk concentration $C_s(t) = C(0, t)$ when diffusion-controlled, so that

$$\frac{1}{A}\frac{\partial(\Gamma A)}{\partial t} = \left(1+\frac{\partial\ln\Gamma}{\partial\ln A}\right)\frac{\partial\Gamma}{\partial t} = \left(1+\frac{\partial\ln\Gamma}{\partial\ln A}\right)L_p\frac{\partial C}{\partial t}\bigg|_{z=0}, \tag{4.30}$$

where $L_p = \partial\Gamma/\partial C_s$ is the depletion depth (3.47). Using (4.30) in (4.29) gives

$$\frac{\partial\ln\Gamma}{\partial\ln A} = -\left(1+\frac{D}{L_d}\frac{\partial C/\partial z|_{z=0}}{\partial C/\partial t|_{z=0}}\right)^{-1}. \tag{4.31}$$

Substituting perturbed variables (4.26) in (4.31) then gives the complex modulus (4.28):

$$E^* = \frac{E_0}{1+\zeta_d - i\zeta_d}, \tag{4.32}$$

where

$$\zeta_d = \frac{1}{L_d}\sqrt{\frac{D}{2\omega}} \tag{4.33}$$

is a dimensionless ratio of the diffusive boundary layer thickness $\delta_{\mathrm{BL}} = \sqrt{D/2\omega}$ to the depletion depth $L_p = \partial\Gamma/\partial C_s$, first introduced as (3.51) in §3.2.

The apparent surface-elastic and surface-viscous moduli are the real and imaginary parts of E^*, respectively:

$$E = \mathrm{Re}[E^*] = E_0\frac{1+\zeta_d}{1+2\zeta_d+2\zeta_d^2}, \tag{4.34a}$$

$$\kappa_s^{\text{ads}} = \frac{\text{Im}[E^*]}{\omega} = \frac{E_0}{\omega}\frac{\zeta_d}{1+2\zeta_d+2\zeta_d^2}. \tag{4.34b}$$

During 'fast' oscillations ($\zeta_d \ll 1$), surfactant molecules do not diffusively escape the depletion depth before the barrier reverses direction, so the interface behaves as insoluble, with $E \to E_0$. By contrast, during 'slow' oscillations ($\zeta_d \gg 1$), the oscillatory boundary layer is thicker than the depletion depth ($\delta_{\text{BL}} \gg L_p$). In this limit, dissolved molecules diffuse across the depletion depth during each oscillation and restore the sublayer concentration to C_0 before the barrier reverses. Molecules then adsorb/desorb much more quickly than the interface is compressed and dilatated, so that $\Gamma(t) \approx \Gamma_0$ and the Gibbs modulus vanishes. The apparent dilatational surface viscosity κ_s^{ads} is highest when $\zeta_d = O(1)$, i.e., when $\tau_\omega \sim \tau_d$.

More generally, the complex dilatational modulus E^* depends on the Damköhler number Da (3.40). We will generalize E^* for finite Da and non-planar interfaces in the next section, but simply note that the qualitative trends of E^* resemble those in Figure 16*b*, regardless of system geometry: $|E^*| \to E_0$ for slow adsorption/desorption (or rapid deformation), and $|E| \to 0$ for slow deformations.

4.2.2. Oscillating bubble tensiometry—Oscillating bubbles make excellent experimental probes of dilatational surface rheology (Kotula & Anna 2016; Ravera *et al.* 2010). Indeed, §3.2.1 illustrated kinetically and diffusion-limited surfactant exchange via oscillating bubbles. Here, we will follow Johnson & Stebe (1994) in examining the surface stresses that arise in oscillating bubbles, and how they depend on adsorption/desorption, surface rheology, and subphase viscosity.

Alvarez *et al.* (2010*a*) developed a microbubble microtensiometer, which simultaneously measures radius the radius and gas pressure of $\mathcal{O}(100\mu\text{m})$ bubbles. For a static bubble with equilibrated surface coverage, the surface tension (or surface pressure) is then determined via the Young-Laplace equation (2.6). Indeed, the equilibrium isotherm of insoluble monolayers can be mapped out by quasi-static compression of a spherical bubble (Kotula & Anna 2016).

To quantify the impact of surfactant adsorption/desorption,mass transport and surface rheology on dynamic bubbles, we return to the work of Johnson & Stebe (1994), first introduced in §3.2.1, involving an oscillating air bubble of radius $R(t)$, with dynamic surface concentration $\Gamma(t)$, in a liquid containing dissolved surfactant at concentration $C(t)$. Fluid pressure and radial velocity in both gas and liquid phases are perturbed as before (3.29), via

$$v_r(r,t) = \delta v_r(r)e^{i\omega t}, \quad p(r,t) = p_0 + \delta p(r)e^{i\omega t}. \tag{4.35}$$

Solving the unsteady Stokes equations gives

$$\delta v(r) = \frac{i\omega R_0^2}{r^2}\delta R, \tag{4.36a}$$

$$\delta p(r) = -\frac{\rho\omega^2 R_0^2}{r}\delta R, \tag{4.36b}$$

in the liquid phase.

Assuming the gas viscosity to be negligible, the gas pressure is uniform throughout the bubble ($p_g = p_g(R)$) and is determined by the stress balance at the interface (3.8). Assuming also that the adsorbed surfactant forms a Newtonian monolayer and simplifying the Boussinesq-Scriven stress tensor (3.93) for radial deformation gives (Scriven 1960):

$$p_g - p_l(R) + 2\eta\left.\frac{\partial v_r}{\partial r}\right|_{r=R} = \frac{2\gamma}{R} + \frac{4\kappa_s v_r(R)}{R^2}. \tag{4.37}$$

The perturbed surface tension is

$$\gamma = \gamma(\Gamma_0) + \left.\frac{\partial\gamma}{\partial\Gamma}\right|_{\Gamma_0}\delta\Gamma e^{i\omega t} = \gamma_0 - \frac{E_0}{\Gamma_0}\delta\Gamma e^{i\omega t}, \tag{4.38}$$

so that the leading-order interfacial stress balance (4.37) is the Young-Laplace equation:

$$p_{g,0} - p_{l,0}(R_0) = \frac{2\gamma_0}{R_0}. \tag{4.39}$$

At $O(\delta R)$, however, the pressure jump at the interface has contributions due to Young-Laplace from the radial change, the resistance to dilatation due to changes in adsorbed surfactant concentration (and therefore Π), the viscous resistance from the bulk liquid, and dilatational surface viscous resistance:

$$\delta p_g - \delta p_l(R) = \left[-\frac{2\gamma_0}{R_0^2} + \frac{4E_0}{R_0^2}\frac{\delta\Gamma}{\delta\Gamma_{\text{insol}}} + \frac{4i\omega\eta}{R_0} + \frac{4i\omega\kappa_s}{R_0^2}\right]\delta R, \tag{4.40}$$

where

$$\delta\Gamma_{\text{insol}} = -2\Gamma_0\frac{\delta R}{R_0} \tag{4.41}$$

is the surface concentration change in the insoluble limit (3.32). Recall from §3.2.1 that $\delta\Gamma$ in (4.40) is complex, with components both in and out of phase with δR.

Nondimensionalizing length and pressure in (4.40) using R_0 and the Laplace pressure $2\gamma_0/R_0$ respectively gives

$$\delta\tilde{p}_g - \delta\tilde{p}_l(R) = \chi\delta\tilde{R}, \tag{4.42}$$

where

$$\chi = -1 + 2Ma_\gamma \frac{\mathrm{Re}[\delta\Gamma]}{\delta\Gamma_{\mathrm{insol}}} + 2iCa\left(1 + Bq_\kappa + Ma\frac{\mathrm{Im}[\delta\Gamma]}{\delta\Gamma_{\mathrm{insol}}}\right) \tag{4.43}$$

and the capillary, Marangoni, and Boussinesq numbers are

$$Ca = \frac{\eta R_0 \omega}{\gamma_0}, \quad Ma = \frac{E_0}{\eta R_0 \omega}, \quad Ma_\gamma = Ma \times Ca = \frac{E_0}{\gamma}, \quad Bq_\kappa = \frac{\kappa_s}{\eta R_0}. \tag{4.44}$$

Evaluating (4.42)–(4.44) requires the solution for $\delta\Gamma/\delta\Gamma_{\mathrm{insol}}$, described in §3.2.1 and given by (3.41) and reproduced here

$$\frac{\delta\Gamma}{\delta\Gamma_{\mathrm{insol}}} = \left[1 - i\,St\left(\frac{1+\sqrt{i\,Wo}}{1+\sqrt{i\,Wo}+Da}\right)\right]^{-1}, \tag{4.45}$$

where the Stanton, Womersley, and Damköhler numbers are

$$St = \frac{k_\Gamma}{\omega}, \quad Wo = \frac{\omega R_0^2}{D}, \quad \text{and} \quad Da = \frac{k_C R_0}{D}. \tag{4.46}$$

Surfactant-free bubbles lack surface viscous and surface elastic stresses ($Ma = Bq_\kappa = 0$). The interfacial stress balance (4.42) then recovers the linear limit of the classic Rayleigh-Plesset equation (Marmottant *et al.* 2005):

$$\left.\frac{\widetilde{\delta p_g} - \widetilde{\delta p_l}(R)}{\widetilde{\delta R}}\right|_{\mathrm{clean}} = -1 + 2iCa. \tag{4.47}$$

The normal stress jump balances the perturbed Laplace pressure due to change in radius and the viscous stress from the liquid phase.

Bubbles with insoluble surfactants have surface concentrations that change in phase with the oscillations, giving $\mathrm{Re}[\delta\Gamma] = \delta\Gamma_{\mathrm{insol}}$ and $\mathrm{Im}[\delta\Gamma] = 0$, so that (4.42) becomes

$$\left.\frac{\widetilde{\delta p_g} - \widetilde{\delta p_l}(R)}{\widetilde{\delta R}}\right|_{\mathrm{insol}} = -1 + 2Ma_\gamma + 2iCa + 2iBq_\kappa Ca. \tag{4.48}$$

The pressure jump across the interface then balances additional surface stresses: the terms proportional to Ma_γ and $Bq_\kappa Ca$ quantify the elastic and intrinsic surface viscous resistance to interfacial dilatation/compression, respectively.

Surface elastic resistance to bubble expansion decreases for soluble surfactants, however, since adsorption/desorption diminishes perturbations to surface concentration, and $\mathrm{Re}[\delta\Gamma] < \delta\Gamma_{\mathrm{insol}}$. Solubility also introduces an out-of-phase component of surface concentration, so that $\mathrm{Im}[\delta\Gamma] \neq 0$, giving rise to an additional surface-viscous-like stress as in §4.2.1.

The dynamic Gibbs modulus E and the apparent dilatational surface viscosity κ_s^{ads} are the real and imaginary parts of the complex modulus E^* (§4.2.1). For small oscillatory perturbations around a spherical bubble, (4.28) gives

$$\frac{E^*}{E_0} = -\frac{\mathrm{d}\ln\Gamma}{\mathrm{d}\ln A} = -\frac{R_0}{2\Gamma_0}\frac{\delta\Gamma}{\delta R} = \frac{\delta\Gamma}{\delta\Gamma_{\mathrm{insol}}}, \tag{4.49}$$

so that using (4.45) for $\delta\Gamma$ gives

$$\frac{E^*}{E_0} = \left[1 - i\,St\left(\frac{1+\sqrt{i\,Wo}}{1+\sqrt{i\,Wo}+Da}\right)\right]^{-1}. \tag{4.50}$$

Surfactant exchange between the interface and subphase is kinetically-limited when the bulk diffusion time τ_d is much smaller than the kinetic time τ_k (see §3.2.1). In the kinetically-limited ($Da = \tau_d/\tau_k \to 0$) case, (4.50) becomes

$$\frac{E^*_{\mathrm{kin}}}{E_0} = \frac{1}{1-iSt} = \frac{1}{1+St^2} + i\frac{St}{1+St^2}. \tag{4.51}$$

The monolayer is effectively insoluble, and the Gibbs modulus E approaches the Marangoni modulus E_0, in the limit that adsorption kinetics are so slow that $\Gamma(t)$ does not change appreciably before the oscillatory cycle reverses (or $St \to 0$). By contrast, $\Gamma(t)$ is approximately constant if adsorption/desorption is fast relative to bubble oscillations ($St \to \infty$), so that the monolayer provides no resistance to compression/dilatation. Bubble size does not affect E^*_{kin} when transport is kinetically-limited: the oscillatory mechanical response of a soluble planar monolayer (§4.2.1) also follows (4.51) in the kinetically-limited regime $Da \to 0$.

Alternatively, adsorption is diffusion-limited when $\tau_d \gg \tau_k$ (or $Da \gg 1$), and surface concentration rapidly equilibrates with the subsurface concentration $C_s(t) = C(R,t)$ via an isotherm $\Gamma(C_s)$. In the diffusion-controlled limit ($Da \to \infty$), (4.50) becomes

$$\frac{E^*_{\mathrm{diff}}}{E_0} = \frac{\Lambda_d Wo}{\Lambda_d W_O - i - i\sqrt{i\,W_O}}, \tag{4.52}$$

where $\Lambda_d = (\partial\Gamma/\partial C_s)/R_0$ is the dimensionless depletion depth (3.47). The monolayer behaves as if it were insoluble, so that $E^*_{\mathrm{diff}} \to E_0$ when diffusive transport is so slow that surfactants desorbed during bubble compression do not diffuse away before they readsorb during bubble expansion ($Wo \to \infty$). By contrast, $\Gamma(t)$ remains nearly in equilibrium if the bubble oscillates much more slowly than required for diffusion ($Wo \to 0$), in which limit the monolayer offers no resistance.

The real and imaginary parts of (4.52) correspond to the excess elastic and dissipative terms in (4.42). Separating these contributions and simplifying gives

$$\frac{E^*_{\text{diff}}}{E_0} = \frac{1+\zeta_d}{1+2\zeta_d+2\zeta_d^2\left(1+2\Lambda_d\zeta_d+2\Lambda_d^2\zeta_d^2\right)} + i\frac{\zeta_d(1+2\Lambda_d\zeta_d)}{1+2\zeta_d+2\zeta_d^2\left(1+2\Lambda_d\zeta_d+2\Lambda_d\zeta_d^2\right)}, \tag{4.53}$$

where

$$\zeta_d = \frac{1}{L_d}\sqrt{\frac{D}{2\omega}} \tag{4.54}$$

is the ratio of the diffusive oscillatory boundary layer thickness to the depletion depth (3.51),

$$L_d = \frac{\partial \Gamma}{\partial C_s}. \tag{4.55}$$

Bubbles with radii significantly larger than the depletion depth ($\Lambda_d = L_d/R \ll 1$) recover the classic results of Lucassen & van den Tempel (1972) for oscillatory compression of *planar* interfaces, presented in §4.2.1.

In the examples so far, the subphase was assumed to be infinitely deep so that the bulk fluid always contained enough surfactant to adsorb on to the interface given enough time. However, the bulk fluid may be entirely depleted of surfactant if the subphase is shallow, as may occur in thin films, coating flows, foams and concentrated emulsions. The film thickness h then 'cuts off' the depletion depth L_d, and the film is said to be confined (Quéré 1999; Delacotte *et al.* 2012). Surface concentration perturbations are not diminished by adsorption/desorption if $h \ll L_d$, and the effective dilatational modulus is maximal (equal to the Marangoni modulus E_0) for confined flows.

4.3. Damping of capillary waves

The calming effect of oil poured on the surface of water has been known among seafarers since the times of the ancient Greeks. Benjamin Franklin gave one of the earliest systematic accounts, claiming that a mere teaspoonful of oil was capable of rendering a half-acre pond "as smooth as a looking-glass" (Franklin *et al.* 1774). His own hypothesis was that the film of oil prevented wind from "catching" the water, in turn preventing friction by gliding on the surface and damping wave formation. However, wave damping occurs far too quickly to result from a reduction in wind input alone.

Instead, surfactants dissipate wave energy and therefore play the dominant role in wave damping (Levich 1962; Lucassen & Hansen 1966; Alpers & Hühnerfuss 1989). In what follows, we will first outline wave motion on a clean interface, and later contrast it with waves on surfactant-laden interfaces. The surfaces of clean fluids are dilated or compressed at the nodes of surface waves, and surface rheology or Marangoni stresses resist such a deformation. Large surface elasticity or surface viscosity makes the interface act as effectively incompressible, suppressing the propagation of surface waves.

4.3.1. Waves on a clean liquid surface—The vertical displacement ζ of a surface due to plane waves of wavelength λ propagating along the x direction (figure 17) can be written

$$\zeta(x,t) = \zeta_0 e^{i(kx-\omega t)}, \tag{4.56}$$

where $k = 2\pi/\lambda$ and ω are, respectively, the wave number and frequency. For small wave amplitudes, the nonlinear term in the Navier-Stokes equation is negligible (Levich 1962; Probstein 1994) and the hydrodynamic governing equations are the unsteady Stokes equations.

Waves are driven by the balance between fluid inertia and the restoring forces of gravity and/or surface tension. The excess hydrostatic pressure due to the disturbance is

$$p_g = \rho g \zeta, \tag{4.57}$$

and the excess capillary pressure, following the Young-Laplace equation and assuming small curvatures, is

$$p_c = -\gamma \frac{\partial^2 \zeta}{\partial x^2} = \gamma k^2 \zeta. \tag{4.58}$$

The ratio of hydrostatic and capillary pressures is the Bond number,

$$Bo = \frac{p_g}{p_c} = \frac{\rho g}{\gamma k^2}. \tag{4.59}$$

Short wavelengths ($Bo \ll 1$) correspond to capillary waves ($\lambda \lesssim O(1\text{cm})$ for water), whereas large wavelengths ($Bo \gg 1$) correspond to gravity waves.

Inviscid flows are simplest, as they are irrotational in this configuration, and can therefore be described by a velocity potential:

$$\boldsymbol{v} = \boldsymbol{\nabla}\phi, \quad \text{and} \quad \boldsymbol{\nabla}^2\phi = 0. \tag{4.60}$$

Linearity and continuity require

$$\phi(x,z,t) = A e^{kz} e^{i(kx-\omega t)}, \tag{4.61}$$

so that the linearized inviscid Navier-Stokes equation give

$$\left.\frac{\partial \phi}{\partial t}\right|_{z=0} = -\left(g + \frac{\gamma k^2}{\rho}\right)\zeta, \tag{4.62}$$

approximating the interface to be at $z = 0$, with $O(\zeta^2)$ corrections. Imposing the kinematic condition $D\zeta/Dt = v_z$ at the interface then gives

$$\omega_0 = \left(gk + \frac{\gamma k^3}{\rho}\right)^{1/2} = \sqrt{\frac{\gamma k^3}{\rho}}(1 + Bo)^{1/2}, \tag{4.63}$$

where Bo is the Bond number (4.59). From the dispersion relation (4.63), the wave velocity is given by

$$c = \frac{\omega_0}{k}, \tag{4.64}$$

with a minimum $c_{\min} \approx 20$ cm/s for water.

Waves described by (4.63) neither grow nor decay when the fluid is inviscid and the interface is clean. However, waves decay in fluids with finite viscosity. The relative strength of wave damping is captured by the ratio of viscous stresses to inertial stresses,

$$m = \frac{\nu k^2}{\omega_0} = \frac{2\pi\nu}{c\lambda}, \tag{4.65}$$

where $\nu = \eta/\rho$ is the kinematic viscosity. Based on the minimum phase velocity in water, $m < 1$ for wavelengths larger than $\lambda \gtrsim 0.1$mm (Levich 1962). Viscous stresses are therefore typically weak relative to inertia, and it is safe to assume that the wave frequency departs only slightly from its inviscid value ω_0, so that

$$\zeta(x,t) = \zeta_0 e^{i(kx - \omega_0 t) + \beta t}, \tag{4.66}$$

where $|\beta| \ll \omega_0$ gives a weak viscous damping. The negative real part of β is the decay rate, and its imaginary part gives a small correction to the wave frequency due to fluid viscosity.

The non-irrotational nature of viscous flows necessitates a stream function ψ in addition to the potential function ϕ. Solving for the velocity, pressure, and β based on ϕ and ψ is tedious – see Levich (1962) for details – here we simply present the resultant damping rate,

$$\beta_{\text{clean}} = \text{Re}[\beta] = -2m\omega_0 = -2\nu k^2. \tag{4.67}$$

The damping timescale $\beta_{\text{clean}}^{-1}$ can be interpreted as the time taken for vorticity generated by shear stresses to diffuse a depth comparable to the wavelength λ.

In what follows, we examine how surfactants modify the damping rate β. Levich (1962) shows the effect of surfactants to be significant only when $\lambda \lesssim 10$ cm, and therefore affect capillary waves more prominently than gravity waves. We will therefore restrict our attention to capillary waves ($Bo \ll 1$) in the following sections, and approximate $\omega_0 \approx \sqrt{\gamma k^3/\rho}$. As Franklin *et al.* (1774) noted over two centuries ago, large waves on a stormy sea are unaffected, whereas smaller ripples are smoothed out resulting in ‘glassy’ surfaces.

4.3.2. Marangoni damping due to insoluble and surface inviscid surfactants

—Surfactants strengthen wave damping through two main mechanisms – Marangoni

stresses and surface rheology – and we start with the former. The simplest case is a surface inviscid monolayer, for which $\eta_s = \kappa_s = 0$. Additionally, surface concentration gradients do not relax by adsorption/desorption in insoluble monolayers, in which case E is equal to the Marangoni modulus E_0 (§2.4.2). Surface diffusion may also weaken the Marangoni effect by smoothing out gradients in Γ, but we will neglect diffusion by assuming the time to diffuse the wavelength λ^2/D_s is much longer than the oscillation period ω_0.

The surface concentration is perturbed away from its equilibrium value Γ_0 via

$$\Gamma(x,t) = \Gamma_0 + \delta\Gamma e^{i(kx-\omega_0 t)+\beta t}, \tag{4.68}$$

where $\delta\Gamma \ll \Gamma_0$. Like with the vertical displacement $\zeta(x, t)$ (4.66), we assume that subphase viscous effects are weak, so that the frequency is well-approximated by its inviscid value ω_0, and that the damping rate $|\beta| \ll \omega_0$. For small surface velocities, the surfactant conservation equation (3.10) gives

$$\delta\Gamma e^{i(kx-\omega_0 t)+\beta t} = \frac{\Gamma_0}{-i\omega_0+\beta}\frac{\partial v_x}{\partial x} \tag{4.69}$$

to leading order, so that the normal and tangential stress boundary conditions (3.8) for a surface-inviscid monolayer are:

$$-p + 2\eta\frac{\partial v_z}{\partial z} = \gamma(\Gamma_0)\frac{\partial^2\zeta}{\partial x^2}, \tag{4.70a}$$

$$\eta\left(\frac{\partial v_x}{\partial z}+\frac{\partial v_z}{\partial x}\right) = -\frac{E_0}{\Gamma_0}\frac{\partial\Gamma}{\partial x} = \frac{E_0}{i\omega_0-\beta}\frac{\partial^2 v_x}{\partial x^2}. \tag{4.70b}$$

The capillary force in (4.70*a*) drives the wave, whereas the Marangoni stress in (4.70*b*) resists it. We therefore anticipate the damping rate β to depend on the relative magnitudes of $\gamma(\Gamma_0)$ and $E_0(\Gamma_0)$.

Solving the unsteady Stokes equations with boundary conditions (4.70) gives the fluid velocity and the damping rate β. The calculation is tedious, but analytically tractable, in the limits of weak viscosity ($m = \nu k^2/\omega_0 \ll 1$) and small damping rate ($|\beta| \ll \omega_0$), giving (Levich 1962; Alpers & Huühnerfuss 1989)

$$\frac{\mathrm{Re}[\beta]}{\omega_0} \approx -\frac{1}{2\sqrt{2}}\frac{Ma_\gamma^2\sqrt{m}-4Ma_\gamma m^{3/2}+4\sqrt{2}m^2}{Ma_\gamma^2+m-Ma_\gamma\sqrt{2m}}. \tag{4.71}$$

Here, the modified Marangoni number Ma_γ (table 3) quantifies the competition between interfacial area creation due to capillary forces and resistance to interfacial stretching due to Marangoni forces:

$$Ma_\gamma = \frac{E_0(\Gamma_0)}{\gamma(\Gamma_0)} = \frac{E_0}{\eta c}\times\frac{\eta c}{\gamma} = Ma\times Ca. \tag{4.72}$$

Reverse Marangoni flows immobilize the interface when $Ma_\gamma \gg 1$ or $E_0 \gg \gamma$, in which case the interface behaves like an incompressible sheet with

$$\beta_{\text{stiff}} = \text{Re}\left[\beta\left(Ma_\gamma \to \infty\right)\right] = -\frac{1}{2\sqrt{2}}\omega_0\sqrt{m} = -\frac{1}{2\sqrt{2}}\sqrt{\omega_0 \nu k^2}. \tag{4.73}$$

By contrast, weak E_0 gives $Ma_\gamma \ll 1$ and recovers the clean interface limit β_{clean} (4.67). The ratio of the damping coefficient in the two limits is

$$\frac{\beta_{\text{stiff}}}{\beta_{\text{clean}}} = \frac{1}{4\sqrt{2m}} = \frac{1}{8\sqrt{\pi}}\left(\frac{c\lambda}{\nu}\right)^{1/2}. \tag{4.74}$$

Because wave speeds are greater than $c_{\text{min}} \approx 0.2$m/s on water-air interfaces, $\beta_{\text{stiff}} > \beta_{\text{clean}}$ for waves with millimeter (or larger) wavelength. Typical capillary waves therefore decay more rapidly when surfactants are present.

Notably, the damping coefficient depends nonmonotonically on Ma_γ (figure 18), with a maximum value $\beta_{\text{max}} \approx 2\beta_{\text{stiff}}$ that occurs at an intermediate Marangoni number, as reported in both experiments and simulations (Davies & Vose 1965; Alpers & Hühnerfuss 1989). Lucassen (1968) ascribes this maximum to a resonance-like mechanism between transverse capillary waves and longitudinal Marangoni waves. Damping is maximum when the wavelengths of these transverse and longitudinal waves are equal.

Probstein (1994) notes that β_{stiff} can be estimated by treating the interface as an incompressible plate. The damping coefficient in general takes the form $\beta \sim -\nu k/d$, where d is viscous gradient length scale in the bulk. Without surfactants, the dissipation extends to a depth $d \sim k^{-1}$, and $\beta = \beta_{\text{clean}} \sim -\nu k^2$ in agreement with (4.67). When surfactants immobilize the surface via Marangoni flows, the viscous boundary layer under the surface is akin to that of an incompressible plate oscillating at frequency ω. This is Stokes' second problem, revealing a viscous boundary layer that extends to a depth $d \sim (\nu/\omega)^{1/2}$, with damping rate $\beta_{\text{stiff}} \sim -(\nu\omega)^{1/2}k$.

The enhanced damping mechanism is illustrated in figure 19. Fluid elements on and near a surfactant-free interface travel in circular trajectories. Surfactants drive Marangoni flows that act to immobilize the interface, distorting these circular trajectories. The change from near-vertical motion at the interface to circular trajectories in the subphase increases velocity gradients and viscous dissipation. Notably, damping still occurs due to bulk viscous dissipation: surface incompressibility due to reverse Marangoni flow modifies the bulk velocity field in a manner that amplifies viscous dissipation in the bulk (§3.3.2).

4.3.3. Damping due to soluble and/or surface viscous surfactants—

The surface flow generated by the motion of a wave creates alternating regions of dilatation and compression (figure 19). Any putative surface viscous stresses would resist such a deformation. Note also that surface shear and surface dilatational viscosities appear inseparably in the Boussinesq-Scriven equation (3.118) for 1D deformations, as occurs in plane waves. In other words, a monolayer with finite surface shear viscosity η_s resists one-

dimensional stretching and compression, even if the surface dilatational viscosity κ_s is negligible.

Recall from the oscillatory dynamics of surfactant-covered bubbles (4.2.2) that additional viscous stresses arise due to excess surface rheology as well as adsorption/desorption. The tangential stress balance (3.94) for a Newtonian monolayer undergoing 1D deformation is

$$\eta\left(\frac{\partial v_x}{\partial z}+\frac{\partial v_z}{\partial x}\right)=-\frac{E_0}{\Gamma_0}\frac{\partial \Gamma}{\partial x}+(\eta_s+\kappa_s)\frac{\partial^2 v_x}{\partial x^2}, \tag{4.75}$$

where changes in Γ now drive adsorption/desorption fluxes. In what follows, we will assume diffusion-limited adsorption (§3.2); kinetically-limited systems follow similar trends. Solving the bulk diffusion equation and substituting in (4.75) while assuming small perturbations as in (4.68) gives

$$\eta\left(\frac{\partial v_x}{\partial z}+\frac{\partial v_z}{\partial x}\right)=\frac{E_{\text{eff}}}{i\omega_0-\beta}\frac{\partial^2 v_x}{\partial x^2}, \tag{4.76}$$

which is similar to the insoluble tangential stress balance (4.70*b*) except with a *complex* effective modulus:

$$E_{\text{eff}}=E^*+(i\omega_0-\beta)(\eta_s+\kappa_s), \tag{4.77}$$

where $E^*(\omega)$ is the complex modulus for uniform oscillatory deformation (4.34).

The real part of the effective dilatational modulus E_{eff} (4.77) quantifies the strength of reverse Marangoni flows. Rapid adsorption eliminates Marangoni forces, giving $\text{Re}[E_{\text{eff}}]\approx 0$ (assuming $|\beta|\ll\omega_0$). By contrast, reverse Marangoni flows are strongest for negligibly slow adsorption, whereupon $\text{Re}[E_{\text{eff}}]\approx E_0$ (4.34). Solubility effectively reduces the dynamic Gibbs modulus $E=\text{Re}[E^*]$ (figure 16) and therefore decreases the damping rate $\beta(E)$. Indeed, Franklin *et al.* (1774) and Levich (1962) note that sailors report that waves are damped more with animal and vegetable oils (with insoluble fatty acids) than with soluble mineral oils. The imaginary part of E_{eff} (4.77) quantifies surface viscous resistance to wave motion. In addition to η_s and κ_s, $\text{Im}[E_{\text{eff}}]$ contains a contribution $\kappa_s^{\text{ads}}=\text{Im}[E^*]$ (4.34), which becomes significant when ω_0 is comparable to the sorption time.

The full calculation of β is complicated, and we do not pursue it here. However, the similarity between (4.76) and (4.70*b*) suggests that the damping rate β depends on the ratio of E_{eff} and γ. An effective immobilization parameter,

$$\Psi^*=\frac{E_{\text{eff}}}{\gamma}\approx Ma_\gamma\frac{\text{Re}[E^*]}{E_0}+iCa\left(Bq_\eta+Bq_\kappa+Ma\frac{\text{Im}[E^*]}{E_0}\right) \tag{4.78}$$

takes the place of $Ma_\gamma=E_0/\gamma$ in (4.71), since $\beta\ll\omega_0$, where Ma and Ma_γ are defined in table 3, and

$$Ca = \frac{\eta c}{\gamma}, \quad Bq_\eta = \frac{\eta_s k}{\eta}, \quad Bq_\kappa = \frac{\kappa_s k}{\eta}. \tag{4.79}$$

Equation (4.78) is the analog of (4.43) for the mechanical response of oscillating bubbles.

The damping rate is a nontrivial function of Ma_γ, Bq_η or Bq_κ in general, with limiting values of β_{clean} (4.67) when $|\Psi^*| \to 0$ and β_{stiff} (4.73) when $|\Psi^*| \to \infty$. The rate of damping therefore does not distinguish between the specific surfactant processes responsible for the damping. Measurements of a partially immobilized interface can at best be used to determine the lumped immobilization parameter Ψ^*.

4.4. Thin films: surfactant dynamics affect thickness of coating

Thin fluid films are central to engineering and biophysical flows, most of which involve surfactants. Every blink or breath involves the dynamics of a tear film or the alveolar fluid film, and every stroke of a paintbrush leaves a thin liquid film that eventually dries. Industrial machinery is often coated with thin films of lubricant, and fibers, parts and products are coated by thin liquid films that are flowed over the objects. As with §4.1–4.3, the effects of surface viscosity and Marangoni flows can not always be neatly differentiated in many of these applications. In this section, we will quantify surfactant-covered thin film flows and highlight how the observable quantity (e.g. film thickness) relates to one or many "hidden" surfactant variables.

4.4.1. Plate coating: the Landau-Levich-Derjaguin problem—

Dip coating is perhaps the easiest way to deposit a thin liquid film on an object: dip the object in a liquid reservoir, then pull it out. The thickness h of the entrained liquid layer depends on the velocity V of the substrate, and the density, viscosity and surface tension of the liquid being drawn out (figure 20) as given by the classic Landau-Levich-Derjaguin (LLD) law,

$$\frac{h_{\text{LLD}}}{\ell_c} \approx 0.946 Ca^{2/3}, \tag{4.80}$$

where

$$\ell_c = \sqrt{\frac{\gamma}{\rho g}} \tag{4.81}$$

is the capillary length (Landau & Levich 1942; Quéré 1999), and $Ca = \eta V/\gamma$ is the capillary number.

The LLD scaling follows from dividing the film into three regions: a film of uniform thickness coating the plate far above the reservoir, a static or undisturbed meniscus (figure 20*a*), and an intermediate *dynamic meniscus* of length ℓ_d that smoothly matches the interfacial curvature between the uniform coating and the static meniscus (figure 20*b*). Neglecting fluid inertia, the viscous stress in a dynamic meniscus of thickness h scales with $\eta V/h^2$, and balances the capillary stress, which is the gradient of the Laplace pressure (γ/ℓ_c) along the dynamic meniscus of length ℓ_d.

$$\frac{\eta V}{h^2} \sim \frac{\gamma}{\ell_c \ell_d}. \tag{4.82}$$

Near the liquid reservoir, the curvature of the dynamic meniscus must smoothly match to the static meniscus, which is set by the capillary length ℓ_c, giving

$$\frac{1}{\ell_c} \sim \frac{h}{\ell_d^2}. \tag{4.83}$$

Combining (4.82) and (4.83) to eliminate ℓ_d gives the $Ca^{2/3}$ scaling in the LLD law.

The fluid being drawn out of the bath is rarely pure in most applications, and it has long been known that surfactants enhance the thickness h_0 of the film. Reverse Marangoni stresses and possibly surface rheological stresses immobilize the interface, dragging excess liquid along with the surface. In the following sections, we will outline recent studies that adapt the LLD approach to accommodate various surfactant processes, which first requires a description of the fluid dynamics of the entrained film.

For simplicity, we assume that the balance between viscous and capillary stresses dominate the dynamic meniscus. In particular, both inertia and gravity are weak, such that $\rho V^2/h_0 \ll \eta V/h_0^2$ and $\rho g \ll \eta V/h_0^2$, where V is the withdrawal velocity and h_0 is the film thickness. Under these assumptions, fluid does not drain to leading order: the film asymptotes to a uniform upward flow far from the reservoir. For sufficiently thin films ($h_0 \ll \ell_c$), lubrication theory holds within the dynamic meniscus:

$$\eta \frac{\partial^2 u}{\partial x^2} = \frac{\partial p}{\partial z}, \quad \frac{\partial p}{\partial x} = 0. \tag{4.84}$$

Near the plate, the slope and curvature of the liquid surface $h(z)$ is small, and the Young-Laplace equation (2.6) gives the capillary pressure:

$$p_c \approx -\gamma \frac{\mathrm{d}^2 h}{\mathrm{d}z^2}. \tag{4.85}$$

However, $\partial p/\partial x = 0$ within the lubrication layer, and therefore bulk fluid pressure p is constant across the film, and equal to the local capillary pressure $p_c(z)$. Substituting $p(z) = p_c(z)$ in (4.84) and solving with boundary conditions $u(x = 0) = V$ and $u(x = h) = u_s$ gives

$$u(x, z) = -\frac{\gamma}{2\eta} \frac{\mathrm{d}^3 h}{\mathrm{d}z^3} \left(x^2 - xh\right) + (u_s - V) \frac{x}{h} + V. \tag{4.86}$$

Note that the surface velocity $u_s(z)$ and film thickness $h(z)$ are yet unknown.

Since gravitational drainage is negligible, $h(z)$ follows from mass conservation ($\int_0^h u \, \mathrm{d}x = V h_0$), to give

$$\frac{\gamma}{\eta}\frac{\partial^3 h}{\partial z^3} = \frac{12Vh_0}{h^3} - \frac{6V + 6u_s}{h^2}. \tag{4.87}$$

The surface velocity $u_s(z)$ is then determined by the interfacial stress condition. For a surfactant-free film, imposing $\eta\,\partial u/\partial x|_{x=h} = 0$ in (4.86) and substituting (4.87) gives

$$\frac{u_s}{V} = \frac{3}{2}\frac{h_0}{h} - \frac{1}{2}. \tag{4.88}$$

Notably, a stagnation point appears at $h(z) = 3h_0$, meaning that the surface velocity is directed along the plate motion for only a section of the dynamic meniscus. Surfactants modify this stagnation point, enabling more fluid to be drawn.

Substituting (4.88) in (4.87) gives the LLD equation

$$\frac{\gamma}{\eta}h''' = \frac{3V}{h^3}(h_0 - h), \tag{4.89}$$

where primes represent derivatives in z. In dimensionless variables, (4.89) becomes

$$\tilde{h}^3\tilde{h}''' = 1 - \tilde{h}, \tag{4.90}$$

where $\tilde{h} = h/h_0$ and $\tilde{z} = z/\ell_d$, and the dynamic meniscus length is

$$\ell_d = \frac{h_0}{(3Ca)^{1/3}}. \tag{4.91}$$

Far from the reservoir, $\tilde{h}(\infty) \to 1$, $\tilde{h}'(\infty) \to 0$, and $\tilde{h}''(\infty) \to 0$.

Landau & Levich (1942) realized that $\tilde{h}''$ must asymptotically match the curvature of the static meniscus near the reservoir. Using the Young-Laplace law and assuming zero contact angle, the static meniscus has height $\sqrt{2}\ell_c$ and curvature $\sqrt{2}/\ell_c$. In dimensionless terms, this inner boundary condition on (4.90) becomes

$$\tilde{h}'' = \frac{\sqrt{2}h_0}{\ell_c}\left(\frac{\gamma}{3\eta V}\right)^{2/3} \approx 0.64, \tag{4.92}$$

where the constant is found by numerically integrating (4.90). Rearranging (4.92) for the residual thickness h_0 then gives the classic LLD law (4.80).

In anticipation of the immobilizing effect of surfactants, we calculate the extreme case of complete surface immobilization. An incompressible surface has $u_s = V$, and (4.87) becomes

$$\frac{\gamma}{\eta}h''' = \frac{12V}{h^3}(h_0 - h), \tag{4.93}$$

Comparing (4.93) with (4.89) reveals this limit to be identical to the standard LLD problem, but with a modified dynamic meniscus length

$$\ell_d^{\text{immob}} = \frac{h_0}{(12Ca)^{1/3}}. \tag{4.94}$$

In other words, the dimensionless problem and the matching proceeds exactly like for LLD, but with a capillary number that four times larger, thereby modifying this LLD scaling to

$$\frac{h_0^{\text{immob}}}{\ell_c} \approx 0.946(4Ca)^{2/3} = 4^{2/3}\frac{h_{\text{LLD}}}{\ell_c}. \tag{4.95}$$

An incompressible interface entrains more fluid as the plate is withdrawn, increasing the film thickness up to $4^{2/3}$ more than a fully mobile interface (figure 21). In what follows, we will treat specific surfactant processes based on illustrative works in dip coating (Park 1991; Quéré 1999; Shen *et al.* 2002; Scheid *et al.* 2010), each of which reveals a similar transition between the clean and immobilized limits.

4.4.2. Insoluble and surface-inviscid surfactant—Surfactants give rise to Marangoni and surface viscous forces that resist interfacial stretching. The Boussinesq-Scriven equation (3.94) modifies the interfacial stress balance to

$$\frac{\partial \gamma}{\partial z} + (\eta_s + \kappa_s)\frac{\partial^2 u_s}{\partial z^2} = \eta \frac{\partial u}{\partial x}\bigg|_{x=h} = \eta\left(-\frac{6Vh_0}{h^2} + \frac{2V + 4u_s}{h}\right), \tag{4.96}$$

where $u(x, z)$ follows from (4.86) and (4.87). We will first consider insoluble surfactants that are surface inviscid, so that $\eta_s = \kappa_s = 0$. Surface fluid flows establish gradients in Γ, which exert reverse Marangoni stresses. Without surfactant exchange, surface diffusion is the only mechanism to relax gradients in $\gamma(\Gamma)$. Perturbing the surface concentration via $\Gamma(z) = \Gamma_0 + \delta\Gamma(z)$, the steady-state surface conservation equation (3.10) becomes

$$\Gamma_0 \frac{\partial u_s}{\partial z} = D_s \frac{\partial^2(\delta\Gamma)}{\partial z^2}. \tag{4.97}$$

Integrating (4.97) and imposing $\partial\Gamma/\partial z(z \to \infty) \to 0$ and $u_s(z \to \infty) \to V$ gives

$$\frac{\partial(\delta\Gamma)}{\partial z} = \frac{\Gamma_0}{D_s}(u_s - V). \tag{4.98}$$

The Marangoni stress is then given by

$$\frac{\partial \gamma}{\partial z} = -\frac{E_0}{\Gamma_0}\frac{\partial \delta\Gamma}{\partial z} = -\frac{E_0}{D_s}(u_s - V). \tag{4.99}$$

Substituting into the interfacial stress balance (4.96) with $\eta_s = \kappa_s = 0$ and nondimensionalizing gives

$$Ma_D(1-\tilde{u}_s) = -\frac{6}{\tilde{h}^2}+\frac{2+4\tilde{u}_s}{\tilde{h}}, \tag{4.100}$$

where the surface diffusive Marangoni number (table 3) is:

$$Ma_D = \frac{E_0 h_0}{D_s \eta} = \frac{E_0}{\eta V}\times\frac{V h_0}{D_s} = Ma \times Pe_s\,. \tag{4.101}$$

When $Ma_D \gg 1$, the interface is immobilized relative to the moving plate, and (4.100) gives $\tilde{u}_s \to 1$, or $u_s \to V$. This surface immobilization occurs when the Marangoni modulus is large or surface diffusivity is weak. By contrast, weak Marangoni flows or strong surface diffusion ($Ma_D \ll 1$) recovers the u_s corresponding to clean surfaces (4.88).

The film thickness equation (4.87) for an inviscid, insoluble surfactant, using (4.100) for u_s, is

$$\tilde{h}^3\tilde{h}''' = (1-\tilde{h})\left(1+\frac{3\tilde{h}Ma_D}{4+\tilde{h}Ma_D}\right). \tag{4.102}$$

As $Ma_D \to 0$, (4.102) is identical to the classic LLD equation for a clean interface (4.90). For strong immoblization as $Ma_D \to \infty$, the right-hand side increases four-fold, amplifying the apparent capillary number four-fold, and increasing the film thickness by $4^{2/3}$ (Park 1991; Quéré 1999).

4.4.3. Soluble and/or surface viscous surfactant—Adsorption/desorption weakens the Marangoni effect, and reduces the thickening factor $\alpha = h/h_{\mathrm{LLD}}$ (Ou Ramdane & Quéré 1997). However, as with oscillating bubbles (§4.2.2) and wave damping (§4.3), the distinct effects of adsorption/desorption and intrinsic surface viscosities are not easy to tease apart. The role of surface viscosity in dip coating has only recently gained attention (Scheid *et al.* 2010; Delacotte *et al.* 2012; Seiwert *et al.* 2014) in systems with negligible Marangoni forces; e.g. when rapid adsorption/desorption eliminates surface tension gradients.

Assuming surface diffusion to be negligible, gradients in $\gamma(\Gamma)$ are governed by the balance of flow and adsorption (§3.2):

$$\Gamma_0\frac{\partial u_s}{\partial z} = -\frac{\delta\Gamma}{\tau_s}\,. \tag{4.103}$$

Taking perturbations $\delta\Gamma$ from equilibrium Γ_0 to be small gives a Marangoni stress

$$\frac{\partial\gamma}{\partial z} = -\frac{E_0}{\Gamma_0}\frac{\partial(\delta\Gamma)}{\partial z} = E_0\tau_s\frac{\partial^2 u_s}{\partial z^2}\,. \tag{4.104}$$

Substituting (4.103) in the interfacial stress condition (4.96) gives

$$\left(\frac{E_0\tau_s + \eta_s + \kappa_s}{\eta}\right)\frac{\partial^2 u_s}{\partial z^2} = -\frac{6Vh_0}{h^2} + \frac{2V + 4u_s}{h}. \tag{4.105}$$

Nondimensionalizing over h_0, V and $\ell_d = (3Ca)^{-1/3}h_0$ for $h(z)$, $u_s(z)$ and z gives

$$\tilde{\Psi}\frac{\partial^2 \tilde{u}_s}{\partial z^2} = -\frac{6}{\tilde{h}^2} + \frac{2 + 4\tilde{u}_s}{\tilde{h}}, \tag{4.106}$$

where

$$\tilde{\Psi} = \frac{(3Ca)^{2/3}\Psi\ell_c}{h_0}, \tag{4.107}$$

and Ψ is the surface immobilization parameter, described in §3.4.3:

$$\Psi = \frac{E_0\tau_s + \eta_s + \kappa_s}{\eta\ell_c} = Ma_K + Bq_\eta + Bq_\kappa. \tag{4.108}$$

If E_0, τ_s, η_s, and κ_s are known separately, (4.106) can be solved numerically along with the film thickness equation (4.87) for arbitrary values of Ψ (Scheid *et al.* 2010). The limits of large and small Ψ are easy to interpret: the surface is fully mobile as $\Psi \to 0$, recovering the classic LLD solution. By contrast, the interface is immobilized as $\Psi \to \infty$, in which case $u_s \approx V$ everywhere. The same factor of 4 found in the $Ma_D \to \infty$ limit of (4.102) appears in the LLD equation, and the film thickness increases by $4^{2/3}$.

Measured film thickness depends on the lumped parameter Ψ and does not distinguish between three distinct phenomena – surface shear viscosity, surface dilatational viscosity, and apparent dilational viscosity due to adsorption/desorption (§3.4.3). More information, e.g. from complementary experiments, would be required to deconvolve the impact of each.

It may also be possible to suppress one surfactant process to isolate the effect of another in specific systems. For example, intrinsic surface viscosity becomes the dominant immobilizing component when $Bq \gtrsim Ma_K$. The Marangoni contribution to immobilization is weakest when adsorption/desorption is fast: gradients in Γ are small if $\tau_s \ll \tau_{\text{flow}}$, so that

$$Ma_K = \frac{E_0}{\eta V} \times \frac{V\tau_s}{\ell_c} = Ma \times \frac{\tau_s}{\tau_{\text{flow}}} \ll 1. \tag{4.109}$$

This condition, however, does not account for finite subphase depth and the availability of surfactant molecules in the thin film. Effective surfactant exchange requires the film to be thicker than the depletion depth $L_d = \partial\Gamma/\partial C_s$ (§3.2), so as to not be 'confined' (Quéré 1999; Delacotte *et al.* 2012) by the lack of sufficient dissolved molecules. Suppressing Marangoni flows therefore requires large surfactant concentrations (so L_d is small), large withdrawing velocities (so h_0 is large), and eliminating energetic barriers to adsorption (so τ_s is small). Following this strategy, Delacotte *et al.* (2012) measured enhanced film thickness in unconfined films despite rapid adsorption, suggesting that surface viscosity does indeed play

a role in immobilizing interfaces. However, the two surface viscosities η_s and κ_s still remain indistinguishable in 1D surface deformations.

Finally, the presence of micelles at high bulk surfactant concentrations influences thickness of the coating in nontrivial ways. Above the critical micelle concentration (CMC), micelles dissociate to maintain a reservoir of free monomers, thereby eliminating diffusion limitation to adsorption. Bulk concentrations above the CMC thus lead to a thinner coating, as Marangoni flows are suppressed and the interface is 'remobilized' (Stebe & Maldarelli 1994, see also §4.1.2). However, micelles may dissociate at timescales comparable to or slower than the bulk diffusion time at very high concentrations, thereby depleting the bulk of free monomers and enhancing the Marangoni effect, which again leads to a thicker entrained film (Shen *et al.* 2002).

4.4.4. Thin film drainage—Gravitational drainage is negligible in the LLD problem, and fluid flow is driven entirely by capillary pressure. For illustration and completion, we will briefly examine one case where gravity drives thin film flow. Approximating the flow in a thin film draining down a vertical wall using lubrication theory, the velocity $u(x, z, t)$ obeys

$$\eta \frac{\partial^2 u}{\partial x^2} = -\rho g, \tag{4.110}$$

where z is positive downward, and x is perpendicular to gravity. Solving with a no-slip wall at $x = 0$ and a (yet unknown) surface velocity $u_s(z, t)$, the fluid velocity is

$$u(x, z, t) = -\frac{\rho g}{2\eta}\left(x^2 - hx\right) + \frac{x u_s}{h}. \tag{4.111}$$

Conservation of mass requires

$$\frac{\partial h}{\partial t} + \frac{\partial Q}{\partial z} = 0, \tag{4.112}$$

Where $Q(z, t) = \int_0^h u(x, z, t)\,\mathrm{d}x$ is the vertical flux. Substituting (4.111) in (4.112) gives the film thickness equation:

$$h_t + \frac{\rho g}{4\eta} h^2 h' + \frac{(h u_s)'}{2} = 0, \tag{4.113}$$

where primes represent z derivatives, and the subscript t denotes time derivatives.

A clean fluid interface is stress-free, and enforcing this at $x = h$ in (4.111) gives

$$u_s = \frac{\rho g h^2}{2\eta}. \tag{4.114}$$

Substituting (4.114) in (4.113) gives the evolution equation for a clean fluid film draining under gravity,

$$h_t + \frac{\rho g}{\eta} h^2 h' = 0. \tag{4.115}$$

By contrast, surfactant processes resist interfacial deformation, which modifies u_s. Rather than explicitly treating surface rheology and transport, we will consider the extreme case when the surface is immobilized due to some combination of reverse Marangoni flow and surface viscous resistance. Setting $u_s = 0$ in (4.113) gives

$$h_t + \frac{\rho g}{4\eta} h^2 h' = 0. \tag{4.116}$$

Notably, the same factor of 4 between the stress-free interface and the immobile interface appears here, as in the LLD problems (4.95).

To solve the appropriate film equation, we use R as a system-specific lengthscale (such as length of the plate) in the flow direction. Nondimensionalizing over R, h_0, and $\eta R/\left(\rho g h_0^2\right)$ for z, h and t, respectively, gives

$$\tilde{h}_t + \frac{1}{\beta} \tilde{h}^2 \tilde{h}' = 0, \tag{4.117}$$

where $\beta = 1$ for a clean surface (4.115) and $\beta = 4$ for an immobile surface (4.116). The film thickness obeys a similarity solution, $h = F(\zeta)$, where $\zeta = \sqrt{\tilde{z}/\tilde{t}}$, and F obeys

$$F' F^2 - \beta \zeta^2 F' = 0 \tag{4.118}$$

with solution $F(\zeta) = \sqrt{\beta}\zeta$. The dimensional film thickness is then

$$h(z,t) = \sqrt{\frac{\beta \eta z}{\rho g t}}. \tag{4.119}$$

The clean interface limit ($\beta = 1$) recovers the classic Jeffreys' solution (Jeffreys 1930). More generally, the $h \sim t^{-1/2}$ scaling persists even with surfactant. Drainage takes longer with surfactant, however, and the film is $\beta^{1/2}$ or twice as thick when the surface is completely immobile. Surface viscosity, Marangoni flows or some nontrivial combination acts to retard surface flow, thereby slowing film drainage. This effect is responsible in part for the long lives of soapy bubbles and foams (§4.5), and the increased coalescence time of surfactant-covered bubbles.

Bhamla *et al.* (2014) developed an experimental platfrom that mimics drainage dynamics of tear films. A hemispherical dome is raised from a reservoir of liquid containing a particular surfactant, and the drainage is measured. Insoluble (DPPC) monolayers do indeed retard drainage. Measurements and numerical simulations captured the transition between the expected Reynolds' thinning law for clean fluids (4.115) and drainage with a surface-immobilized surface (4.116) (Bhamla *et al.* 2014). Working with the same system, Hermans *et al.* (2015) later identified that Marangoni effects and dilatational viscosity cannot be

deconvoluted in this process. In other words, the surface is immobilized as a function of $\Psi \approx Bq + Ma$. Surface immobilization is controlled not by Ma or Bq_η or Bq_κ alone, but by a combination of the three that is not easy to separate except in specific geometries, or with independent measurements of surfactant properties.

4.5. Foams: surfactant properties impact macroscopic flows

Foams are examples of complex multiphase materials, with ubiquitous applications in the kitchen (e.g. whipped cream), in cleaning (e.g. soap suds), in packaging (e.g. Styrofoam), and superlight construction materials (e.g. metal foams). Most relevant to our discussion are aqueous foams, which are stabilized against rupture by adsorbed surfactant molecules. The type and rheology of the surfactant influences its stability and its macroscopic flow (Buzza *et al.* 1995; Cohen-Addad *et al.* 2013). Here we focus on foam drainage, the gravity-driven flow of liquid within an aqueous foam.

The geometry of soap foams is intricate, but can be described by few basic rules of energy minimization, as first laid out by the Belgian scientist Joseph Plateau in the 19th century (at a time when he was already blind). The liquid content in a foam resides mostly in a network of *channels* ('Plateau borders') connected to each other at *nodes*, where four channels meet in a tetrahedral configuration (figure 22). The principal geometric parameters are the typical length L of a channel, and the transverse radius of curvature r, which is also the characteristic channel width. The volume of fluid in each channel is $O(r^2L)$, whereas each node contains a volume $O(r^3)$. The macroscopic foam occupies a volume of $O(L^2)$, so that the volume fraction of the liquid phase is

$$\epsilon = \delta_\epsilon \left(\frac{r}{L}\right)^2 + \delta'_\epsilon \left(\frac{r}{L}\right)^3, \tag{4.120}$$

where δ_ϵ and δ'_ϵ are constants. When $\epsilon \ll 1$, the foam is said to be 'dry', and then $r \approx \delta_\epsilon^{-1/2} L \epsilon^{1/2}$.

Surfactants modify fluid flow within these channels and nodes, systematically altering macroscopic foam drainage. In what follows, we will review and illustrate past works (Verbist *et al.* 1996; Koehler *et al.* 2000; Durand & Langevin 2002) first using a surfactant transport model that accounts for flow within channels and nodes, and then using a macroscopic model that lumps all surfactant processes into course-grained coefficients. Together, the two models paint a qualitative picture of how surfactant processes impact measurable macroscopic foam properties.

4.5.1. Physicochemical model—We simplify the geometry by considering only a planar projection of a vertical liquid channel (figure 22) of width $2h(z)$. The non-trivial shape of the channel and its orientation relative to gravity will modify the following analysis, but only by numerical prefactors (Koehler *et al.* 2000; Durand & Langevin 2002). Like with coating flows, we exploit the fact that $r \ll L$, and use lubrication theory for the bulk fluid flow:

$$\eta \frac{\partial^2 u}{\partial x^2} = \frac{\partial P}{\partial z}, \tag{4.121}$$

where $P(z) = p(z) - \rho g z$. Integrating (4.121) and imposing boundary conditions $u(x = \pm h) = u_s$ gives

$$u(x, z) = \frac{x^2 - h^2}{2\eta} \frac{\partial P}{\partial z} + u_s, \tag{4.122}$$

where the surface velocity u_s is yet unknown and will be determined by the surface stress balance. The fluid pressure, p, relative to the gas pressure in the bubbles obeys the Young-Laplace equation, giving

$$\frac{\partial P}{\partial z} \approx \frac{\gamma}{h^2} \frac{\partial h}{\partial z} - \rho g, \tag{4.123}$$

where the total curvature is assumed to be $1/h(z)$.

Conservation of mass within the channel requires

$$\frac{\partial h}{\partial t} + \frac{\partial}{\partial z} \left[\int_{-h}^{h} u(x, z) \mathrm{d}x \right] = 0, \tag{4.124}$$

and substituting $u(x,z)$ from (4.122) gives the drainage equation for each channel

$$\frac{\partial h}{\partial t} + \frac{\partial}{\partial z} \left[-\frac{h^3}{3\eta} \frac{\partial P}{\partial z} + 2 u_s h \right] = 0. \tag{4.125}$$

The surface velocity u_s in (4.125) is dictated by the interfacial stress balance (3.94):

$$-\frac{E_0}{\Gamma_0} \frac{\partial \Gamma}{\partial z} + (\eta_s + \kappa_s) \frac{\partial^2 u_s}{\partial z^2} = h \frac{\partial P}{\partial z}. \tag{4.126}$$

Reverse Marangoni stresses are driven by gradients in Γ, as described by the balance between surface convection and diffusion, or adsorption/desorption, as pursued in previous sections.

We will choose one illustrative case that is analytically tractable. If the surfactant is surface inviscid ($\eta_s = 0,\ \kappa_s = 0$) and insoluble ($\tau_s^{-1} = 0$), gradients in Γ can only relax via surface diffusion. Durand & Langevin (2002) solved the surfactant conservation equation for Γ, using (4.126) to obtain

$$u_s = -\frac{D_s}{E_0} h \frac{\partial P}{\partial z}, \tag{4.127}$$

which when substituted in (4.125) along with (4.123) gives the drainage equation

$$\frac{\partial h}{\partial t} + \frac{\partial}{\partial z}\left[\frac{1}{3\eta}\left(\rho g h^3 - \gamma h \frac{\partial h}{\partial z}\right) + \frac{2D_s}{E}\left(\rho g h^2 - \gamma \frac{\partial h}{\partial z}\right)\right] = 0. \tag{4.128}$$

Analogous drainage equations can be derived for more general 3D networks and written in terms of the cross-sectional area $A \propto h^2$ of the channel. A measureable quantity is the volume fraction $\epsilon(z, t)$ of liquid in the foam, which relates to the channel cross-sectional area $A(z, t)$ via $\epsilon \sim (AL)/L^3$. A generalized 3D foam drainage equation emerges,

$$\frac{\partial \epsilon}{\partial t} + \frac{\partial}{\partial z}\left[\delta_1 \frac{L^2}{\eta}\left(\rho g \epsilon^2 - \delta_0 \frac{\gamma}{L}\frac{\partial \epsilon^{3/2}}{\partial z}\right) + \delta_2 \frac{D_s L}{E_0}\left(\rho g \epsilon^{3/2} - \delta_0 \frac{\gamma}{L}\frac{\partial \epsilon}{\partial z}\right)\right] = 0, \tag{4.129}$$

where δ_0, δ_1, and δ_2 are numerical constants that depend on the particular geometry of the Plateau borders (Koehler *et al.* 2000; Durand & Langevin 2002). Nondimensionalizing length and time in (4.129) over $\delta_0\gamma/\rho g L$ and $\delta_0\gamma\eta/\delta_1\rho^2 g^2 L^3$ gives

$$\frac{\partial \epsilon}{\partial \tilde{t}} + \frac{\partial}{\partial \tilde{z}}\left[\epsilon^2 - \frac{\partial \epsilon^{3/2}}{\partial \tilde{z}} + \frac{\delta_2}{\delta_1 Ma_D}\left(\epsilon^{3/2} - \frac{\partial \epsilon}{\partial \tilde{z}}\right)\right] = 0, \tag{4.130}$$

where the surface diffusive Marangoni number is $Ma_D = E_0 L/\eta D_s$, as in table 3.

Marangoni reverse flows are strongest when surface diffusion is weak, and $Ma_D \gg 1$, in which case (4.130) becomes

$$\frac{\partial \epsilon}{\partial \tilde{t}} + \frac{\partial \epsilon^2}{\partial \tilde{z}} - \frac{\partial^2 \epsilon^{3/2}}{\partial \tilde{z}^2} = 0. \tag{4.131}$$

In this rigid-interface limit, the channels are essentially no-slip walls, and bulk fluid flow within the channels is Poiseuille-like. This model was was first given by Verbist *et al.* (1996), who derived it from a macroscopic perspective as we illustrate in the next section. The dominant resistance to foam drainage in the rigid-interface limit arises from bulk viscous dissipation.

By contrast, strong surface diffusion quickly eliminates surface concentration gradients when $Ma_D \ll 1$, thereby weakening Marangoni reverse flows. Rescaling the characteristic time in (4.130) by $\delta_1 Ma_D/\delta_2$ in this limit gives

$$\frac{\partial \epsilon}{\partial \tilde{t}} + \frac{\partial \epsilon^{3/2}}{\partial \tilde{z}} - \frac{\partial^2 \epsilon}{\partial \tilde{z}^2} = 0. \tag{4.132}$$

This mobile-interface drainage equation represents channels with plug-like bulk flow: the surface is completely stress-free or ‘remobilized’ in this limit. The resistance to fluid flow arises from dissipation at the channel surfaces. In the following sections, we will explore the measurable macroscopic signatures of these two limits.

4.5.2. Macroscopic model—The analysis thus far ignored the nodes that connect Plateau borders within the foam network. Mixing, merging and bending of streamlines at

nodes occur over length scales $r \ll L$, and therefore increase viscous dissipation. The detailed flow in the nodes (Cohen-Addad *et al.* 2013) is beyond the scope of our discussion, and we will instead outline a course-grained model (Koehler *et al.* 2000) that treats the foam as a porous macroscopic material.

Mass conservation in the foam network requires

$$\frac{\partial \epsilon}{\partial t} + \frac{\partial (\epsilon v)}{\partial z} = 0, \tag{4.133}$$

where the mean velocity v obeys Darcy's law:

$$\frac{\partial P}{\partial z} + \frac{\eta v}{k(\epsilon)} = 0. \tag{4.134}$$

All details of the network and dissipation within the foam are lumped into a permeability $k(\epsilon)$ in (4.134). The foam is driven by both capillary and hydrostatic pressures:

$$P(z) = p_{\text{gas}} - \frac{\gamma}{r} - \rho g z \approx p_{\text{gas}} - \frac{\gamma \delta_\epsilon^{1/2}}{L \epsilon^{1/2}} - \rho g z, \tag{4.135}$$

where the radius of curvature is assumed to be small ($r \ll L$), and the foam is assumed to be dry ($\epsilon \ll 1$) so that $r \approx \delta_\epsilon^{-1/2} L \epsilon^{1/2}$ from (4.120). Using (4.135) in (4.134) gives

$$\rho g + \frac{\gamma \delta_\epsilon^{1/2}}{L} \frac{\partial \epsilon^{-1/2}}{\partial z} = \frac{\eta v}{k(\epsilon)}, \tag{4.136}$$

which can be solved for v in terms of the permeability $k(\epsilon)$. Mass conservation (4.133) then becomes

$$\frac{\partial \epsilon}{\partial t} + \frac{\partial}{\partial z}\left[\frac{\rho g}{\eta} k(\epsilon)\epsilon - \frac{\gamma \delta_\epsilon^{1/2}}{\eta L} k(\epsilon) \frac{\partial \epsilon^{1/2}}{\partial z}\right] = 0, \tag{4.137}$$

which is the generalized macroscopic foam drainage model.

The permeability $k(\epsilon)$, in general, depends on the geometry and boundary conditions for the flow within the foam network (Koehler *et al.* 2000). When Marangoni and/or surface viscous effects immobilize the interface, bulk flow within the channels is Poiseuille-like. The permeability $k(\epsilon)$ then comes from balancing the fluid pressure gradient $\eta V/r^2$ with that driving the Darcy flow $\eta V/k(\epsilon)$, implying

$$k(\epsilon) \propto r^2 \propto L^2 \epsilon\,. \tag{4.138}$$

Using $k(\epsilon) \sim L^2 \epsilon$ in (4.137) gives the (dimensional) rigid-interface drainage equation, (4.131).

By contrast, if surface stresses are negligible and interfaces are mobile, flow in the channels is plug-like. The dominant viscous resistance then comes from the merging flows at nodes,

which occupy a fraction of $O(r/L)$ of the total fluid volume. When the resistance to Darcy flow, $\eta V/k(\epsilon)$, arises from the volume-averaged viscous resistance at nodes, $(\eta V/r^2)(r/L)$, the foam permeability becomes

$$k(\epsilon) \propto rL \propto L^2\epsilon^{1/2}. \tag{4.139}$$

Substituting $k(\epsilon) \sim L^2\epsilon^{1/2}$ in (4.137) gives the node-dominated foam drainage equation (Koehler *et al.* 2000), which is identical to the mobile-interface drainage equation (4.132). However, the resistance to fluid drainage in this limit arises due to bulk viscous dissipation at the nodes, rather than surface stresses. In other words, flow in channels can be plug-like even when channel-dominated if the driving pressure gradient balances surface stresses via (4.126).

More generally, we expect surfactant processes to impact flow in foams via a lumped immobilization parameter

$$\Psi = \frac{E_0\tau + \eta_s + \kappa_s}{\eta L}, \tag{4.140}$$

where τ is the timescale of the dominant surfactant process that relaxes Marangoni stresses. If the channel walls are not immobilized, the surface 'slips' as the foam drains. Surface stresses associated with such a deformation scale like $(E_0\tau + \eta_s + \kappa_s)V/L^2$, which translates to a force per unit volume of the fluid of $(E_0\tau + \eta_s + \kappa_s)V/rL^2$. Equating this force to the macroscopic driving force density $\eta V/k(\epsilon)$ gives permeability

$$k(\epsilon, \Psi) \propto \frac{\eta L^2 r}{E\tau + \eta_s + \kappa_s} \propto \frac{L^2\epsilon^{1/2}}{\Psi}. \tag{4.141}$$

The permeability of channels increases with decreasing degree of immoblization: a 'slip-pier' interface makes flow more plug-like. Substituting $k(\epsilon) \sim L^2\epsilon^{1/2}/\Psi$ in (4.137) and setting $\Psi = Ma_D$ gives the dimensional analog of the mobile-interface drainage equation (4.132).

4.5.3. Foam drainage: predictions vs observations—Forced foam drainage experiments introduce fluid from the top at flow rate Q into a dry foam, and track the velocity v of a wet front as it moves downwards through the foam. The front moves at a velocity

$$v \propto Q^{\alpha}, \tag{4.142}$$

where the exponent α is typically between 1/3 and 1/2 (Verbist *et al.* 1996; Koehler *et al.* 2000; Durand & Langevin 2002). Surfactant processes impact this exponent in a measurable way.

The drainage equation in both channel- and node-dominated limits can be solved by modeling the wetted front as a soliton wave

$$\epsilon(z,t) = f(s) = f(z - vt) \tag{4.143}$$

which travels downward at a constant front velocity v. The foam is assumed to be dry far ahead of the moving front, and uniformly wetted far behind the front:

$$f(s \to \infty) = 0, \quad \text{and} \quad f'(s \to -\infty) = 0. \tag{4.144}$$

Verbist *et al.* (1996) and Koehler *et al.* (2000) describe this solution in detail for (4.131) and (4.132), respectively. Fortunately, the exponent α can be deduced without solving for the front profile. In the channel-dominated or rigid-interface limit, transforming (4.131) using $s = z - vt$, and integrating once gives

$$-vf + f^2 - \left(f^{3/2}\right)' = 0. \tag{4.145}$$

the $s \to -\infty$ condition (4.144) in (4.145) then gives

$$f(s \to -\infty) = \epsilon(z \to -\infty) \to v\,. \tag{4.146}$$

For a foam of cross-section area A, a macroscopic volume $vA\Delta t$ is wetted behind the moving front by a volume $Q\Delta t$ of fluid supplied at the top. The wetted volume fraction is then

$$\epsilon = \frac{Q}{vA}\,. \tag{4.147}$$

For the wetted region far behind the front, (4.146) gives

$$\frac{Q}{vA} \to v \quad \Rightarrow \quad v \propto Q^{1/2}, \quad \text{i.e.,} \quad \alpha = 1/2. \tag{4.148}$$

This scaling would be expected in a foam drainage experiment when the channel surfaces are immobilized, and the foam is essentially a network of connected tubes with Poiseuille flow through each channel.

By contrast, transforming and integrating (4.132) for the mobile-interface or node-dominated regime gives

$$-vf + f^{3/2} - f' = 0. \tag{4.149}$$

The boundary condition as $s \to -\infty$ (4.144) gives

$$f(s \to -\infty) = \epsilon(z \to -\infty) \to v^2\,. \tag{4.150}$$

Then, in the wetted region far behind the moving front,

$$\epsilon = \frac{Q}{vA} \to v^2 \quad \Rightarrow \quad v \propto Q^{1/3}, \ \text{i.e.,} \ \alpha = 1/3. \tag{4.151}$$

The transition from Poiseuille-like flow in immobilized channels to plug-like flow in mobile channels manifests as a change in the exponent α in (4.142) from 1/2 to 1/3.

Surfactants change the character of drainage based on the extent of surface immobilization. Durand *et al.* (1999) measured the exponent α to transition between the two types of flow upon modifying surface rheology. The foam literature historically quantifies this transition in terms of the 'Kraynik criterion' (Koehler *et al.* 2000; Durand & Langevin 2002) based on the surface shear viscosity:

$$M_K = \frac{r\eta}{\eta_s} = \frac{1}{Bq}. \tag{4.152}$$

Large M_K (or small Bq) corresponds to mobile channel surfaces, and small M_K (or large Bq) justifies the assumption of rigid channel walls.

However, η_s, κ_s, and $E_0\tau_s$ play indistinguishable roles in 1D compression/dilatation of interfaces, as noted in §3.4.3. What was previously attributed to dissipation due to a surface shear viscosity might arise from an intrinsic surface dilatational viscosity, or due to Marangoni stresses with finite-time adsorption/desorption, or some combination (Buzza *et al.* 1995). More generally, therefore, the transition from one drainage regime to the other should depend on the degree of immobilization Ψ. When $\Psi \gg 1$, the surface is immobilized, flow within the channels is Poiseuille-like, and the drainage exponent α is closer to 1/2. By contrast, channel surfaces are mobile when $\Psi \ll 1$, flow within the Plateau borders are plug-like, and $\alpha \approx 1/3$.

4.6. Particles and probes on surfactant-laden interfaces

Early descriptions of particle motion within viscous interfaces were motivated by the dynamics of membrane-bound proteins. Saffman & Delbrück (1975) approximated the phospholipid membrane as a thin fluid layer of thickness h and 3D viscosity η_m atop a subphase of viscosity η (figure 12). A modern interpretation of this system would introduce a surface shear viscosity $\eta_s = \eta_m h$. Saffman (1976) solved this problem asymptotically in the interface-dominated ($Bq \gg 1$) limit. The leading-order 2D problem has no steady solution for the translation of a cylinder – the well-known Stokes paradox. This far-field singularity must be regularized by some additional force – Saffman & Delbrück (1975) examined fluid inertia, finite system size, and viscous coupling with subphase liquid. Saffman (1976), and later Hughes *et al.* (1981), showed that subphase viscous resistance resolves the paradox in many practical systems. In addition to predicting membrane protein diffusivity, these relations help deduce surface rheology from the measured mobility of surface-attached probes (Prasad *et al.* 2006; Fuller & Vermant 2012; Zell *et al.* 2014), and form the basis for interfacial microrheology.

4.6.1. Translation and rotation of cylinders—A surface-attached particle translating within an insoluble surfactant monolayer disturbs the surface concentration distribution, potentially setting up reverse Marangoni flows. Assuming weak surfactant diffusivity ($Ma_D \gg 1$, table 3), these reverse flows modify the fluid streamlines to that of a surface incompressible flow (§3.3.2). Using the Green's function derived in §3.4.2, the surface

velocity field around a moving particle embedded within the monolayer can be written as a boundary integral,

$$\boldsymbol{u}_s(\boldsymbol{r}) = \int_S \boldsymbol{G}(\boldsymbol{r}-\boldsymbol{r}')\cdot\boldsymbol{f}(\boldsymbol{r}')\mathrm{d}S, \tag{4.153}$$

where S is the area occupied by the particle, and $\boldsymbol{r}' \in S$. The force density $\boldsymbol{f}(\boldsymbol{r}')$ is chosen such that $\boldsymbol{u}_s$ satisfies the boundary conditions at the probe surfaces (Fischer 2004*b*). The drag force on the particle is then

$$\boldsymbol{F}_{\mathrm{drag}} = \int_S \boldsymbol{f}(\boldsymbol{r})\mathrm{d}S\,. \tag{4.154}$$

Alternatively, flow fields can be obtained directly when the system geometry simplifies the Boussinesq-Scriven equations. For example, both the surface velocity $\boldsymbol{u}_s$ and bulk velocity $\boldsymbol{u}$ can be obtained directly for a cylindrical probe (Hughes *et al.* 1981; Barentin *et al.* 1999) by projecting the governing equations into Fourier-Bessel functions. Then, the drag force can be written as the sum of viscous contributions from the subphase and the monolayer:

$$\boldsymbol{F}_{\mathrm{drag}} = \int_S \hat{\boldsymbol{e}}_z\cdot\boldsymbol{\sigma}\mathrm{d}S + \int_{\partial S}\hat{\boldsymbol{e}}_r\cdot\boldsymbol{\sigma}_s\mathrm{d}\ell\,. \tag{4.155}$$

where $\boldsymbol{\sigma}$ and $\boldsymbol{\sigma}_s$ are stress tensors corresponding to the bulk and the interface, respectively. In the following, we will outline key results from Hughes *et al.* (1981) to illustrate key differences between interface- and bulk-dominated systems.

The classic Saffman-Delbrück problem consists of a disk of radius R translating or rotating on a planar insoluble interface of surface viscosity η_s atop an infinitely deep subphase fluid with viscosity η. The drag $\boldsymbol{F}$ against translation at a constant velocity $\boldsymbol{U}$ when the interfacial viscous stresses dominate ($Bq \gg 1$) is (Hughes *et al.* 1981)

$$\boldsymbol{F}(Bq \gg 1) = -\frac{4\pi\eta_s\boldsymbol{U}}{\ln(2Bq) - \gamma_E + 4/(\pi Bq) - \ln(2Bq)/\left(2Bq^2\right)}, \tag{4.156}$$

where γ_E is Euler's constant and the Boussinesq number is $Bq = \eta_s/\eta R = \ell_{\mathrm{SD}}/R$. The Saffman-Delbrück length $\ell_{\mathrm{SD}} = \eta_s/\eta$ (3.102) establishes a 'cutoff' beyond which subphase drag dominates over momentum transfer on the interface.

By contrast, when the drag force is dominated by the subphase ($Bq \ll 1$), the drag on a disk in an insoluble monolayer is

$$\boldsymbol{F}(Bq \ll 1) = -8\eta R\boldsymbol{U}\,. \tag{4.157}$$

This result may at first glance seem surprising, as the drag within an inviscid interface is greater than the drag on a probe translating within a clean interface (Happel & Brenner 1965),

$$\boldsymbol{F}_{\text{clean}} = -\frac{16}{3}\eta R\boldsymbol{U}\,. \tag{4.158}$$

In other words, the simple addition of a surfactant – even with zero surface viscosity – increases the drag on a disk by a factor of 3/2, owing to the effective surface incompressibility boundary condition imposed by the surfactant (§3.3.2) in the limit $Ma \gg 1$.

Reverse Marangoni flows modify surface streamlines, which in turn force the bulk fluid to flow in planes parallel to the interface (figure 11). The excess drag in (4.157) arises due to bulk viscous dissipation associated with this modified flow, and *not* due to surface rheology (Fischer 2004*a*). Only drag forces much larger than (4.157) should be atrributed to surface rheology.

The Saffman-Delbrück problem assumes an infinitely deep subphase, and may not be valid for a finite subphase of depth H. The general solution for arbitrary depth obtained numerically by (Stone & Ajdari 1998) is shown in figure 23. In the shallow subphase limit ($H \ll R$), Evans & Sackmann (1988) used the lubrication approximation (3.96) to obtain

$$\boldsymbol{F}(H \ll R) = -\frac{2\pi\eta R^2}{H}\frac{K_2(1/Bq_1)}{K_0(1/Bq_1)}\boldsymbol{U}, \tag{4.159}$$

where K_n are modified Bessel functions, and Bq_1 is a Boussinesq number modified to account for finite depth:

$$Bq_1^2 = Bq\frac{H}{R} = \frac{\eta_s H}{\eta R^2}\,. \tag{4.160}$$

When drag force is dominated by the subphase ($Bq \ll 1$), (4.159) gives

$$\boldsymbol{F}(H \ll R, Bq \to 0) = -\frac{2\pi\eta R^2}{H}\boldsymbol{U}\,. \tag{4.161}$$

For comparison, the drag on a probe on a clean interface with a shallow subphase is (Barentin *et al.* 1999)

$$\boldsymbol{F}_{\text{clean}}(H \ll R) = -\frac{8\pi\eta R^2}{5H}\boldsymbol{U}\,. \tag{4.162}$$

Even surface-inviscid surfactants thus increase drag on the disk in the shallow subphase limit by 25% due to surface incompressibility (§3.3.2).

All the above discussion was restricted to insoluble and incompressible monolayers.Sur-face pressure gradients set up by moving probes can be relaxed by adsorption/desorption when the surfactant is soluble. Marangoni flows are set up over the time scale $\tau_m = \eta R/E_0$ (3.86), and the mobility relations discussed thus far hold only if sorption is slow ($\tau_s \gg \tau_m$) so that $Ma_K \to \infty$.

For finite Ma_K, the interface still generates Marangoni flows, but the surface flow is compressible. The drag on a probe translating within such an interface has not been computed except in asymptotic limits (Elfring *et al.* 2016). In what follows, we only highlight the limiting case of $Ma_K \to 0$, whereupon Marangoni flows entirely vanish due to rapid surfactant exchange. Any drag in excess of that on a clean interface then arises due to surface viscous stresses. Following Barentin *et al.* (1999), the drag on a disk translating within a monolayer with constant surface pressure ($Ma_K \to 0$) atop a thin subphase ($H \ll R$) is

$$\boldsymbol{F}_{\text{compr}} = -\frac{8\pi\eta R^2}{H}\frac{K_2(1/Bq_1)K_2(1/Bq_2)}{K_2(1/Bq_1)K_0(1/Bq_2) + 4K_0(1/Bq_1)K_2(1/Bq_1)}\boldsymbol{U}, \tag{4.163}$$

where

$$Bq_2^2 = Bq_1^2\frac{(1+\kappa_s/\eta_s)}{4} = Bq\frac{H}{R}\frac{(1+\kappa_s/\eta_s)}{4} \tag{4.164}$$

is yet another modified Boussinesq number that accounts for a surface dilatational viscosity κ_s.

The surface-inviscid ($Bq \to 0$) limit of (4.163) recovers the drag on a clean interface (4.162). In this limit, the surface stress tensor $\boldsymbol{\sigma}_s$ vanishes as $\nabla_s \Pi \to \boldsymbol{0}$ and η_s, $\kappa_s \to 0$, and the only resistance comes from the bulk fluid flow constrained by a stress-free boundary condition. Another interesting limit is $Bq_2 \to \infty$ along with $\kappa_s \gg \eta_s$, so that the surface strongly resists dilatational deformation and the drag is then identical to that of an incompressible monolayer. Table 4 summarizes the interface-/subphase-dominant limits as a function of Bq and H/R.

Rotating circular probes, by contrast, do not perturb surface concentrations and therefore do not establish Marangoni flows or adsorption/desorption fluxes. Rotating disks excite pure shear deformations and the resistance to rotation arises from viscous stresses alone, regardless of the solubility and the Marangoni elasticity of the monolayer. For the same reason, rotating microbuttons (Zell *et al.* 2014) make excellent probes for unambiguous measurements of η_s in interface-dominated systems. The torque on a disk rotating within a monolayer at angular velocity $\boldsymbol{\Omega}$ is

$$\boldsymbol{T}(Bq \gg 1) = -4\pi\eta_s R^2\boldsymbol{\Omega} \tag{4.165}$$

when interface-dominated, and is

$$\boldsymbol{T}(Bq \ll 1) = -\frac{16}{3}\eta R^3\boldsymbol{\Omega} \tag{4.166}$$

when subphase-dominated. The latter recovers the clean interface limit (Happel & Brenner 1965), highlighting a crucial difference between translational and rotational motion on interfaces. No Marangoni flows are set up by pure shear, and the rotational resistance in surface-shear-inviscid monolayers is identical to that in a clean interface.

4.6.2. Elongated particles—Drag coefficients can be evaluated in the same manner for elongated particles (Fischer 2004*b*), flexible particles (Levine *et al.* 2004), or particles that extend into the subphase (Stone & Masoud 2015). We will briefly mention the results for elongated rod-like particles in insoluble (and incompressible) monolayers, due to their applicability in devices like the interfacial stress rheometer (Verwijlen *et al.* 2011).

Consider a rod of length L and width d, where $d \ll L$ and $d \ll \ell_{\mathrm{SD}} = \eta_s/\eta$. The traction on the surface of the rod can then be approximated as a line distribution of point forces, which can be integrated following (4.154). For comparison, translational drag in directions perpendicular and parallel to the long axis of the rod differ by a factor of 2 in 3D bulk fluids:

$$\boldsymbol{F}_{\perp}^{\mathrm{3D}} = 2\boldsymbol{F}_{\parallel}^{\mathrm{3D}} \approx -\frac{4\pi\eta L\boldsymbol{U}}{\ln(aL/d)}, \tag{4.167}$$

where a is a constant. The drag on a rod translating on a clean liquid-gas interface is then $\boldsymbol{F}_{\mathrm{clean}} \approx \boldsymbol{F}^{\mathrm{3D}}/2$.

The drag on a rod translating in an incompressible, interface-dominant monolayer is (Fischer 2004*b*; Levine *et al.* 2004)

$$\boldsymbol{F}_{\parallel,\,\perp}(Bq \gg 1) = -\frac{4\pi\eta_s\boldsymbol{U}}{\ln(8Bq) - \gamma_E \pm 1/2}, \tag{4.168}$$

where $Bq = \ell_{\mathrm{SD}}/L = \eta_s/\eta L$ and the + (or −) applies to motion in a direction parallel (or perpendicular) to the long axis of the rod. Unlike 3D fluids, $\boldsymbol{F}_{\perp} \approx \boldsymbol{F}_{\parallel}$ for translating rods when $Bq \gg 1$. The drag on the particle depends only weakly on its shape and orientation when $L \ll \ell_{\mathrm{SD}}$. In fact, (4.168) closely resembles the leading-order force on a circular disk (4.156), despite significant shape differences.

By contrast, the drag for subphase-dominant systems (particularly, when $d \ll \ell_{\mathrm{SD}} \ll L$),

$$\boldsymbol{F}_{\parallel}(Bq \ll 1) = -\frac{\pi\eta L\boldsymbol{U}}{\ln(0.48/Bq)}, \tag{4.169}$$

resembles the drag on a rod moving in a bulk fluid (4.167), but with an effective width of ℓ_{SD} instead of d. The bulk fluid under the rod does not 'see' the smaller length scale d, and provides bulk viscous resistance to an 'effective' rod of width comparable to the 2D-to-3D crossover length scale ℓ_{SD}. The most striking difference with 3D fluids, however, occurs in perpendicular translation when $Bq \ll 1$:

$$\boldsymbol{F}_{\perp}(Bq \ll 1) = -\pi\eta L\boldsymbol{U}\,. \tag{4.170}$$

The drag on a rod moving broadside-on becomes much larger than $\boldsymbol{F}_{\parallel}$, owing to surface incompressibility. On a clean interface (or on a compressible monolayer with instantaneous adsorption/desorption), Π remains approximately uniform, and the surface flow has a non-zero divergence ahead and behind the rod (figure 24*a*). Insoluble surfactants that impose surface incompressibility (§3.3.2) then perturb velocities over the largest dimension of the rod (figure 24*b*), giving rise to the linear dependence on L.

5. Additional complexities with real-world surfactants

We have thus far treated surfactant monolayers in a way that is natural to most fluid mechanicians – as featureless continuum materials, isotropic and homogeneous. While some multi-component monolayers do form homogeneous mixtures – as do miscible liquids and dissolving solutes in 3D liquids – some surfactant species may associate with each other, or phase separate to form heterogeneous monolayers more akin to emulsions or dispersions. Even single-component monolayers often exhibit non-trivial morphologies, for example, forming condensed phases with liquid crystalline order that coexist with disordered phases. Monolayers in phase coexistence typically consist of 'grains' of one phase dispersed in another, acting like dilute dispersions at low surface pressure, then forming grainy, poly-crystalline phases or jammed suspensions (like compressed emulsions or suspensions) upon further compression, depending on the details and dynamics of compression and domain relaxation.

In what follows, we briefly describe some aspects that give surfactant monolayers additional richness and complexity. §5.1 describes the unexpectedly rich phase behavior and morphologies that arise in even simple surfactant monolayers, and how those can be understood in terms of the characteristics of the surfactants themselves. §5.2 then addresses how monolayer heterogeneities and anisotropies impact the surface rheology and therefore the fluid dynamics of such systems. In many cases, these surface rheologies can be understood by analogy with three-dimensional non-Newtonian fluids: suspensions and emulsions with effective viscosities, surface viscoelasticity, surface shear thinning and surface yield stresses. New phenomena arise in surface rheology as well, as described in §5.3: surface rheology very often depends *exponentially* on surface pressure, which leads to qualitative differences in flow phenomena that would not be expected by a fluid mechanician accustomed to thinking about incompressible, constant-viscosity liquids.

5.1. Phase behavior of surfactant monolayers

In describing Π-Γ isotherms in §2 and table 1, we introduced the simplest of phase transitions: surfactants that experience intermolecular attractions ($\beta > 0$) undergo a phase transformation from a gaseous (G) phase at very low surface concentration Γ to a disordered liquid phase ('liquid expanded,' or LE), frequently with G/LE phase coexistence over a range of Γ, shown in figure 25*d*. Compression to higher Γ often reveals phase behaviors (figure 25) that are significantly richer than the simple gas-liquid transition described by the van der Waals or Frumkin isotherms, forming a host of additional condensed phases with various translational and orientational ordering (Kaganer *et al.* 1999; Knobler & Desai 1992).

Perhaps the simplest, 'canonical' surfactants are saturated fatty alcohols or acids, shown in figure 25(*a*), which consist of a linear alkyl chain as a hydrophobic tail, and a small polar group (e.g. alcohol or carboxilic acid) as the hydrophilic head. Figure 25*b* depicts a generic isotherm for Langmuir monolayers of saturated fatty acids or alcohols. When a disordered liquid (LE) is compressed past a particular concentration Γ_* (or below an area per molecule $A_* = 1/\Gamma_*$), 'liquid condensed' (LC) domains with liquid crystalline ordering nucleate and grow within the continuous, disordered LE phase. Within each LC domain, the hydrophilic

head groups form a hexagonal lattice, and the hydrophobic tails tilt towards neighboring tails to maximize attractive van der Waals interactions (figure 25*e*). The difference between surfactant concentrations (Γ_C and Γ_E) in the LC and LE phases imparts different electrostatic dipole densities to the two phases, giving rise to dipole-dipole repulsions between LC domains that effectively stabilize the dispersion against coalescence (McConnell 1991). Increasing Γ (or decreasing A) grows LC grains at the expense of LE, and ultimately forms a fully LC phase. The LE-LC 'condensation' process reflects a balance between favorable interactions between tilted tails, and unfavorable entropic losses: head groups lose translational entropy by forming lattices, whereas tails lose orientational entropy by tilting. In this balance, lengthening the alkyl tail of a surfactant increases the van der Waals 'benefit' to condensation, with relatively small entropic penalties. Consequently, the melting temperature of the LC phase increases with hydrocarbon tail length, typically by 5–10 K per carbon (Bibo & Peterson 1990).

When facing a fully LC phase, the fluid mechanician might breathe a sigh of relief, in the hopes that LC monolayers act like familiar homogeneous liquids. That fluid mechanician should prepare for disappointment, however. Such LC phases are generally polycrystalline, consisting of compressed LC grains (e.g. figure 27*b*), each of which has a headgroup lattice that is oriented differently from its neighbors; moreover, tail groups generally tilt in one of six energetically equivalent directions relative to the lattice (figures 25*e*, 26*a*–b). Even grains whose headgroup lattices were aligned would only coalesce if their tail tilts were also aligned. The complexity continues: upon further compression, LC monolayers may go through other phase transitions, to any of a veritable menagerie of liquid crystalline phases.

Double bonds within the alkyl tail change the phase behavior rather dramatically. For example, oleic acid is chemically nearly identical to stearic acid, but with one double bond that 'kinks' the tail in a way that frustrates packing with neighboring tails and therefore weakens van der Waals attractions (figure 25 *a*). Unsaturated tails therefore discourage or even prevent liquid condensed phases from forming. In fact, 2D surfactant 'dispersions' can be designed by spreading a mixture of saturated and unsaturated fatty acids or alcohols: upon compression, saturated lipids condense to form LC grains, but unsaturated lipids remain in a continuous LE phase (figure 27 *e*, from Ding *et al.* (2002)).

Phospholipids – the primary surfactants that form the membranes of cells, vesicles and organelles – show even more complex phase behavior than fatty acids. This complexity arises in part because phospholipids have *two* hydrocarbon tails; additionally, these tails attach to the head group in a *chiral* fashion. As with fatty acids, head groups condense to form hexagonal lattices, and (saturated) tails tilt (some towards nearest neighbors, others towards next nearest neighbors). The chiral attachment of each pair of tails, however, promotes a gradual *precession* of tail tilt direction, causing LC domains to 'wind' with a particular handedness (see, e.g., the counter-clockwise spiral arms in LC domains of the common phospholipid Dipalmitoylphosphatidylcholine (DPPC) in figure 27 *a*).

Frustration arises between the packing preferences of the heads and the tails, however, since the tail tilt orientation can only precess by straining the *headgroup* lattice. Since each LC domain represents a single crystal of hexagonally-packed head-groups, this frustration

becomes untenable once LC domains grow large enough. LC DPPC domains ultimately resolve this tension between ordered headgroup lattices and winding tailgroup tilt orientation by forming tilt mosaics (figure 26). Within each ‘patch’ of the mosaic, tail groups tilt in one of 6 directions relative to the HCP lattice, and precess gradually (Dreier *et al.* 2012). Tilt orientation changes discontinuously from one patch of the mosaic to the next, however, across tilt-grain boundary lines where tilt orientations are disordered and thus energetically more costly. These high-energy defects exert additional ‘line tensions’ within the domain. Stretching these LC domains significantly disrupts the balance in frustration between the headgroup lattice and tail tilt precession, and can trigger the nucleation and growth of new tilt grain defects (figure 26 *c*) that stabilize the stretched LC arms against shape relaxation, akin to plastic deformations in solids.

LC DPPC domain shapes thus reflect a variety of competing forces (McConnell 1991; Mohwald 1990; Dreier *et al.* 2012): dipole-dipole repulsions within each domain tend to favor elongation of each domain, whereas the line tension introduced by the higher energetic state of surfactants at the LC/LE boundary acts to reduce the perimeter to area ratio. Tilt orientation precession promotes the chiral winding of spiral arms, which competes with the headgroup lattice trying to maintain its preferred crystaline order. Frustration between tilt precession and headgroup lattice ordering is resolved by high-energy tilt grain boundaries that exert their own line tension within each domain, ‘pulling inwards’ at various points along the domain boundary, causing the concave ‘kinks’ and invaginations along the domain boundary.

Figure 27 highlights a small sliver of the wild menagerie of morphologies formed by condensed mixtures of DPPC and other insoluble surfactants. The chirality of LC DPPC domains is apparent in both LC/LE coexistence (figure 27 *a*) and in the fully condensed, polycrystalline LC phase (figure 27 *a*), growing with the ratio of left- to right-handed DPPC in the mixture (figure 27 *c*), as studied by Kim *et al.* (2018).

Saturated fatty acids or alcohols may co-crystallize with LC phospholipids, since their small head-groups enable them to insert into the head-group lattice without deforming it significantly, while reaping the benefits of tail-tail packing. Such co-crystallization tends to stiffen these domains. Just like fatty acids and alcohols, unsaturated phospholipids generally don’t form LC phases, and so can be used to control the area fraction of LC/LE dispersions (figure 27 *d*, from Ding *et al.* (2002)).

By contrast, cholesterols have small head groups but big ring ‘tails’ that act to promote defects within LC grains. Moreover, just as surfactants lower surface energy when they adsorb to 2D interfaces between 3D liquids, ‘line-actant’ molecules adsorb to 1D boundaries of 2D surfactant domains to lower line energy (Trabelsi *et al.* 2008). Cholesterol is a line-actant for LC-DPPC (Kim *et al.* 2013) and promotes thinner LC spiral arms that wind more tightly (figure 27 *e*). Mixing all three components (phospholipid, fatty alcohol, and cholesterol) forms LC grains that are as complex as they are beautiful: stiff ‘cores’ of DPPC-hexadecanol form first, followed by wispy spirals of DPPC-cholesterol mixtures (figure 27 *f*, from (Sachan *et al.* 2017)).

These examples serve only to give a very cursory sense of the incredibly rich variety of monolayers, phases, and domains that form in even seemingly simple systems with one or two small-molecule surfactants. Additional complexities arise when solutes in the subphase interact with surfactants in the monolayer. Multivalent ions may electrostatically bridge multiple ionic surfactants: for example, calcium ions (Ca^{2+}) adsorb to two stearic acid molecules, stiffening monolayers (Ghaskadvi *et al.* 1999) and even growing multilayer films of calcium distearate (de Ruiter *et al.* 2011). However exotic and beautiful this process may appear to the curious scientist, those who shower with 'hard' water call it soap scum.

5.2. Rheological implications of surface heterogeneities

Because surfactant monolayers are frequently heterogeneous (e.g. figure 27), determining their rheological properties and predicting their mechanical response to flows and stresses can be challenging. A detailed discussion of the complex structure and non-Newtonian rheology of surfactant monolayers is beyond the scope of this work, and recent reviews provide a more exhaustive survey of the state of the field Fuller & Vermant (2012); Langevin (2014); Jaensson & Vermant (2018). Instead, in what follows, we merely outline aspects of 2D heterogeneous monolayers that qualitatively resemble familiar 3D systems, and where intuition and physical concepts from classical fluid dynamics can be borrowed to describe and design these 2D systems.

5.2.1. Line tension: liquid crystalline domains as 2D drops—Recall from §2.1 that molecules on the interface between 3D fluids are in an energetically unfavorable state, giving rise to surface tension (figure 2). The 2D analog occurs on the 'interface' between surfactant phases – LC domain boundaries are higher energy and give rise to a line tension λ, or energy per unit perimeter. The attractive interaction energy between molecules in the condensed phase must be $O(k_BT)$. Condensation involves moving molecules from the disordered phase to LC and therefore requires an energy ~ k_BT per molecule. Molecules pack with a line density of about one per nanometer, giving $\lambda \sim k_BT/\text{nm} \sim$ pN.

Just like surface tension acts to restore the equilibrium shapes of deformed, 3D emulsion drops or bubbles, the LC line tension acts to force deformed LC domains to relax back to their equilibrium shapes, at a rate that is limited by the surface viscosity of the LC phase when $Bq \gg 1$ (or by subphase viscosity when $Bq \ll 1$). Indeed, λ can be identified by measuring the relaxation dynamics of stretched LC 'droplets' (Mann *et al.* 1995; Trabelsi *et al.* 2008). When interface-dominant ($Bq \gg 1$), balancing the line tension force (~ λ) with the surface viscous force (~$\eta_s\dot{R}$, with R the characteristic domain length scale) gives a characteristic relaxation time

$$T_c(Bq \gg 1) \sim \frac{\eta_s R}{\lambda}. \tag{5.1}$$

By contrast, the bulk fluid offers the dominant viscous resistance (~ $\eta R\dot{R}$) when subphase-dominant ($Bq \ll 1$), giving

$$T_c(Bq \ll 1) \sim \frac{\eta R^2}{\lambda}. \tag{5.2}$$

Extending the analogy, fully LC phases act like compressed emulsions – like two-dimensional mayonnaise. Interlocking domains impart a yield stress to fully LC monolayers, enabling them to sustain elastic stresses over system-spanning lengthscales. The dynamics of LC domains are then described by a surface capillary number,

$$Ca_s = \frac{\eta_s V}{\lambda}, \tag{5.3}$$

which for domains of some size R, sheared at rate $\dot{\gamma}$ or frequency ω, becomes

$$Ca_s = \frac{\eta_s R\omega}{\lambda}, \quad Ca_s = \frac{\eta_s R\dot{\gamma}}{\lambda}. \tag{5.4}$$

Surface capillary stresses dominate at low frequencies, acting to restore domain shapes and imparting a solid-like response. By contrast, viscous stresses dominate at high frequencies, as the LC phase resists deformation within each grain. From the crossover frequency ω_c, the line tension can be identified (Choi *et al.* 2011).

The healing of deformed LC monolayers, however, is qualitatively different from traditional yield-stress materials. Unlike 3D drops, elongated domains do not 'pinch off' due to capillary forces. The classic Rayleigh-Plateau instability is suppressed by the absence of out-of-plane curvature of LC domains. Even thread-like domains are therefore stable for long times (Trabelsi *et al.* 2008). Deformed LC phases heal via line-tension-driven relaxation of highly stretched domains back to more compact equilibrium shapes. Additional viscous losses may be incurred in sliding domains against each other, or in irreversible topological rearrangements. The net effect is a viscoelastic recovery – one that can take hours (Choi *et al.* 2011).

5.2.2. 2D 'suspensions' of condensed domains: effective surface viscosities

Liquid condensed phases are typically much stiffer rheologically than LE phases. Langmuir monolayers in LE-LC phase coexistence can thus be treated as a suspension of 'stiff' 2D particles dispersed in a continuous 'liquid'. In fact, Ding *et al.* (2002) measured the effective surface shear viscosity of DPPC-palmitic acid mixtures over a wide range of LE-LC coexistence, finding a power-law divergence

$$\eta_s^{\text{eff}} \sim \frac{1}{(1 - A/A_c)^n}, \tag{5.5}$$

as the domain area A approached some critical area A_c. Analogous behavior had been known and shown in 3D suspensions (Brady 1993; Stickel & Powell 2005).

In system where domains are effectively rigid inclusions suspended in an incompressible, continuous phase that is surface viscous enough to be interface dominant ($Bq \gg 1$), the

subphase may be ignored and the monolayer rheology corresponds to the Einstein viscosity correction in 2D. This classic problem in low-Reynolds-number hydrodynamics (Brady 1983) gives the effective shear viscosity of a 2D suspension with a domain area fraction $\phi \ll 1$ to be

$$\eta_s^{\text{eff}}(Bq \gg 1) = \eta_s^c(1 + 2\phi), \tag{5.6}$$

Where η_s^c is the surface shear viscosity of the continuous phase.

Additionally, surfactant monolayers are far more compressible than 3D fluids, and the flow of a compressible 2D 'fluid' around incompressible domains dissipates excess surface viscous stresses. The 'Einstein correction' to the 2D dilatational viscosity is (Khair 2006)

$$\kappa_s^{\text{eff}}(Bq \gg 1) = \frac{\kappa_s^c + \phi\eta_s^c}{1 - \phi}, \tag{5.7}$$

where κ_s^c is the dilatational surface viscosity of the continuous phase. Notably, κ_s^{eff} depends on the surface *shear* viscosity of the continuous phase, η_s^c. Even if κ_s^c is immeasurably small, rigid inclusions modify surface flows in a manner that imparts an effective dilatational viscosity $\kappa_s^{\text{eff}} \approx \phi\eta_s^c$ to the monolayer.

Stiff inclusions suspended in an inviscid monolayer, e.g. a dispersion of repulsive colloidal microparticles on a clean fluid interface, might also impart an effective surface shear viscosity (Buttinoni *et al.* 2015). The colloids do not deform, and the suspending fluid interface is clean and therefore offers no surface viscous resistance. Viscous dissipation in the *subphase* fluid due to the relative motion of colloids against interparticle potentials appears as a 'surface viscosity' of the 2D colloidal layer.

5.2.3. Apparent surface dilatational rheology during phase coexistence—

§4.2.1 described how dynamic adsorption and desorption of soluble surfactants as an interface is compressed relaxes surface stresses, thereby diminishing the dilatational modulus E and imparting an apparent surface viscosity $\kappa_s^{\text{app}} \sim E_0\tau_s$. Similar processes can arise within monolayers at phase coexistence, where exchange between condensed and expanded phases plays a role analogous to adsorption/desorption. To illustrate, we treat the kinetics of exchange between phases with a simple adsorption-like model, using Γ_C and Γ_E to represent the surface concentration in the condensed and expanded phases, respectively. The total number of molecules is conserved between the two phases,

$$\frac{1}{A_E}\frac{\mathrm{d}(\Gamma_E A_E)}{\mathrm{d}t} = -j_p, \tag{5.8a}$$

$$\frac{1}{A_C}\frac{\mathrm{d}(\Gamma_C A_C)}{\mathrm{d}t} = j_p, \tag{5.8b}$$

where j_p is the net line flux (across domain boundaries) as a result of molecules hopping between phases, and A_E and A_C are the areas of the expanded and condensed phase, respectively.

Rheologically, we assume that the condensed domains act like rigid inclusions, so that all compressibility (and fluidity) of the heterogeneous monolayer originates in the expanded phase. Under weak sinusoidal surface dilatation at frequency ω, the surface concentration and area of the expanded phase are perturbed via:

$$A_E(t) = A_E^0 + \delta A_E e^{i\omega t}, \tag{5.9a}$$

$$\Gamma_E(t) = \Gamma_E^0 + \delta \Gamma_E e^{i\omega t}. \tag{5.9b}$$

The condensed phase concentration $\Gamma_C(t)$ is assumed to remain a constant Γ_C^0.

Although the exchange flux j_p could be diffusion- or kinetically-limited, we will assume a simple kinetically-limited condensation process, with the flux from either phase proportional to the local concentration:

$$j_{E\to C} = k_{E\to C}\Gamma_E, \quad j_{C\to E} = k_{C\to E}\Gamma_C = j_C^0, \tag{5.10}$$

so that $j_{E\to C} = j_{C\to E}$ at equilibrium. When perturbed via (5.9), the net flux into (or out of) the condensed phase is

$$j_p = j_{E\to C} - j_{C\to E} = k_p \delta \Gamma_E e^{i\omega t}, \tag{5.11}$$

where $k_p = j_C^0/\Gamma_E^0$. Perturbations in surface concentration thus relax over a timescale k_p^{-1}.

Substituting (5.9) and (5.11) in the conservation equation (5.8*a*) gives

$$\frac{\mathrm{d}\ln\Gamma_E}{\mathrm{d}\ln A_E} = -\frac{1}{1 - i\zeta_p}, \tag{5.12}$$

where

$$\zeta_p = \frac{k_p}{\omega} \tag{5.13}$$

is the ratio of phase change rate to oscillation rate.

When $\zeta_p \gg 1$, condensed domains incorporate excess molecules from the expanded phase much faster than Γ oscillates, so that the monolayer evolves quasistatically. Conversely, when $\zeta_p \ll 1$, compression oscillates so rapidly that little condensation can occur (figure 28).

Because the condensed phase domains are assumed incompressible, the compressibility modulus originates from the expanded phase, giving:

$$E^* = E^* = E^{\text{app}} + i\omega\kappa_s^{\text{app}} = -\frac{\mathrm{d}\Pi}{\mathrm{d}\ln A} = -E_0^{LE}\frac{\mathrm{d}\ln\Gamma_E}{\mathrm{d}\ln A_E}, \tag{5.14}$$

where

$$E_0^{LE} = \frac{\mathrm{d}\Pi}{\mathrm{d}\ln\Gamma_E} \tag{5.15}$$

is the Marangoni modulus of the expanded phase. Substituting (5.12) in (5.14), the apparent surface dilatational elasticity and viscosity are

$$E^{\text{app}} = E_0^{LE}\frac{1}{1+\zeta_p^2}, \quad \kappa_s^{\text{app}} = \frac{E_0^{LE}}{\omega}\frac{\zeta_p}{1+\zeta_p^2}. \tag{5.16}$$

Equation (5.16) has the form of a Maxwell fluid with a characteristic relaxation timescale $\tau = k_p^{-1}$, analogous to kinetic-limited adsorption of soluble surfactants (4.51).

Domains grow freely in the low-frequency limit ($\omega \ll k_p$ or $\zeta_p \gg 1$) and the LE phase offers no resistance to compression (figure 28*a*). By contrast, a finite and rate-dependent dilatational modulus emerges during the LE-LC coexistence when the compression rate and phase change rate are comparable, which derives from temporary compression of the LE 'fluid' before phase change has had a chance to occur. For surfactants with inherent surface viscosity (§3.4), measured surface dissipation must be interpreted as the appropriate combination of a true material property and apparent rate-dependent contributions due to phase changes and adsorption/desorption.

5.3. Non-constant surface viscosity

All discussion of surface rheology thus far has assumed surface shear and dilatational viscosities to be constant. However convenient this approximation may be, many factors can impart spatial, temporal, and concentration-based heterogenities to surface rheological properties. Phase transitions in Langmuir monolayers are typically accompanied by changes in surface viscous and elastic properties. Liquid condensed domains can deform, reorient, jam, or slip against each other in response to hydrodynamic forcing, leading to non-Newtonian behavior. This nonlinear behavior depends on the precise phase behavior, which in turn varies based on surfactant type, hydrocarbon chain length, chain orientation and intermolecular interactions, as described in §5.1. An exhaustive discussion on the resulting non-Newtonian behavior is beyond the scope of this work, and we direct the reader to Fuller & Vermant (2012) and references within. Here, we will only provide a flavor of the richness and uniqueness of non-Newtonian surface rheology by outlining two examples – one with familiar 3D analogs, and another which is almost never observed in 3D – both of which arise due to phase transitions in Langmuir monolayers.

5.3.1. Surface-shear-thickening and -thinning—Gradients in surface pressure drive flows along interfaces, just like bulk pressure gradients drive (Poiseuille) flows in pipes. For example, increasing the surface pressure on one end of an interfacial slit 'pumps' a

monolayer through a 2D channel, making a 2D analog of a syringe (Schwartz *et al.* 1994; Fuller & Vermant 2012). Indeed, the subphase decouples from the interfacial stress balance (3.94) when interface-dominant ($Bq = \eta_s/\eta R \gg 1$), and the surface velocity $u_s(y)$ of an incompressible monolayer obeys the familiar parabolic profile of Poiseuille flow in 2D:

$$u_s(y, Bq \gg 1) = -\frac{R^2}{\eta_s}\frac{\mathrm{d}\Pi}{\mathrm{d}x}\left(1 - \frac{y^2}{R^2}\right), \tag{5.17}$$

where R the slit half-width (figure 29*a*).

However, viscous coupling with the subphase modifies the surface flow from (5.17). When subphase-dominant ($Bq \ll 1$), the solution to the incompressible Boussinesq-Scriven equation (3.94) is (Stone 1995)

$$u_s(y, Bq \ll 1) = -\frac{R}{\eta}\frac{\mathrm{d}\Pi}{\mathrm{d}x}\sqrt{1 - \frac{y^2}{R^2}}\,. \tag{5.18}$$

Subphase-dominant flow (5.18) is insensitive to η_s, and the flow profile is elliptic rather than parabolic, consistent with direct observation of Langmuir monolayers of negligible surface shear viscosity (Schwartz *et al.* 1994).

Increasing the surface shear viscosity – e.g. by compressing the monolayer so that rheologically stiff domains nucleate – transitions the surface velocity from (5.18) to (5.17). However, direct observation of the velocity profiles of heterogeneous arachidic acid monolayers by Kurnaz & Schwartz (1997) reveals a non-Newtonian viscous response (figure 29 *b*). The velocity profile is shear-rate-dependent at sufficiently large flow rates, and approximately fits

$$u_s \propto 1 - \left(\frac{y}{R}\right)^{(1+\alpha)/\alpha}, \tag{5.19}$$

with $\alpha > 1$ when surface-shear-thickening, and $0 < \alpha < 1$ when surface-shear-thinning.

Kurnaz & Schwartz (1997) observed shear-thinning in arachidic acid monolayers at high shear rates ($\gtrsim 0.1\ \mathrm{s}^{-1}$) and low surface pressures, but shear-thickening at higher Π. The transition between the two occurs around $\Pi \approx 20$ mN/m, where arachidic acid undergoes a tail group tilt-untilt transition (Kaganer *et al.* 1999). This phase transition is associated with changes in surface rheology (Kurtz *et al.* 2006; Zell *et al.* 2014), suggesting that surfactant phase behavior is at least in part responsible for the non-Newtonian dynamics. Other classes of surfactants show rate-dependent rheology upon phase transition as well; e.g. power-law models capture experimentally measured surface-shear thinning of DPPC at high surface pressures (Raghunandan *et al.* 2018).

5.3.2. Π-dependent viscosity—Surface viscosities of Langmuir monolayers change appreciably over surface pressure variations accessible in typical experiments. For instance, the surface shear viscosity of DPPC grows exponentially when Π is increased from 5 to 15 mN/m (Kim *et al.* 2011, 2013; Fuller & Vermant 2012; Hermans & Vermant 2014), unlike

3D liquids which show such changes only under truly extreme pressures. The exponential dependence of surface viscosity on surface pressure can be understood in terms of the free-area analog of classical free-volume theories of viscosity (Kim *et al.* 2013), and can be written as

$$\eta_s(\Pi) = \eta_s^0 e^{(\Pi - \Pi_0)/\Pi_c}, \tag{5.20}$$

where Π_c is a characteristic surface pressure change required to appreciably change η_s, and η_s^0 is a reference viscosity at reference pressure Π_0. DPPC is a 'Π-thickening' surfactant with $\Pi_c \approx 8$ mN/m, whereas setting $\Pi_c \to \infty$ in (5.20) retrieves the Newtonian limit of constant η_s.

By contrast, the surface viscosity of some surfactants decreases with increasing surface pressure. For example, the surface viscosity of eicosanol (Kurtz *et al.* 2006; Zell *et al.* 2014) drops tenfold upon increasing Π from 10 to 20 mN/m as it undergoes a tilt-untilt transition (Kaganer *et al.* 1999). Such 'Π-thinning' behavior can be modeled as in (5.20) by inverting the sign of Π_c: for eicosanol, $\Pi_c \sim -3$ mN/m.

The fact that η_s can vary over orders of magnitude in rather mundane flows gives rise to qualitatively new flow phenomena. For example, flow through a thin gap (figure 29) amplifies surface pressure variations and therefore accentuate the Π-dependent nature of η_s. Using lubrication theory, the interface-dominant ($Bq \gg 1$) incompressible Boussinesq-Scriven equation reduces to (Manikantan & Squires 2017*b*)

$$\frac{\partial \Pi}{\partial x} = \eta_s(\Pi)\frac{\partial^2 u_s}{\partial y^2}. \tag{5.21}$$

Fortunately, (5.21) is solvable by separation despite the strong nonlinearity of η_s, whether using the assumed form (5.20) or a measured $\eta(\Pi)$.

The impact of surface-pressure-dependent surface viscosity is best illustrated using the flux pumped through the channel. For a surface pressure gradient $\Delta\Pi$ applied across a channel of length $L \gg R$, the interfacial flux Q is (Manikantan & Squires 2017*b*)

$$Q = \frac{2}{3}\frac{\Pi_c R^3}{\eta_s^0 L}\left(1 - e^{-\Delta\Pi/\Pi_c}\right). \tag{5.22}$$

The familiar Newtonian flux is recovered when $\Pi_c \gg \Delta\Pi$:

$$Q(\Delta\Pi \ll \Pi_c) \to Q_{\text{Newt}} = \frac{2}{3}\frac{\Delta\Pi R^3}{\eta_s^0 L}. \tag{5.23}$$

Qualitative differences arise when $\Delta\Pi$ is comparable to Π_c. Indeed, Q approaches a limiting value when $\Delta\Pi \gg \Pi_c$ for a Π-thickening surfactant ($\Pi_c > 0$):

$$Q(\Delta\Pi \gg \Pi_c) \to Q_{\max} = \frac{2}{3}\frac{\Pi_c R^3}{\eta_s^0 L}, \tag{5.24}$$

which is insensitive to $\Delta\Pi$, with Π_c effectively setting the surface pressure scale beyond which the channel is 'choked'. When $\Delta\Pi \gg \Pi_c$, the surface pressure drops rapidly near the entrance of the channel, where the surface viscosity is extremely high. The pressure in the rest of the channel remains of the order of Π_c, setting the scale for the maximum flux that may be pumped through the channel.

Similarly, Q grows exponentially with applied surface pressure difference when $\Delta\Pi \gg |\Pi_c|$ for a Π-thinning surfactant ($\Pi_c < 0$). For large $\Delta\Pi$, therefore, Π-thinning increases channel 'permeability'. Indeed, some surfactants (e.g. arachidic acid) might simultaneously shear-thicken and Π-thin, so that the monolayer may be more permeable through an interfacial slit than is expected for traditional shear-thickening materials (Kurnaz & Schwartz 1997).

While thin gaps naturally give rise to large surface pressures and are easier to approach analytically, the consequences of Π-dependent η_s are not restricted to lubrication flows (Manikantan & Squires 2017*a*). For example, a disc translating while rotating on an unbounded and otherwise undisturbed Π-thickening/thinning monolayer experiences a force perpendicular to the direction of motion, analogous to the 3D Magnus effect (figure 30), breaking the reversibility expected from Stokes flows. More generally, Π-dependent surface viscosities result in non-intuitive and kinematically irreversible trajectories of pairs of particles on the interface, which could lead to hydrodynamic aggregation, separation, and 'lane formation'.

6. Conclusion

However long this Perspective may seem, it has at most laid out an intellectual skeleton for the mechanics and dynamics of surfactants in fluid systems. We have omitted many complications and subtleties that impact many different fields of science, industry, and life. Still, we hope to have helped bridge the gap between the fluid mechanics community and the surfactant communities in physical chemistry, colloid and interface science.

We close this perspective with a philosophical reflection on the admittedly loose analogy we drew between surfactants in fluid dynamical systems, and the 'hidden variables' that were desperately sought in the early decades of quantum mechanics. As fluid mechanicians, we do not often stop to appreciate how remarkable the Navier-Stokes equations have been in capturing flows from nanometers to thousands of kilometers (fifteen orders of magnitude!) In many cases – particularly in turbulent flows – the challenges in solving fluid mechanics problems relate to the actual challenges in the mechanics of solving those problems. More powerful computers, more efficient algorithms, and more insightful approximations are sought to improve predictions, elucidate new mechanisms, and design new technologies. The basic equations that need to be solved, however, are generally not in question.

Surfactants, by contrast, introduce something different to the study of fluid systems. Although surfactants generally do nothing to alter the Navier Stokes equations that govern

the bulk fluid, they do change the boundary conditions that constrain them – and in so doing, completely change both the quantitative and qualitative aspects of the flow. As should be evident from this Perspective, any particular change in observed dynamics might be caused by any of a number of distinct surfactant processes. Moreover, the 'invisible' nature of surfactants makes it difficult to know a *priori* what the surfactant is actually doing. This lands the typical fluid mechanician in unfamiliar terrain – of needing to determine what equations and boundary conditions must be solved in order to understand a fluid system, and ultimately predict its behavior. We hope that our Perspective will help provide a conceptual map for this endeavor.

Finally, we close by noting that surfactants are by no means the only 'hidden variables' in fluid systems. So-called 'complex fluids' impact almost every industry and every aspect of life: shampoos and toothpastes, eggs and espressos, blood and mucous, paints, vaccines, lubricants and drilling muds. These natural and 'formulated' products generally contain a multitude of ingredients – liquids, solutes, surfactants, colloids, and polymers – that impart mesostructures of various length scales, and affect the dynamic response properties on a variety of time scales. Still, these materials often appear homogeneous when viewed macroscopically. To understand, design, and model the dynamics of these systems, one must identify and incorporate the additional concentration and stress fields associated by each component. And – just like with surfactants – one must often determine the actual equations that govern these additional components. The challenges are both rich and rewarding, and offer fertile ground for the curious fluid mechanician.

Acknowledgments

We gratefully acknowledge support from the National Science Foundation (NSF) under grant no. CBET-1512833 for support of this work, and from the National Heart, Lung, and Blood Institute of the National Institutes of Health under grant number R01HL135065. The content is solely the responsibility of the authors and does not necessarily represent the official views of the National Institutes of Health or the National Science Foundation. We gratefully acknowledge Howard Stone for his particularly thorough and critical reading, insight and suggestions, and Lynn Walker for sharing her expertise, her insightful critiques and valuable perspective. We are grateful to Ian Williams, Gwynn Elfring, Aditya Khair, Paul Linden and Joseph Zasadzinski for critical reading, comments, and discussions, and to Ian Williams for the unpublished image in figure 25*d*.

REFERENCES

Adamson AW 1990 Physical Chemistry of Surfaces. John Wiley & Sons, Inc.

Agrawal S & Wasan D 1979 The effect of interfacial viscosities on the motion of drops and bubbles. The Chemical Engineering Journal 18 (2), 215–223.

Alpers W & Hühnerfuss H 1989 The damping of ocean waves by surface films: A new look at an old problem. Journal of Geophysical Research 94 (C5), 6251.

Alvarez NJ, Vogus DR, Walker LM & Anna SL 2012 Using bulk convection in a microtensiometer to approach kinetic-limited surfactant dynamics at fluid-fluid interfaces. Journal of Colloid and Interface Science 372 (1), 183 – 191. [PubMed: 22326047]

Alvarez NJ, Walker LM & Anna SL 2010a A microtensiometer to probe the effect of radius of curvature on surfactant transport to a spherical interface. Langmuir 26 (16), 13310–13319. [PubMed: 20695573]

Alvarez NJ, Walker LM & Anna SL 2010b Diffusion-limited adsorption to a spherical geometry: The impact of curvature and competitive time scales. Physical Review E 82 (1), 011604.

Aris R 1962 Vectors, Tensors, and the Basic Equations of Fluid Mechanics. Englewood Cliffs, New Jersey: Prentice-Hall.

Arriaga LR, Lopez-Móntero I, Ignés-Mullol J & Monroy F 2010 Domain-growth kinetic origin of nonhorizontal phase coexistence plateaux in langmuir monolayers: Compression rigidity of a raft-like lipid distribution. The Journal of Physical Chemistry B 114 (13), 4509–4520. [PubMed: 20235509]

Barentin C, Ybert C, Di Meglio J-M & Joanny J-F 1999 Surface shear viscosity of Gibbs and Langmuir monolayers. Journal of Fluid Mechanics 397, 331–349.

Bhamla MS, Giacomin CE, Balemans C & Fuller GG 2014 Influence of interfacial rheology on drainage from curved surfaces. Soft Matter 10 (36), 6917–6925. [PubMed: 25140576]

Bibette J, Morse DC, Witten TA & Weitz DA 1992 Stability criteria for emulsions. Physical Review Letters 69 (16), 2439–2442. [PubMed: 10046485]

Bibo AM & Peterson IR 1990 Phase diagrams of monolayers of the long chain fatty acids. Advanced Materials 2 (6–7), 309–311.

Binks BP 2002 Particles as surfactants — similarities and differences. Current Opinion in Colloid & Interface Science 7 (1–2), 21–41.

Bond W & Newton DA 1928 Bubbles, drops, and Stokes' law. (Paper 2). The London, Edinburgh, and Dublin Philosophical Magazine and Journal of Science 5 (30), 794–800.

Boussinesq MJ 1913 Speed of the slow, uniform fall of a liquid spherical drop in a viscous fluid of lesser specific weight. Ann. Chim. Phys 29, 364–371.

Brady JF 1983 The Einstein viscosity correction in n dimensions. International Journal of Multiphase Flow 10 (1), 113–114.

Brady JF 1993 The rheological behavior of concentrated colloidal dispersions. J. Chem. Phys 99, 567–581.

Brooks CF, Fuller GG, Frank CW & Robertson CR 1999 An interfacial stress rheometer to study rheological transitions in monolayers at the air-water interface. Langmuir 15 (7), 2450–2459.

Buttinoni I, Zell ZA, Squires TM & Isa L 2015 Colloidal binary mixtures at fluid-fluid interfaces under steady shear: structural, dynamical and mechanical response. Soft Matter 11 (42), 8313–8321. [PubMed: 26347409]

Buzza DMA, Lu D, C.-Y. & Cates ME 1995 Linear shear rheology of incompressible foams. Journal de Physique II 5 (1), 37–52.

Choi SQ, Steltenkamp S, Zasadzinski JA & Squires TM 2011 Active microrheology and simultaneous visualization of sheared phospholipid monolayers. Nature communications 2 (May), 312.

Cohen-Addad S, Höhler R & Pitois O 2013 Flow in foams and flowing foams. Annual Review of Fluid Mechanics 45 (1), 241–267.

Dai B & Leal LG 2008 The mechanism of surfactant effects on drop coalescence. Physics of Fluids 20 (4), 040802.

Darhuber AA & Troian SM 2005 Principles of microfluidic actuation by modulation of surface stresses. Annu. Rev. Fluid Mech 37 (1), 425–55.

Davies JT & Vose RW 1965 On the damping of capillary waves by surface films. Proceedings of the Royal Society A: Mathematical, Physical and Engineering Sciences 286 (1405), 218–234.

Delacotte J, Montel L, Restagno F, Scheid B, Dollet B, Stone HA, Langevin D & Rio E 2012 Plate coating: Influence of concentrated surfactants on the film thickness. Langmuir 28 (8), 3821–3830. [PubMed: 22283676]

Diamant H & Andelman D 1996 Kinetics of surfactant adsorption at fluid-fluid interfaces. The Journal of Physical Chemistry 100 (32), 13732–13742.

Ding J, Warriner HE & Zasadzinski JA 2002 Viscosity of two-dimensional suspensions. Physical Review Letters 88 (16), 168102. [PubMed: 11955269]

Dreier J, Brewer J & Simonsen AC 2012 Texture defects in lipid membrane domains. Soft Matter 8 (18), 4894.

Durand M & Langevin D 2002 Physicochemical approach to the theory of foam drainage. European Physical Journal E 7 (1), 35–44.

Durand M, Martinoty G & Langevin D 1999 Liquid flow through aqueous foams: From the Plateau border-dominated regime to the node-dominated regime. Physical Review E 60 (6), R6307–R6308.

Edwards DA, Brenner H & Wasan DT 1991 Interfacial Transport Processes and Rheology. Butterworth-Heinemann.

Elfring GJ, Leal LG & Squires TM 2016 Surface viscosity and Marangoni stresses at surfactant laden interfaces. Journal of Fluid Mechanics 792, 712–739.

Evans E & Sackmann E 1988 Translational and rotational drag coefficients for a disk moving in a liquid membrane associated with a rigid substrate. Journal of Fluid Mechanics 194 (−1), 553.

Fischer TM 2004a Comment on “Shear viscosity of Langmuir monolayers in the low-density limit”. Physical Review Letters 92 (13), 139603. [PubMed: 15089651]

Fischer TM 2004b The drag on needles moving in a Langmuir monolayer. Journal of Fluid Mechanics 498, 123–137.

Franklin B, Brownrigg W & Farish M 1774 Of the stilling of waves by means of oil. Philosophical Transactions of the Royal Society of London 64, 445–460.

Fuller GG & Vermant J 2012 Complex fluid-fluid interfaces: Rheology and structure. Annual Review of Chemical and Biomolecular Engineering 3 (1), 519–543.

Furst EM & Squires TM 2017 Microrheology. Oxford University Press.

Ghaskadvi RS, Carr S & Dennin M 1999 Effect of subphase Ca^{++} ions on the viscoelastic properties of Langmuir monolayers. J. Chem. Phys 111 (8), 3675.

Goodrich FC 1969 The theory of absolute surface shear viscosity. I. Proceedings of the Royal Society A: Mathematical, Physical and Engineering Sciences 310 (1502), 359–372.

Guazzelli E & Morris JF 2012 A Physical Introduction to Suspension Dynamics. Cambridge University Press.

Hansen RS 1961 Diffusion and the kinetics of adsorption of aliphatic acids and alcohols at the water-air interface. Journal of Colloid Science 16 (6), 549–560.

Happel J & Brenner H 1965 Low Reynolds Number Hydrodynamics. Prentice-Hall.

Hermans E, Saad Bhamla M, Kao P, Fuller GG & Vermant J 2015 Lung surfactants and different contributions to thin film stability. Soft Matter 11 (41), 8048–8057. [PubMed: 26307946]

Hermans E & Vermant J 2014 Interfacial shear rheology of DPPC under physiologically relevant conditions. Soft Matter 10 (1), 175–186. [PubMed: 24651838]

Hughes BD, Pailthorpe BA & White LR 1981 The translational and rotational drag on a cylinder moving in a membrane. Journal of Fluid Mechanics 110 (−1), 349.

Israelachvili J 2011 Intermolecular and Surface Forces. Academic Press.

Jaensson N & Vermant J 2018 Tensiometry and rheology of complex interfaces. Curr. Opin. Colloid Interf. Sci 37, 136–150.

Jeffreys H 1930 The draining of a vertical plate. Mathematical Proceedings of the Cambridge Philosophical Society 26 (2), 204–205.

Jin F, Balasubramaniam R & Stebe KJ 2004 Surfactant adsorption to spherical particles: The intrinsic length scale governing the shift from diffusion to kinetic-controlled mass transfer. The Journal of Adhesion 80 (9), 773–796.

Johnson DO & Stebe KJ 1994 Oscillating bubble tensiometry: A method for measuring the surfactant adsorptive-desorptive kinetics and the surface dilatational viscosity. Journal of Colloid and Interface Science 168 (1), 21–31.

Kaganer V, Möhwald H & Dutta P 1999 Structure and phase transitions in Langmuir monolayers. Reviews of Modern Physics 71 (3), 779–819.

Khair AS 2006 The ‘Einstein correction’ to the bulk viscosity in n dimensions. Journal of Colloid and Interface Science 302 (2), 702–703. [PubMed: 16919667]

Kim K, Choi SQ, Zasadzinski JA & Squires TM 2011 Interfacial microrheology of DPPC monolayers at the air–water interface. Soft Matter 7 (17), 7782.

Kim K, Choi SQ, Zasadzinski JA & Squires TM 2018 Nonlinear chiral rheology of phospholipid monolayers. Soft Matter 14, 2476–2483. [PubMed: 29561060]

Kim K, Choi SQ, Zell ZA, Squires TM & Zasadzinski JA 2013 Effect of cholesterol nanodomains on monolayer morphology and dynamics. Proceedings of the National Academy of Sciences 110 (33), E3054–E3060.

Knobler CM & Desai RC 1992 Phase transitions in monolayers. Annual Review of Physical Chemistry 43 (1), 207–236.

Koehler SA, Hilgenfeldt S & Stone HA 2000 A generalized view of foam drainage: Experiment and theory. Langmuir 16 (15), 6327–6341.

Kotula AP & Anna SL 2016 Insoluble layer deposition and dilatational rheology at a microscale spherical cap interface †. — Soft Matter 12, 7038. [PubMed: 27478885]

Kralchevsky P, Danov K & Denkov N 2008 Chemical physics of colloid systems and interfaces. In Handbook of Surface and Colloid Chemistry, Third Edition, pp. 197–377. CRC Press.

Krishna R 1990 Multicomponent surface diffusion of adsorbed species: a description based on the generalized Maxwell—Stefan equations. Chemical Engineering Science 45 (7), 1779–1791.

Kurnaz M & Schwartz D 1997 Channel flow in a Langmuir monolayer: Unusual velocity profiles in a liquid-crystalline mesophase. Physical Review E 56 (3), 3378–3384.

Kurtz RE, Lange A & Fuller GG 2006 Interfacial rheology and structure of straight-chain and branched fatty alcohol mixtures. Langmuir 22 (12), 5321–5327. [PubMed: 16732659]

Landau L & Levich B 1942 Dragging of liquid by a plate. Acta Physicochimica URSS 17, 42–54.

Langevin D 2000 Influence of interfacial rheology on foam and emulsion properties. Advances in Colloid and Interface Science 88 (1–2), 209–222. [PubMed: 11185698]

Langevin D 2014 Rheology of adsorbed surfactant monolayers at fluid surfaces. Annual Review of Fluid Mechanics 46 (1), 47–65.

Leal LG 2004 Flow induced coalescence of drops in a viscous fluid. Physics of Fluids 16 (6), 1833–1851.

Leal LG 2007 Advanced Transport Phenomena. Cambridge University Press.

Levich VG 1962 Physicochemical Hydrodynamics. Prentice-Hall.

Levine AJ, Liverpool T & MacKintosh F 2004 Dynamics of rigid and flexible extended bodies in viscous films and membranes. Physical Review Letters 93 (3), 038102. [PubMed: 15323875]

Levine AJ & MacKintosh FC 2002 Dynamics of viscoelastic membranes. Physical Review E 66 (6), 061606.

Lubensky DK & Goldstein RE 1996 Hydrodynamics of monolayer domains at the air–water interface. Physics of Fluids 8 (4), 843.

Lucassen J 1968 Longitudinal capillary waves. Part 1. Theory. Trans. Faraday Soc 64, 2221–2229.

Lucassen J & Hansen RS 1966 Damping of waves on monolayer-covered surfaces I. Journal of Colloid and Interface Science 22 (1), 32–44.

Lucassen J & van den Tempel M 1972 Dynamic measurements of dilational properties of a liquid interface. Chemical Engineering Science 27 (6), 1283–1291.

Manikantan H & Squires TM 2017a Irreversible particle motion in surfactant-laden interfaces due to pressure-dependent surface viscosity. Proceedings of the Royal Society A: Mathematical, Physical and Engineering Science 473 (2205), 20170346.

Manikantan H & Squires TM 2017b Pressure-dependent surface viscosity and its surprising consequences in interfacial lubrication flows. Physical Review Fluids 2 (2), 023301.

Mann EK, Hénon S, Langevin D, Meunier J & Léger L 1995 Hydrodynamics of domain relaxation in a polymer monolayer. Physical Review E 51 (6), 5708–5720.

Marmottant P, van der Meer S, Emmer M, Versluis M, de Jong N, Hilgenfeldt S & Lohse D 2005 A model for large amplitude oscillations of coated bubbles accounting for buckling and rupture. The Journal of the Acoustical Society of America 118 (6), 3499.

Martínez-Balbuena L, Arteaga-Jiménez A, Hernández-Zapata E & Márquez-Beltrán C 2017 Applicability of the Gibbs adsorption isotherm to the analysis of experimental surface-tension data for ionic and nonionic surfactants. Advances in Colloid and Interface Science 247 (April), 178–184. [PubMed: 28780962]

McConnell HM 1991 Structures and transitions in lipid monolayers at the air-water interface. Annual Review of Physical Chemistry 42 (1), 171–195.

Mohwald H 1990 Phospholipid and phospholipid-protein monolayers at the air/water interface. Annual Review of Physical Chemistry 41 (1), 441–476.

Myers D 2006 Surfactant Science and Technology. John Wiley & Sons, Inc.

Oppenheimer N & Diamant H 2009 Correlated diffusion of membrane proteins and their effect on membrane viscosity. Biophysical Journal 96 (8), 3041–3049. [PubMed: 19383450]

Ou Ramdane O & Quéré D 1997 Thickening factor in Marangoni coating. Langmuir 13 (11), 2911–2916.

Park C-W 1991 Effects of insoluble surfactants on dip coating. Journal of Colloid and Interface Science 146 (2), 382–394.

Pozrikidis C 1992 Boundary Integral and Singularity Methods for Linearized Viscous Flow. Cambridge University Press.

Prasad V, Koehler SA & Weeks ER 2006 Two-particle microrheology of quasi-2D viscous systems. Physical Review Letters 97 (17), 176001. [PubMed: 17155483]

Probstein RF 1994 Physicochemical Hydrodynamics: An Introduction. John Wiley & Sons.

Quéré D 1999 Fluid coating on a fiber. Annual Review of Fluid Mechanics 31 (1), 347–384.

Raghunandan A, Hirsa AH, Underhill PT & Lopez JM 2018 Predicting steady shear rheology of condensed-phase monomolecular films at the air-water interface. Physical Review Letters 121 (16), 164502. [PubMed: 30387637]

Ravera F, Loglio G & Kovalchuk VI 2010 Interfacial dilational rheology by oscillating bubble/drop methods. Current Opinion in Colloid & Interface Science 15 (4), 217–228.

de Ruiter R, Tjerkstra RW, Duits MHG & Mugele F 2011 Influence of cationic composition and pH on the formation of metal stearates at oil-water interfaces. Langmuir 27 (14), 8738–8747. [PubMed: 21678925]

Sachan AK, Choi SQ, Kim KH, Tang Q, Hwang L, Lee KYC, Squires TM & Zasadzinski JA 2017 Interfacial rheology of coexisting solid and fluid monolayers. Soft Matter 13 (7), 1481–1492. [PubMed: 28125114]

Saffman PG 1976 Brownian motion in thin sheets of viscous fluid. Journal of Fluid Mechanics 73, 593.

Saffman PG & Delbrück M 1975 Brownian motion in biological membranes. Proceedings of the National Academy of Sciences 72 (8), 3111–3113.

Scheid B, Delacotte J, Dollet B, Rio E, Restagno F, van Nierop E. a., Cantat I, Langevin D & Stone H. a. 2010 The role of surface rheology in liquid film formation. EPL (Europhysics Letters) 90 (2), 24002.

Schwartz DK, Knobler CM & Bruinsma R 1994 Direct observation of Langmuir monolayer flow through a channel. Physical Review Letters 73 (21), 2841–2844. [PubMed: 10057209]

Scott JC 1982 Flow beneath a stagnant film on water: the Reynolds ridge. Journal of Fluid Mechanics 116, 283–296.

Scriven L 1960 Dynamics of a fluid interface: Equation of motion for Newtonian surface fluids. Chemical Engineering Science 12 (2), 98–108.

Scriven LE & Sternling CV 1960 The Marangoni effects. Nature 187 (4733), 186–188.

Seiwert J, Dollet B & Cantat I 2014 Theoretical study of the generation of soap films: role of interfacial visco-elasticity. Journal of Fluid Mechanics 739, 124–142.

Shen AQ, Gleason B, McKinley GH & Stone HA 2002 Fiber coating with surfactant solutions. Physics of Fluids 14 (11), 4055–4068.

Sickert M & Rondelez F 2003 Shear viscosity of langmuir monolayers in the low-density limit. Physical Review Letters 90 (12), 126104. [PubMed: 12688889]

Slattery JC, Sagis L & Oh E-S 2007 Interfacial transport phenomena. Springer.

Squires TM & Quake S 2005 Microfluidics: Fluid physics at the nanoliter scale. Reviews of Modern Physics 77 (July), 977–1026.

Stancik EJ, Kouhkan M & Fuller GG 2004 Coalescence of particle-laden fluid interfaces. Langmuir 20 (1), 90–94. [PubMed: 15745004]

Stebe KJ, Lin S-Y & Maldarelli C 1991 Remobilizing surfactant retarded fluid particle interfaces. I. Stress-free conditions at the interfaces of micellar solutions of surfactants with fast sorption kinetics. Physics of Fluids A: Fluid Dynamics 3 (1), 3–20.

Stebe KJ & Maldarelli C 1994 Remobilizing surfactant retarded fluid particle interfaces. Journal of Colloid and Interface Science 163 (1), 177–189.

Stevenson P 2005 Remarks on the shear viscosity of surfaces stabilised with soluble surfactants. Journal of Colloid and Interface Science 290 (2), 603–606. [PubMed: 16112130]

Stickel JJ & Powell RL 2005 Fluid mechanics and rheology of dense suspensions. Annual Review of Fluid Mechanics 37 (1), 129–149.

Stone HA 1990 A simple derivation of the time-dependent convective-diffusion equation for surfactant transport along a deforming interface. *Physics of Fluids A*: Fluid Dynamics 2 (1), 111–112.

Stone HA 1995 Fluid Motion of Monomolecular Films in a Channel Flow Geometry. Phys Fluids 7 (12), 2931–2937.

Stone HA & Ajdari A 1998 Hydrodynamics of particles embedded in a flat surfactant layer overlying a subphase of finite depth. Journal of Fluid Mechanics 369 (1), 151–173.

Stone HA & Masoud H 2015 Mobility of membrane-trapped particles. Journal of Fluid Mechanics 781, 494–505.

Trabelsi S, Zhang S, Lee TR & Schwartz DK 2008 Linactants: Surfactant analogues in two dimensions. Physical Review Letters 100 (3), 037802. [PubMed: 18233038]

Troian SM, Herbolzheimer E & Safran SA 1990 Model for the fingering instability of spreading surfactant drops. Physical Review Letters 65 (3), 333–336. [PubMed: 10042892]

Verbist G, Weaire D & Kraynik AM 1996 The foam drainage equation. Journal of Physics: Condensed Matter 8 (21), 3715–3731.

Verwijlen T, Leiske DL, Moldenaers P, Vermant J & Fuller GG 2012 Extensional rheometry at interfaces: Analysis of the cambridge interfacial tensiometer. Journal of Rheology 56 (5), 1225.

Verwijlen T, Moldenaers P, Stone HA & Vermant J 2011 Study of the flow field in the magnetic rod interfacial stress rheometer. Langmuir 27 (15), 9345–9358. [PubMed: 21696160]

Ward AFH & Tordai L 1946 Time-dependence of boundary tensions of solutions. I. The role of diffusion in time-effects. The Journal of Chemical Physics 14 (7), 453–461.

Zell ZA, Nowbahar A, Mansard V, Leal LG, Deshmukh SS, Mecca JM, Tucker CJ & Squires TM 2014 Surface shear inviscidity of soluble surfactants. Proceedings of the National Academy of Sciences 111 (10), 3677–3682.

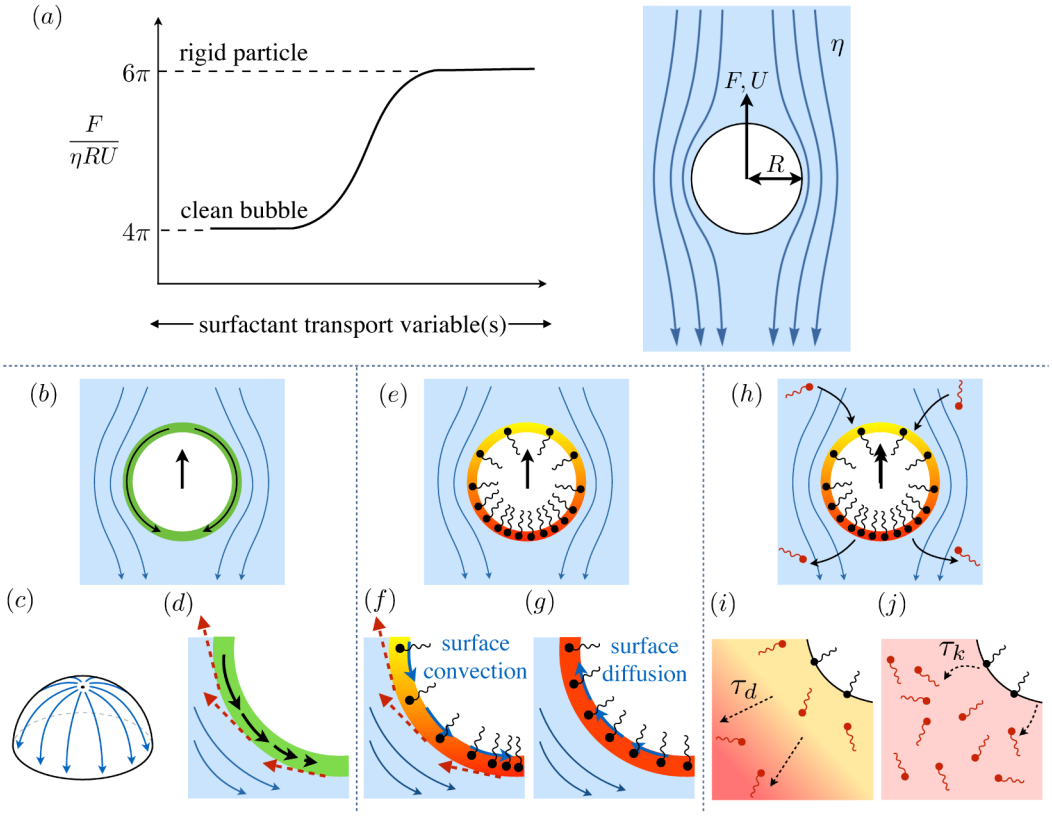

Figure 1.

(*a*) 'Hidden' surfactant variables modify the interfacial flow of a rising bubble such that it might behave like a clean drop, a rigid particle, or somewhere in between. The associated surfactant transport processes are not often easy to differentiate, and systems may exhibit one or a non-trivial combination of several processes. (*b*)–(*d*) For instance, an interfacial or surface excess viscosity can resist the surface flow. The solid lines depict surface flow, and dashed red arrows indicate tangential (viscous) stresses resisting deformation. (*e*)–(*g*) Alternatively, surfactants swept to the rear of the bubble build a concentration gradient and generate a counter-acting Marangoni stress (dashed red arrows) that resists surface convection (blue arrows). These Marangoni forces may be weakened by surface diffusion against the gradient. (*h*)–(*j*) If the surfactant is soluble, adsorption/desorption from the bulk can drive the surface concentration back to equilibrium over a finite time. This process might be controlled by (*i*) diffusive transport in the bulk across bulk concentration gradients over a timescale τ_d, or by (*j*) the finite-rate kinetics over a finite timescale τ_k.

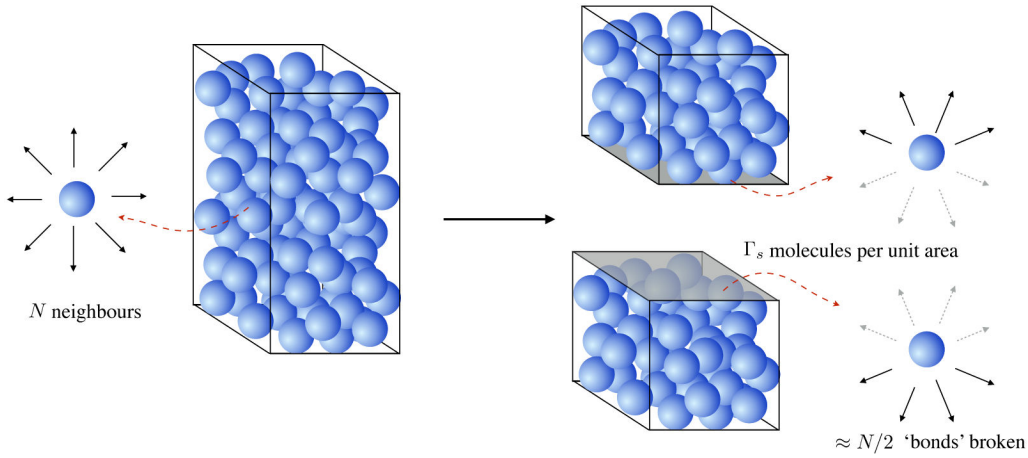

Figure 2.

A liquid molecule in the bulk of a fluid experiences no net force due to a (time-averaged) symmetric distribution of neighhbors. Creating an interface, however, requires breaking intermolecular 'bonds' on the interface and is energentically expensive.

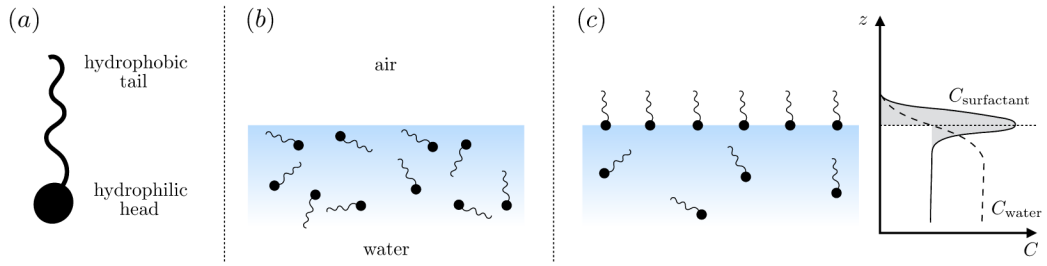

Figure 3.

(*a*) Schematic representation of an amphiphilic molecule. (*b*)–(*c*) Surfactant molecules adsorb to the interface to an extent determined by the competition between (loss of) entropy and energetically favorable interactions during adsorption. Also shown in (*c*) are the concentration profiles of surfactant (solid line) and water (dashed line) molecules. The 'excess' surface concentration is in gray, which represents the amount of surfactant in excess of a hypothetical state where the concentration of dissolved surfactant is constant up until the surface.

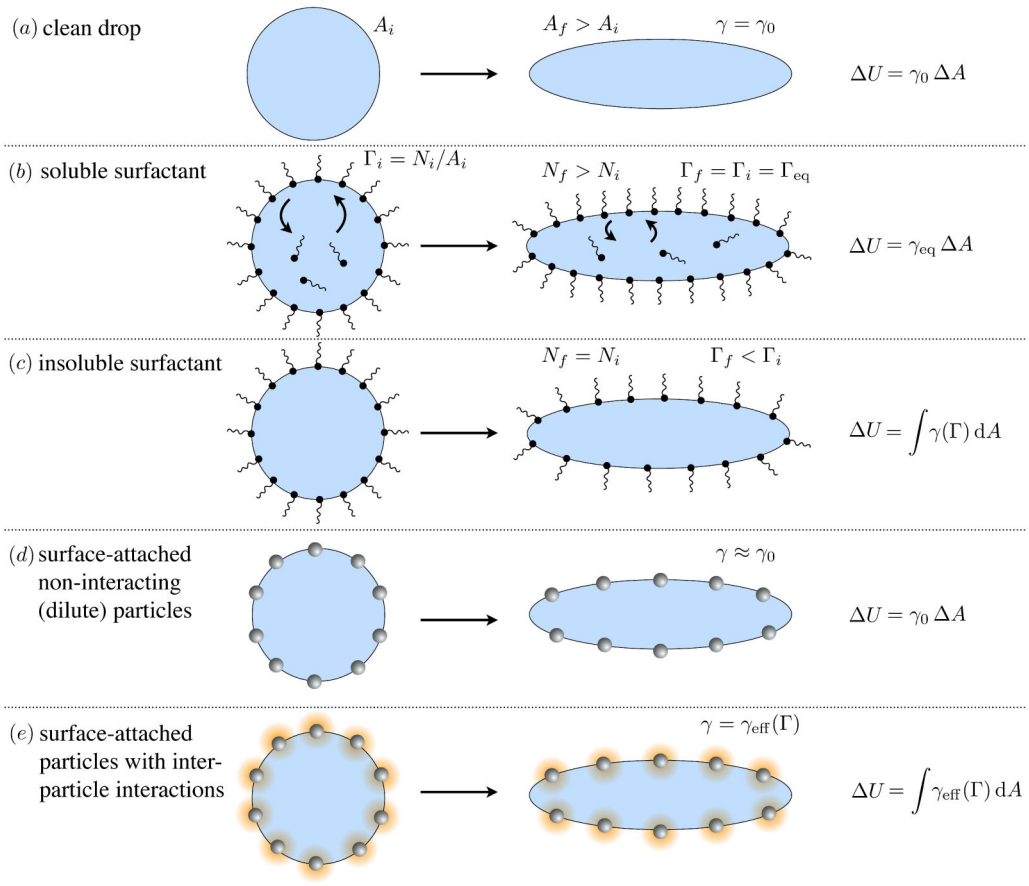

Figure 4.
Examples of change in surface energy upon deformation of a drop with surface-active molecules or particles.

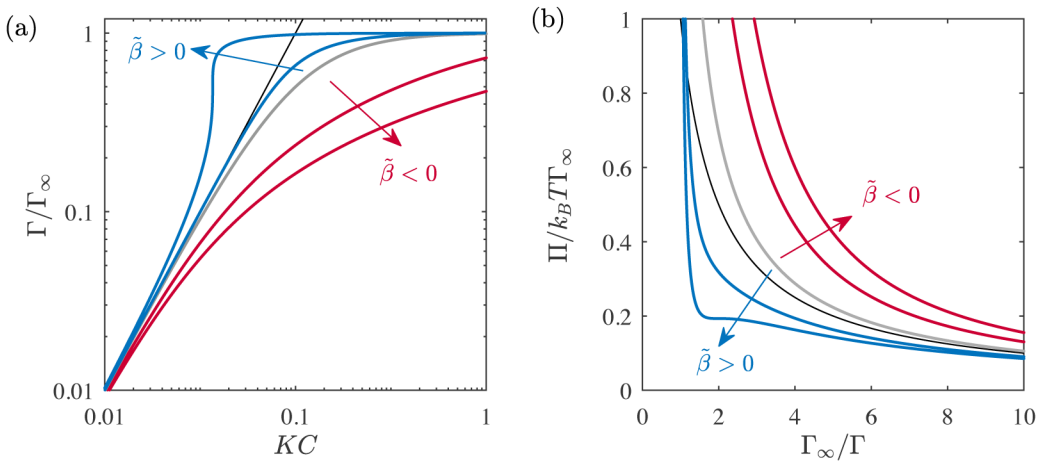

Figure 5.

(*a*) $\Gamma(C)$ and (*b*) $\Pi(\Gamma)$ relations corresponding to Frumkin adsorption from an ideal subphase. Intermolecular interactions are attractive when $\tilde{\beta} = \beta\Gamma_\infty/k_BT > 0$ (blue lines), and repulsive when $\tilde{\beta} < 0$ (red lines). $\tilde{\beta} = 0$ (gray solid lines) recovers Langmuir adsorption. The black line in each panel is the 2D ideal gas limit (the Henry isotherm).

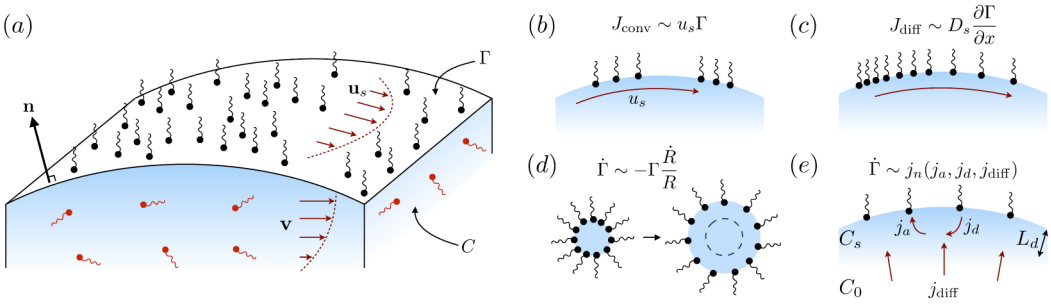

Figure 6.

(*a*) Geometry of a typical surfactant-laden interface. (*b*)–(*e*) Mass transport processes on the interface: (*b*) convection due to imposed (or Marangoni) velocity u_s; (*c*) diffusion due to a surface concentration gradient; (*d*) surface concentration evolution due to curvature modification; and (*e*) adsorption/desorption from the sublayer, showing the depletion length L_d.

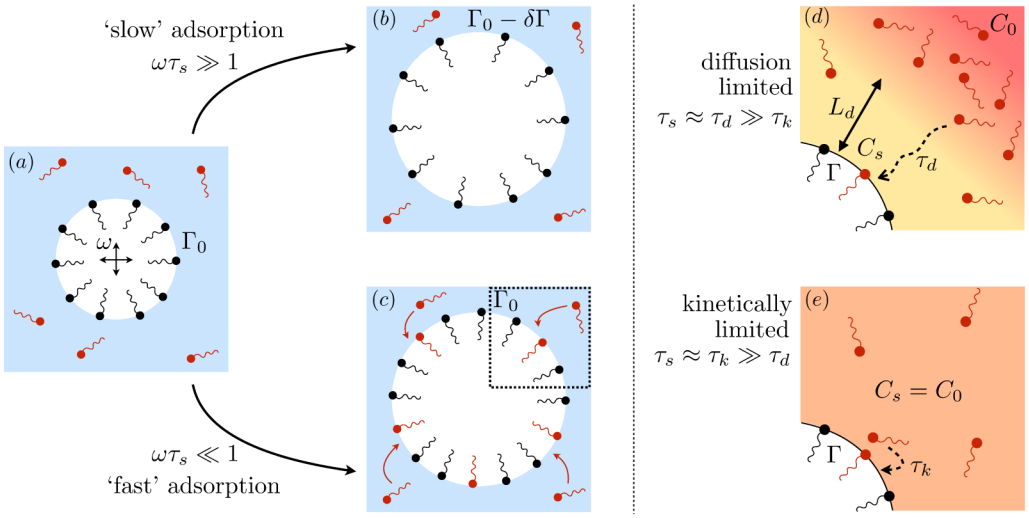

Figure 7.

(*a*) A surfactant-covered bubble oscillating in a liquid containing dissolved surfactant. (*b*) If surfactant exchange is negligibly slow, the number of adsorbed molecules is unchanged (or the surface concentration changes by $\delta\Gamma$). (*c*) By contrast, rapid surfactant exchange equilibrates the surface so that $\Gamma(t) \approx \Gamma_0$ and $\delta\Gamma \approx 0$. Surfactant exchange can be (*d*) diffusion-controlled or (*e*) kinetically-controlled if either process is rate-limiting.

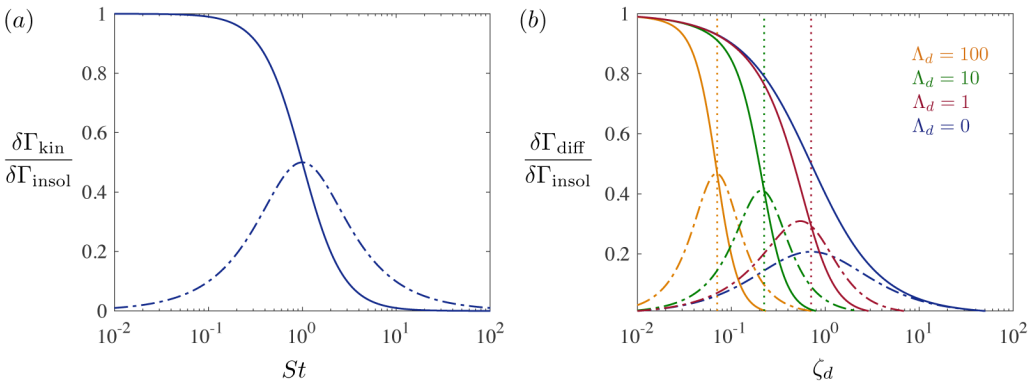

Figure 8.

(*a*) Real (solid line) and imaginary (broken line) components of the perturbed surface concentration for kinetically-limited adsorption ($Da \to 0$) to an oscillating bubble, from (3.44). (*b*) Surface concentration in diffusion-limited mass transfer ($Da \to \infty$), from (3.50). $\Lambda_d = 0$ represents a planar interface following (3.48). The vertical dashed lines show locations where $2\Lambda_d\zeta_d^2 = 1$ when $\Lambda_d \gtrsim 1$, indicating modified diffusion times for small bubbles via (3.53).

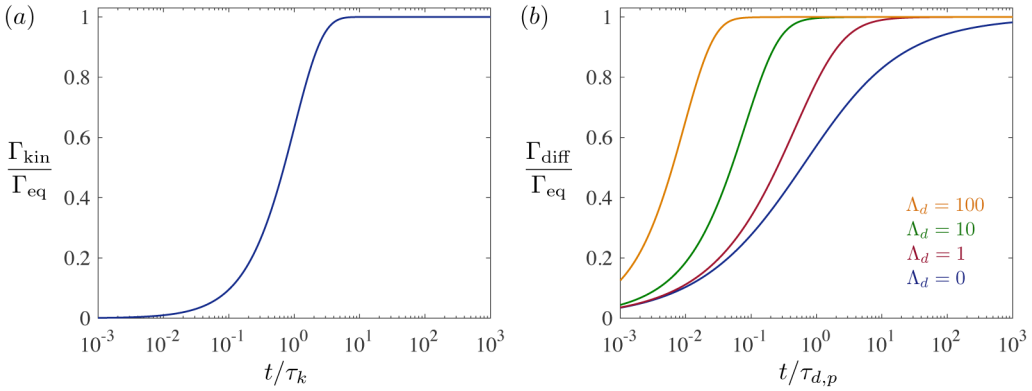

Figure 9.

(*a*) Kinetically-controlled adsorption (3.68) to an initially clean spherical surface. (*b*) Diffusion-controlled adsorption (3.71) to a spherical surface. Adsorption occurs over a faster time scale $\tau_{d,s}$ in smaller bubbles ($\Lambda_d = L_d/R \gtrsim 1$), and approaches equilibrium exponentially, rather than as $1/\sqrt{t}$ in the case of large bubbles ($\Lambda_d \to 0$).

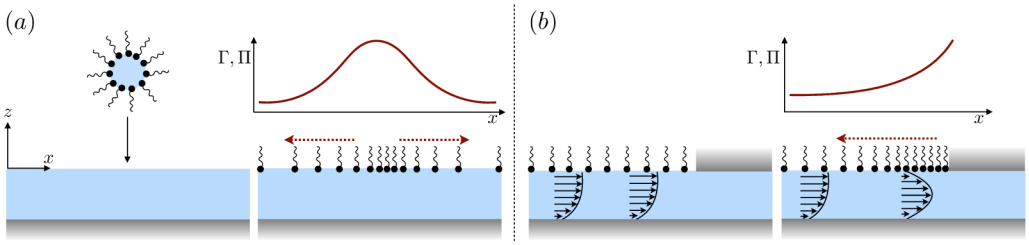

Figure 10.

Two conjugate effects commonly termed ‘Marangoni’ effects: (*a*) A local increase in surfactant concentration, shown here by the addition of a surfactant-rich drop, establishes a surface concentration gradient (and, therefore, a surface pressure gradient) that drives an outward surface flow (red arrows). (*b*) Surface compression due to flow (in this case, towards an interfacial barrier) establishes a surface tension gradient due to non-uniform surface concentration. This introduces a reverse Marangoni flow that ‘immoblizes’ the surface.

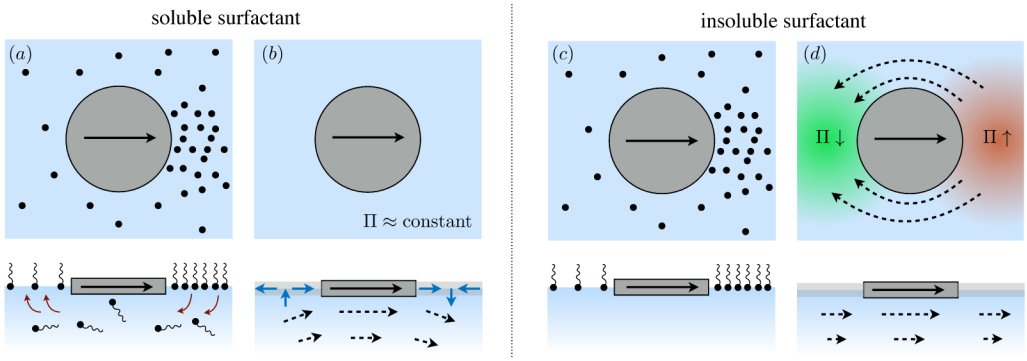

Figure 11.

Illustration of surfactant-induced incompressibility. (*a*) Motion of a probe establishes a surface concentration gradient, shown in top and side views. In a soluble monolayer with instantaneous adsorption/desorption, surface concentration gradients are rapidly eliminated. (*b*) In this limit, $\Delta\Pi \approx 0$ and reverse Marangoni flows are absent. The surface flow has a non-zero divergence ahead and behind the disk. Bulk fluid flow is indicated by the dashed arrows and is indistinguishable from that corresponding to a stress-free clean interface. (*c*) By contrast, if the surfactant is insoluble, a surface concentration gradient is sustained, and (*d*) the surface pressure difference $\Delta\Pi$ generates a reverse Marangoni flow that resists interfacial compression/dilatation. The modified surface flow is divergence-free, which changes the bulk flow by constraining it to flow in planes parallel to the interface (see discussion).

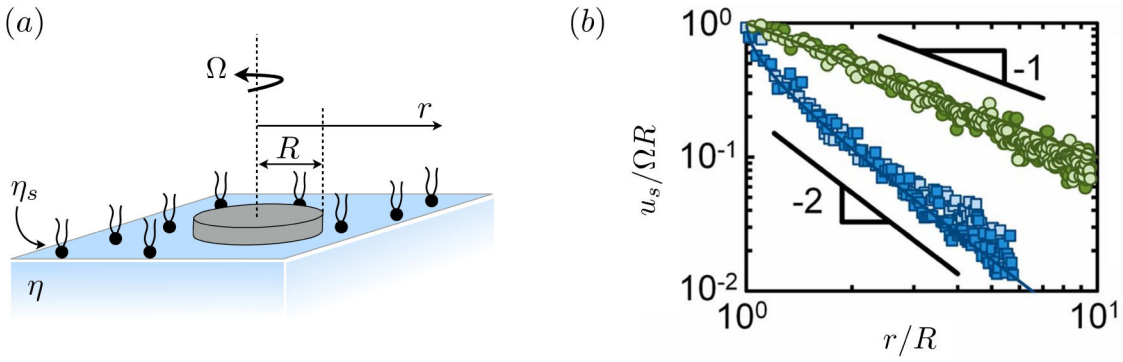

Figure 12.

(*a*) A disk of radius R rotating at a constant angular velocity Ω within a monolayer of surface shear viscosity η_s. (*b*) Surface velocity u_s follows (3.100) when subphase-dominant ($Bq \ll 1$, blue squares) and (3.101) when interface-dominant ($Bq \gg 1$, green circles); adapted from Zell *et al.* (2014).

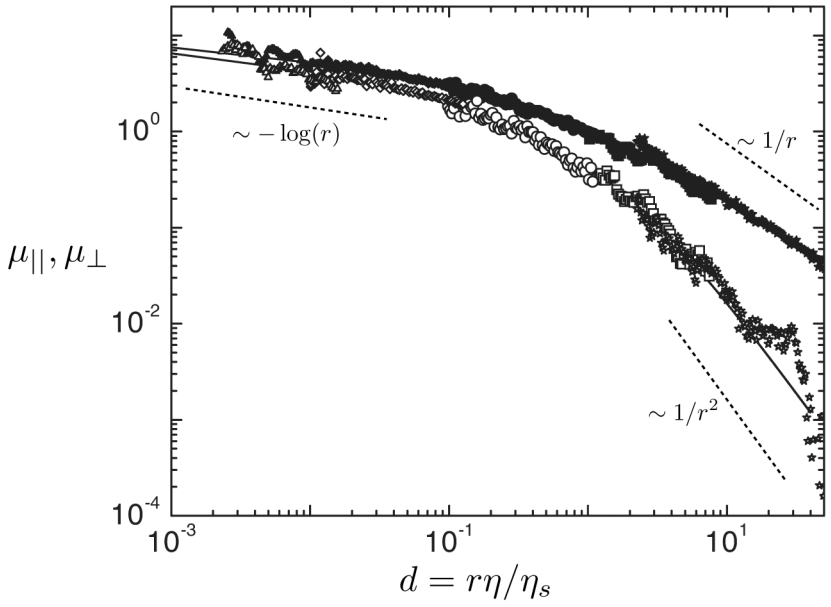

Figure 13.

Mobility coefficients in the radial ($\mu_\parallel$) and azimuthal ($\mu_\perp$) directions (in arbitrary units) extracted from two-particle microrheology. In the surface-dominated regime ($Bq \gg 1$ or $d \ll 1$), both coefficients decay logarithmically with distance, following (3.112). In subphase-dominated cases ($Bq \gg 1$ or $d \ll 1$), the coefficients decay as $1/r$ and $1/r^2$. The symbols correspond to two-particle displacement correlations along the line of centers (filled symbols) and perpendicular to it (empty symbols), and the solid lines are fits to (3.109). The shapes of the symbols correspond to different surface viscosities. Adapted from Prasad *et al.* (2006).

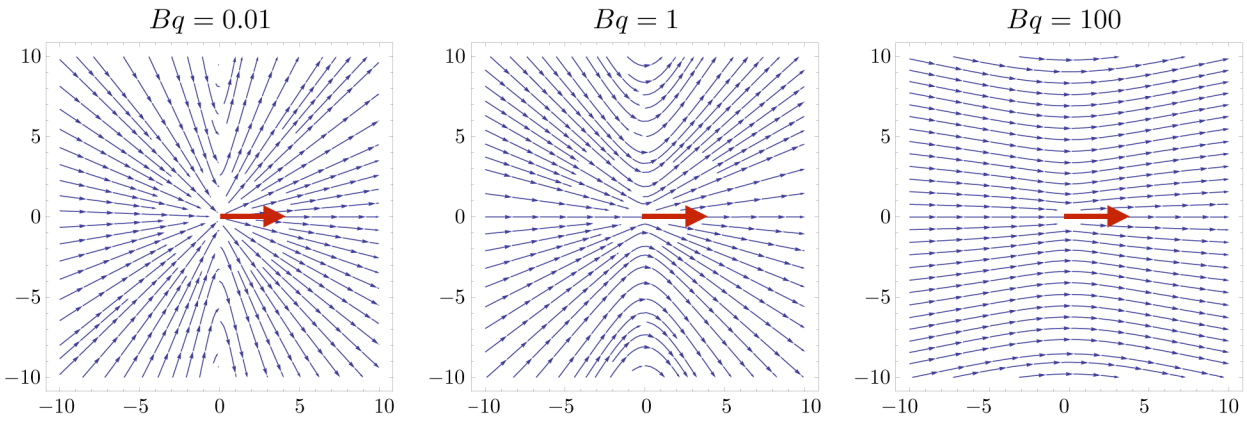

Figure 14.

Streamlines of surface velocity as a result of a point force applied at the origin, following (3.108). Length is in units of R such that $Bq = \eta_s/\eta R$.

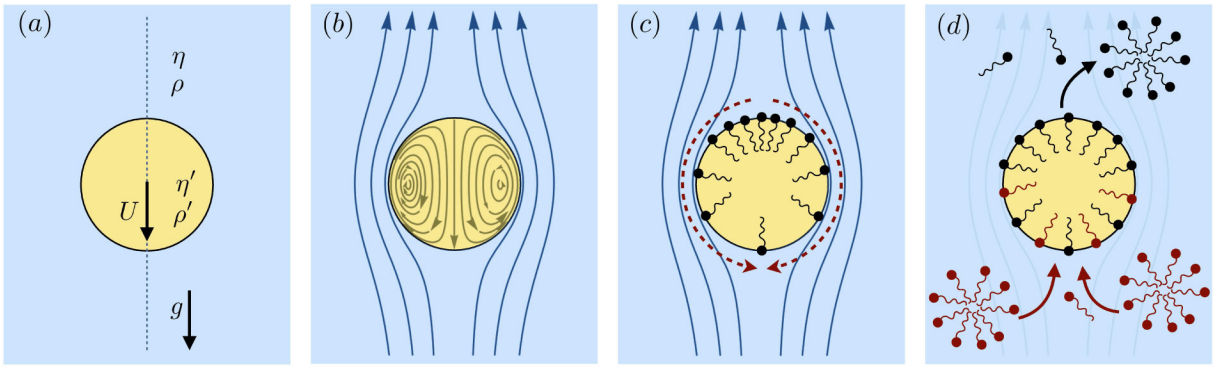

Figure 15.

(*a*) A drop settling in a viscous fluid with terminal velocity U, and (*b*) streamlines corresponding to the Hadamard-Rybczynski solution for a clean interface. (*c*) The uniform retardation regime: with adsorption-desorption or diffusion over finite time scales, a surface concentration gradient is established, and a reverse Marangoni flow immobilizes the surface. (*d*) The remobilization regime: molecules freely desorb at the downstream pole and adsorb at the upstream pole if τ_s is small and bulk concentration is above CMC. The resulting near-uniform surface concentration suppresses Marangoni flows and remobilizes the interface.

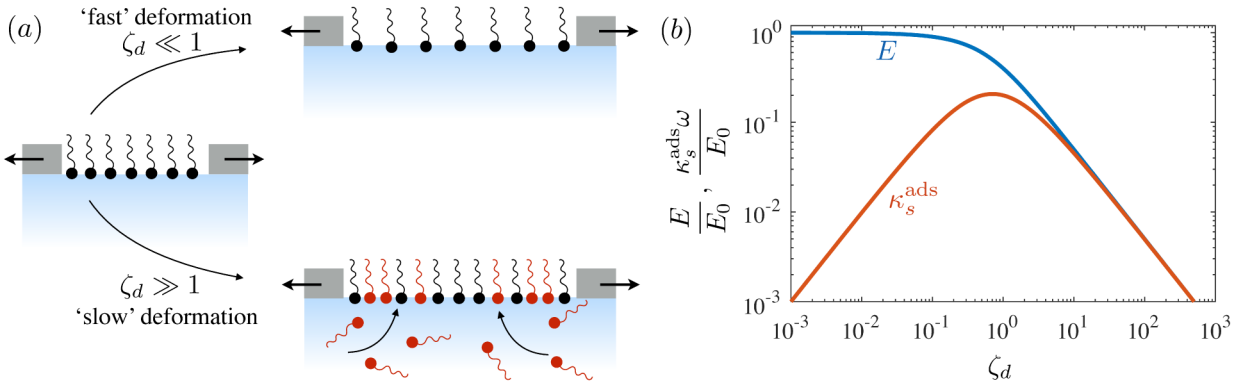

Figure 16.

(*a*) Response of a surfactant monolayer to a dilatational deformation that is fast or slow relative to rate of replenishment by adsorption from the bulk. The monolayer is effectively insoluble as $\zeta_d \to 0$, and the elastic modulus is highest (= E^0) in this limit. Conversely, perturbations of surface concentration from equilibrium are rapidly eliminated by adsorption and the surface elasticity is weak when $\zeta_d \gg 1$. (*b*) The dynamic Gibbs modulus E and apparent dilatational surface viscosity κ_s^{ads} from (4.34).

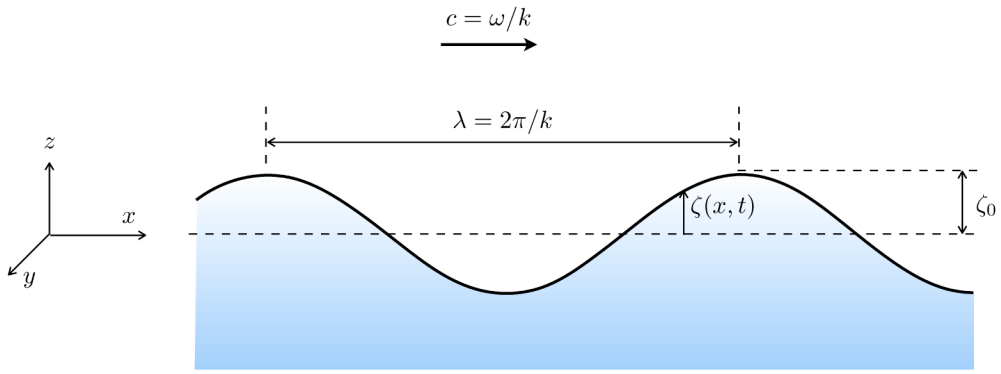

Figure 17.
A planar wave of amplitude ζ_0, length λ and frequency ω.

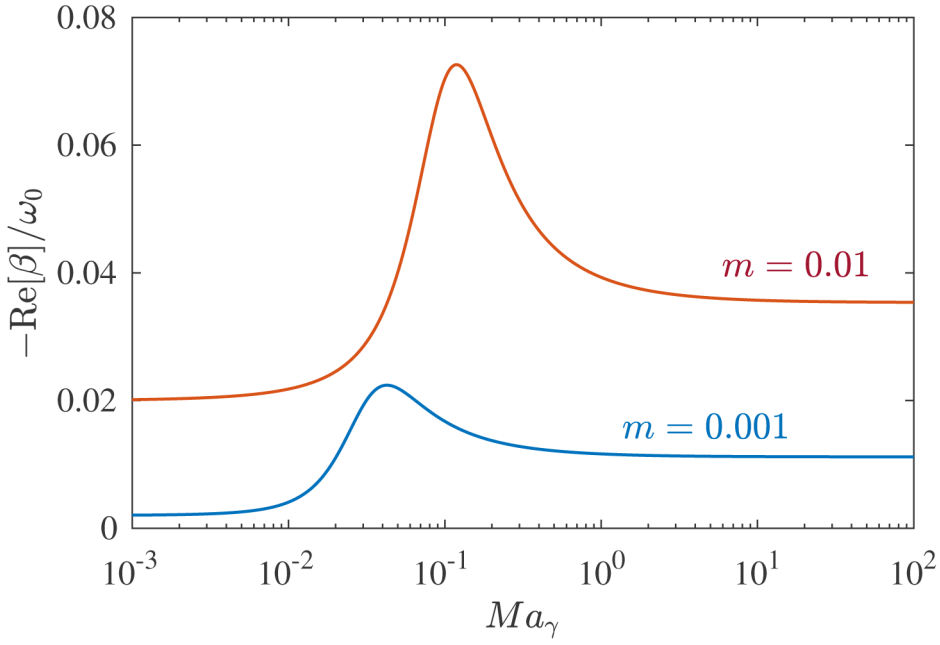

Figure 18.

Capillary wave damping rate β (4.71) as a function of the Marangoni number $Ma_\gamma = E_0/\gamma$ and the normalized fluid viscosity $m = \nu k^2/\omega_0$. The damping rate asymptotes to $\beta_{\text{clean}} = -2m\omega_0$ when Marangoni flows are weak ($Ma_\gamma \ll 1$) and to $\beta_{\text{stiff}} = -(\omega_0/2)\sqrt{m/2}$ when the interface is immobilized ($Ma_\gamma \gg 1$). Waves decay faster in a more viscous fluid (larger m) for all Ma_γ.

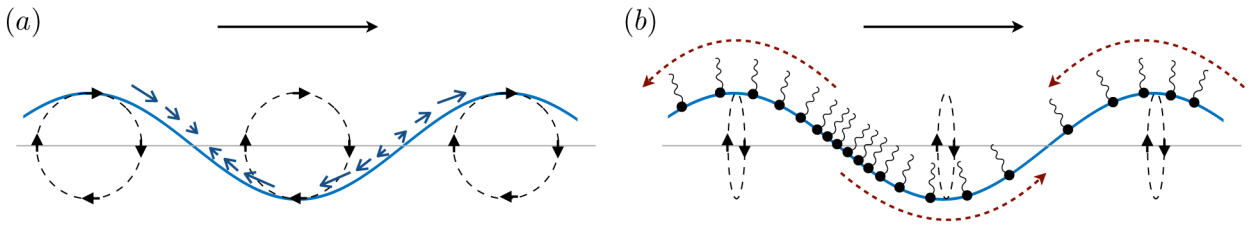

Figure 19.

(*a*) Circular motion of interfacial fluid particles on the clean surface of a wave moving to the right. The solid blue arrows along the interface depict compression and expansion of the surface. (*b*) Surfactants distort circular trajectories via Marangoni flows (red dashed arrows) that oppose the compression and expansion of the interface. The trajectories of fluid elements are then distorted, becoming straight lines in the $Ma_\gamma \to \infty$ limit.

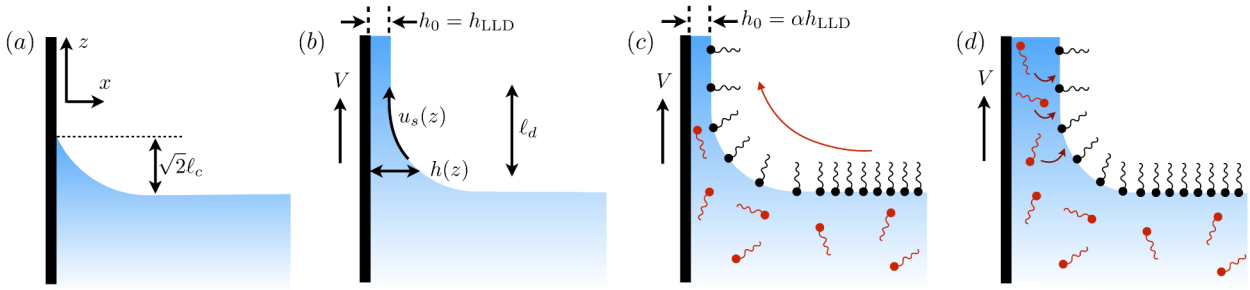

Figure 20.

(*a*) A static meniscus form next to a stationary wall and the liquid level rises to a height $\sqrt{2}\ell_c$. (*b*) When the wall is drawn upward, a film of liquid of asymptotic thickness h_0 is entrained, and a dynamic meniscus connects the coating with the liquid reservoir. When the surface is clean, the the LLD scaling gives $h_0 \sim Ca^{2/3}\ell_c$. (*c*) When surfactants occupy the liquid-air interface, Marangoni effects (and/or surface viscosity, see discussion) resist surface dilatation, drawing more fluid along with the moving plate. The coating is thicker by the factor α. (*d*) If the entrained film is thick enough, or if bulk concentration is large enough, surface concentration gradients are suppressed by adsorption of surfactant molecules to the interface, weakening the Marangoni effect.

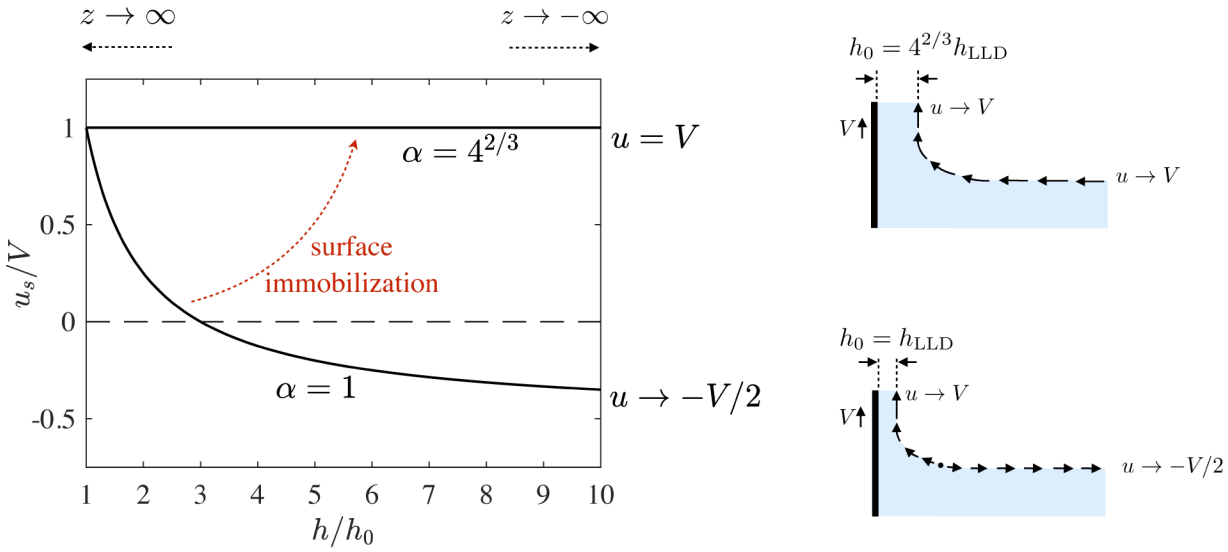

Figure 21.

Surface velocity of the entrained film. The surface flow has a stagnation point for a clean interface ($\alpha = 1$) beyond which the fluid flow is in the direction opposite to that of the plate. With increasing α, the surface is immobilised until a maximal value of $\alpha = 4^{2/3}$, when the interface is surface incompressible and is drawn at the same velocity as the plate everywhere.

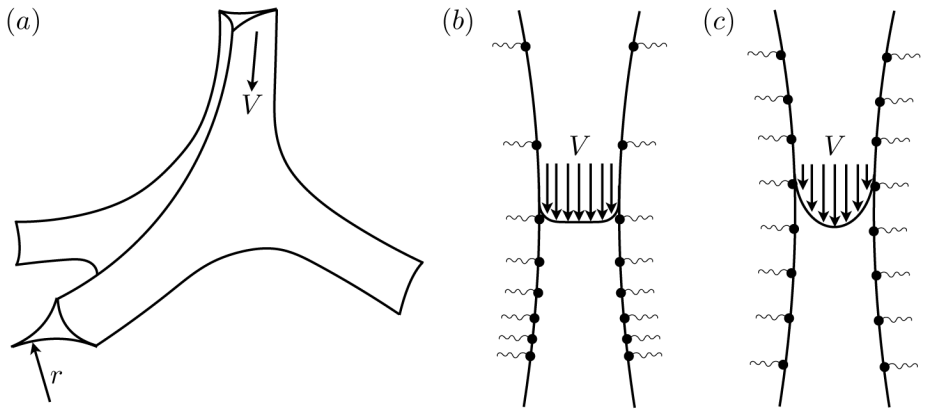

Figure 22.

(*a*) Geometry of a node at the intersection of four Plateau borders. (*b*) Flow along a longitudinal section of a channel is plug-like when $Bq \ll 1$. Viscous dissipation occurs primarily at the nodes (not shown) in this case. (*c*) Poiseuille flow for $Bq \gg 1$, corresponding to large interfacial stresses and subsequent surface immobilization.

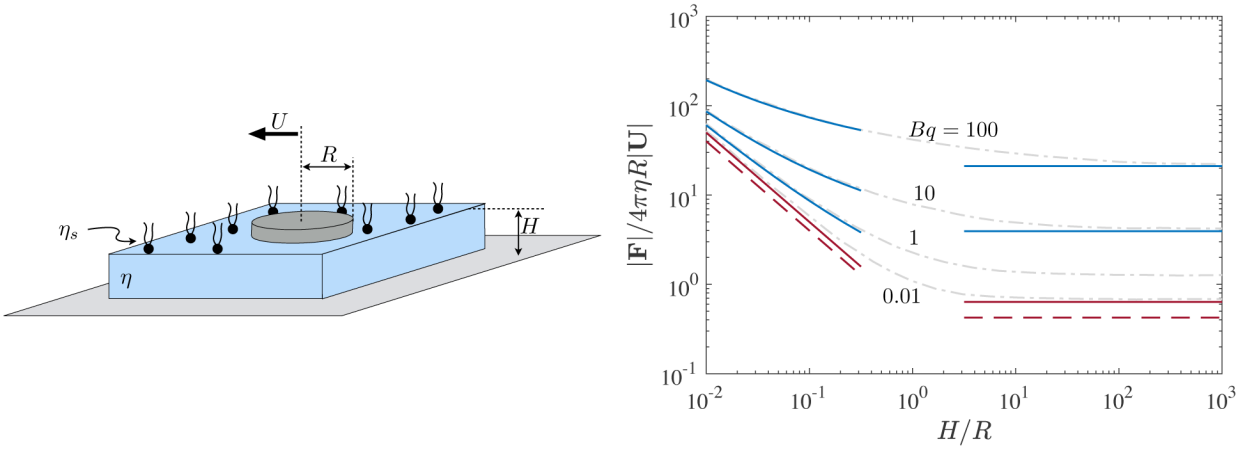

Figure 23.

A cylindrical disk translating within an insoluble surfactant monolayer atop a bulk fluid layer of finite depth H. Also shown is the resistance coefficient $|\boldsymbol{F}|/4\pi\eta R|\boldsymbol{U}|$ as a function of both sublayer thickness and Boussinesq number. The gray dash-dot lines are the numerical calculations of Stone & Ajdari (1998) at specified Bq, and the solid lines are asymptotic values for small and large H/R. The bottom-most solid lines represent the $Bq \to 0$ limit (table 4). The dashed asymptotes correspond to a clean interface, from (4.158) and (4.162), and highlights the fact that even an inviscid surfactant increases drag on a translating probe as compared to a surfactant-free surface.

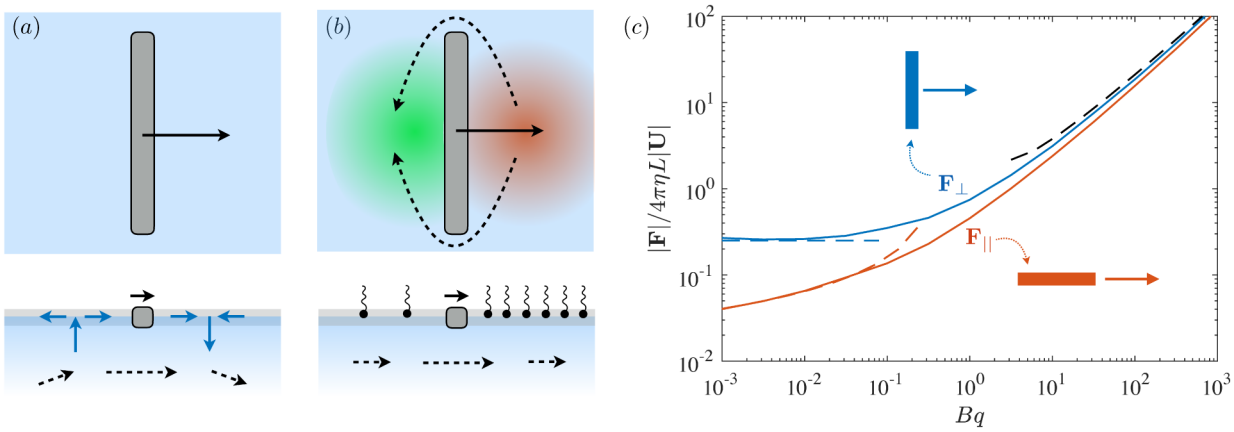

Figure 24.

(*a*) A rod translating perpendicular to its long axis on a clean interface, shown in top and side views. The surface velocity field has a non-zero divergence ahead and behind the rod, and the bulk velocity field is three-dimensional. (*b*) Insoluble surfactants drive reverse Marangoni flows that render monolayers incompressible (see §3.3.2 and figure 11), setting up surface and bulk flows on length scales comparable to the rod length. Surface incompressibility thus imparts a larger drag than a clean interface even when the surfactant is surface-inviscid ($Bq \to 0$), and impacts $\boldsymbol{F}_\perp$ more strongly than $\boldsymbol{F}_\parallel$.· (*c*) Translational resistance coefficient of long rods in incompressible monolayers (Levine *et al.* 2004) with asymptotic scalings in dashed lines following (4.168), (4.169), and (4.170).

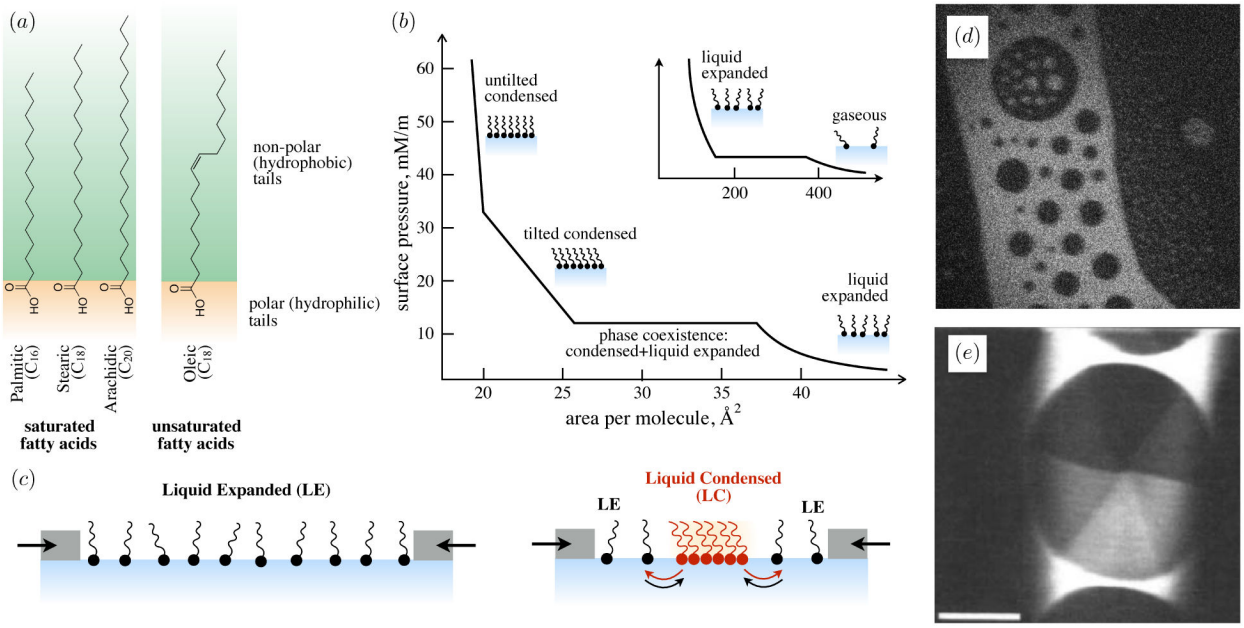

Figure 25.

(*a*) Fatty acids consist of a (hydrophilic) carboxilic acid head group and a (hydrophobic) hydrocarbon tail. The longer the hydrocarbon tail, the lower its solubility in water and the stronger the van der Waals attractions with adjacent fatty acids. Saturated hydrocarbon tails pack well with each other, whereas unsaturated tails (e.g. oleic acid, with a double bond at the ninth carbon) are ‘kinked’ and frustrate packing. (b) Generalized isotherm of an insoluble monolayer of saturated fatty acids, adapted from Kaganer *et al.* (1999). Monolayers form a gaseous phase at extremely low concentration (inset), which condenses to form a disordered, liquid expanded (LE) phase when compressed. At higher surface concentrations, a phase transition occurs from the LE phase to one of various liquid condensed (LC) phases with different liquid crystalline order, and even further phase transitions at higher concentrations (here to an untilted, condensed phase). (c) Cartoon showing transition between a disordered, low-density phase (e.g. LE or gaseous) to phase coexistence with a higher-density phase (e.g. LE/LC or gas/LE). (d) Fluorescence micrograph showing gas/LE phase coexistence of the phospholipid DPPC (courtesy of Dr. Ian Williams). (e) Polarized micrograph of LE-LC phase coexistence between methyl eicosanoate(C_{20}). Within the LC domain, the six different brightness levels correspond to six distinct orientations of the packed tails, which in turn reveal the hexagonal headgroup lattice (from Knobler & Desai (1992)).

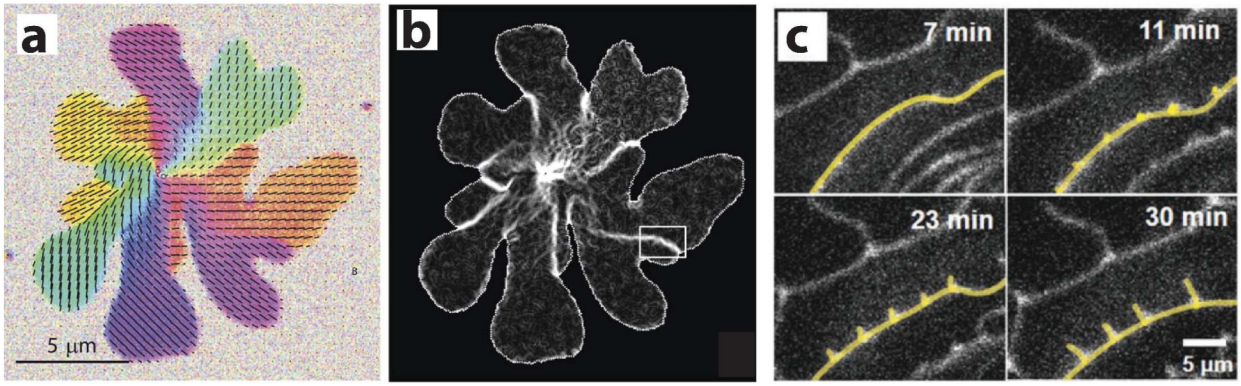

Figure 26.

(a) Tilted DPPC tail groups within an LC domain form discrete patches, within which tails are oriented in the same direction. The tilt orientation jumps by 60° from patch to patch, to accomodate the frustration between the tendency of tilt orientation to precess and the tendency of the hegaxonal headgroup lattice to maintain its order. (b) Bright lines indicate boundaries between patches of aligned tilt, across which tailgroup orientation abruptly changes. These high-energy lines exert a line tension internal to the drop, effectively 'pulling' in invaginations at the domain boundary. (a–b) reproduced from Dreier *et al.* (2012). (c) New tilt grain boundary lines form and grow in LC DPPC domain arms that had been stretched significantly. From Kim *et al.* (2018).

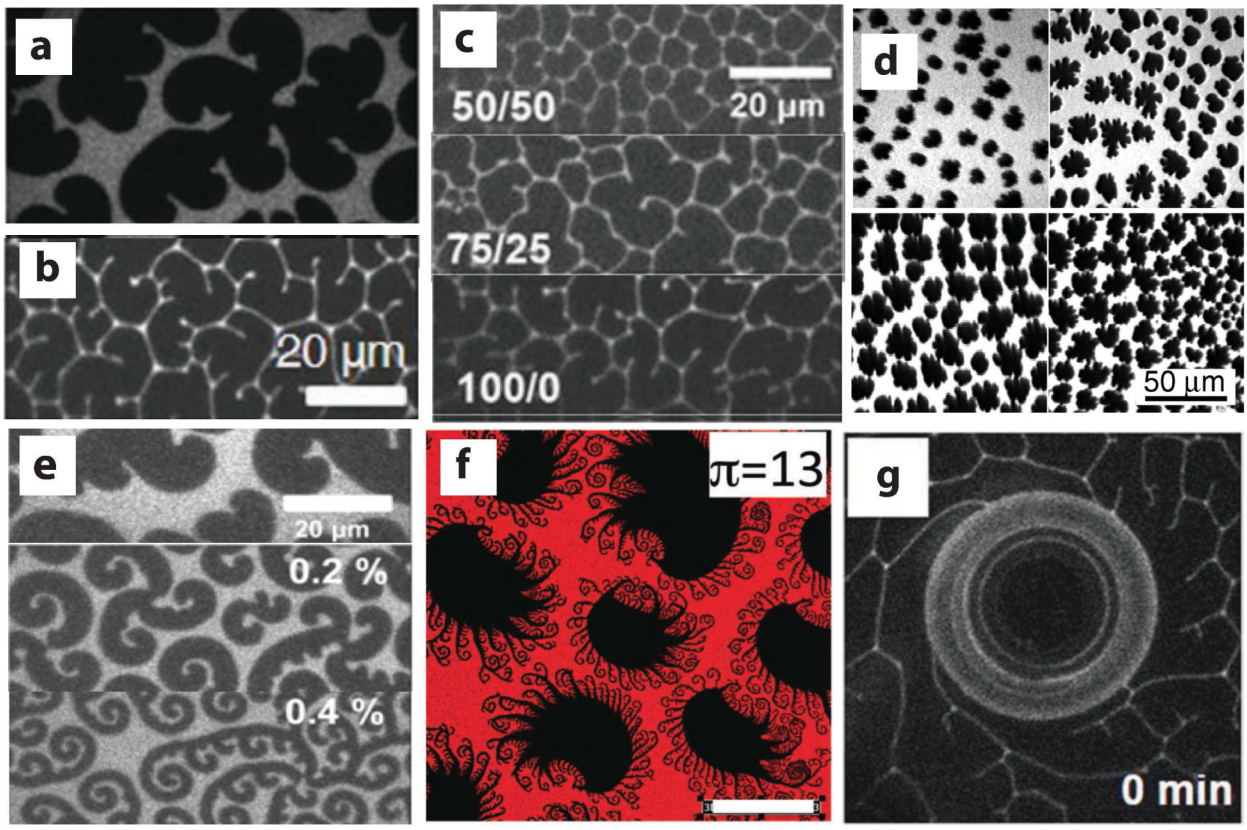

Figure 27.

(a-b) The phospholipid Dipalmitoylphostphatidylcholine (DPPC) in (a) LC/LE coexistence and (b) polycrystalline, fully LC phase, from Kim *et al.* (2018). Natural DPPC forms LC domains that wind in a counter-clockwise fashion, owing to the chiral attachment of the two hydrocarbon tails. (c) The chirality of domains within an LC DPPC monolayer depends on the ratio of right- to left-handed DPPC molecules (from Kim *et al.* (2018)). (d) Palmitic acid co-crystallizes with DPPC to form stiff inclusions, here dispersed by a disordered phase of the unsaturated lipid POPG (from Ding *et al.* (2002)).(e) Cholesterol is 'line-active' for DPPC, promoting the growth of thinner LC grains that wind more tightly (from Kim *et al.* (2013)). (f) DPPC/hexadecanol/cholesterol mixtures form eerily beautiful grains in LC/LE coexistence, consisting of a DPPC/HD co-crystallized core, surrounded by wispy, spiraling DPPC/cholesterol arms (from Sachan *et al.* (2017)). (f) An LC-DPPC monolayer that is steadily deformed by a rotating microfabricated 'button', reveals a surface yield stress: the monolayer flows within the high-stress region near the button, but is stationary outside a yield radius (from Kim *et al.* (2018).

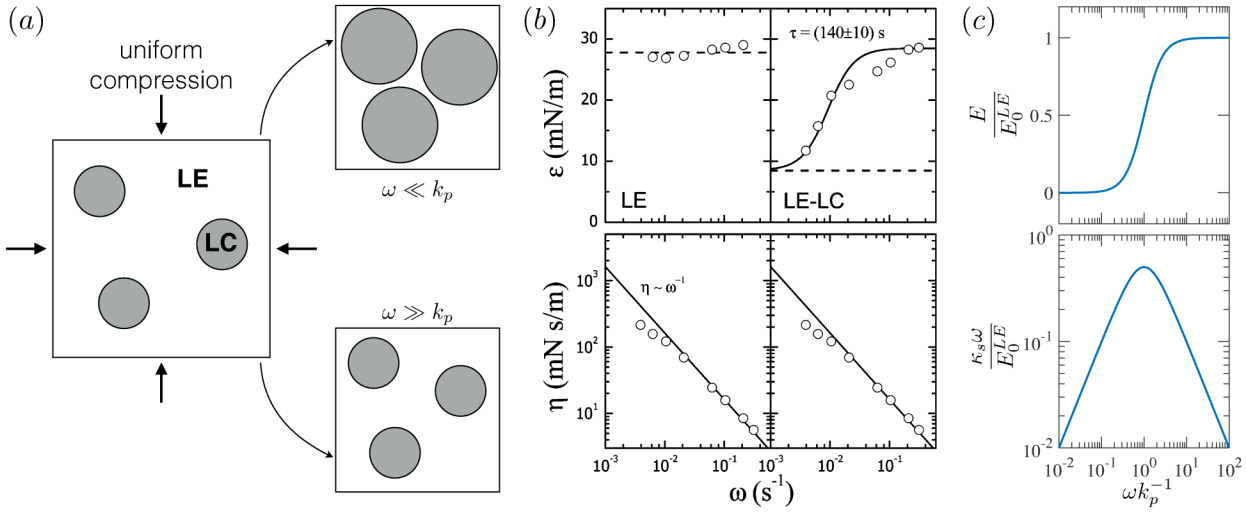

Figure 28.

(*a*) Response of a monolayer with coexisting phases to uniform compression: when $\omega \ll k_p$, domains grow much faster than the rate of compression, and the LE phase offers no elastic resistance. By contrast, when $\omega \gg k_p$, the rate of compression exceeds the rate of molecules changing phases, and the LE phase offers a net resistance to compression. (*b*) Measurements of Arriaga *et al.* (2010) showing elastic and viscous moduli from oscillatory measurements in LE and in coexistence. The solid lines are fit to a Maxwell viscoelastic fluid with characteristic relaxation time $\tau = k_p^{-1} \approx 140\,\mathrm{s}$, and the dashed lines are slopes from equilibrium ($\omega \to 0$) isotherms. (*c*) Effective elastic and viscous modulus following (5.16).

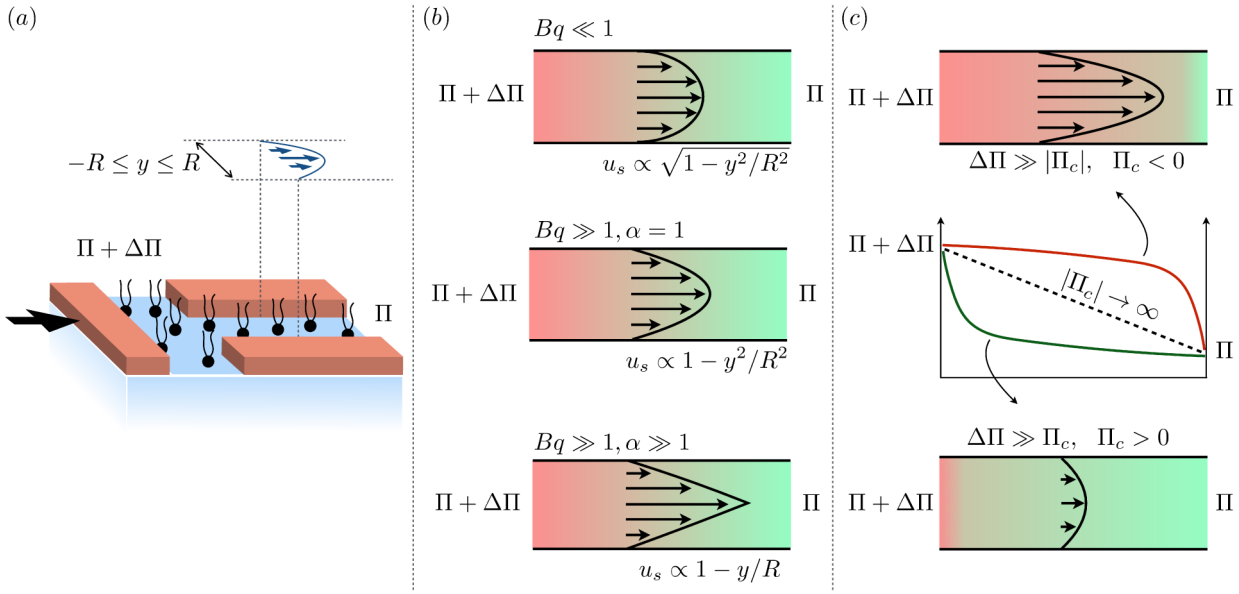

Figure 29.

(*a*) A surface pressure gradient across an interfacial channel sets up a surface (and bulk) flow, much pressure-driven flow in 3D. (*b*) Illustrations of surface velocity profiles, with α defined in (5.19): $u_s(y)$ is elliptic when subphase-dominant ($Bq \ll 1$) and parabolic when interface-dominant ($Bq \gg 1$) with Newtonian surface rheology. However, condensed arachidic acid above $\Pi \sim 20$ mN/m surface-shear-thickens, resulting in triangular velocity profiles (5.19). The background color gradient represents $\Pi(x)$, which changes linearly across the length of the channel. (*c*) Surface pressure distribution in the channel is nonlinear when η_s is a function of Π. When Π-thinning, surface pressure remains of the order of the driving pressure $\mathbf{\Delta}\Pi$ for the majority of the channel and thus pumps a larger surfactant flux, effectively increasing the permeability of the channel. By contrast, surface pressure drops rapidly at the channel entrance when Π-thickening, which maintains a relatively small gradient across the rest of the channel, thereby ‘choking’ the surface flow.

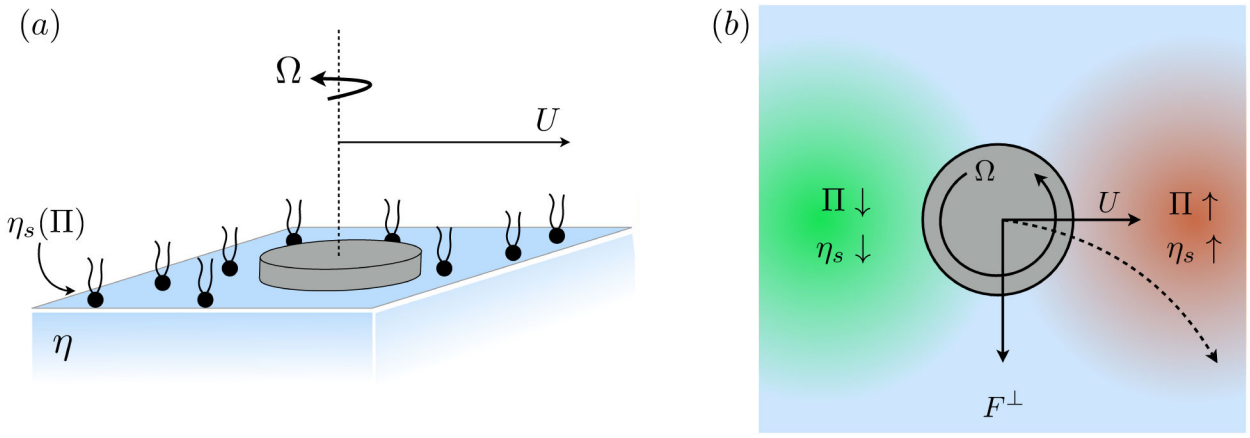

Figure 30.

Surface 'Magnus' Effect. (*a*) A circular particle forced to rotate while translating in a *Π*-thickening surfactant follows a Magnus-like trajectory (*b*) Surfactant in front fo the translating disk has higher surface viscosity than the surfactant behind the disk, owing to the higher surface pressure. Consequently, the rotation of the particle causes it to 'roll' upwards, perpendicular to the direction of forcing (Manikantan & Squires 2017*a*).

Table 1.

Common adsorption isotherms, and corresponding expressions for surface pressure and the Marangoni modulus.

Isotherm	Description	$\Pi(C)$	$\Pi(\Gamma)$	$E_0(\Gamma)$
Henry	2D ideal gas dilute	KC	$k_B T\Gamma$	$k_B T\Gamma$
Freundlich	empirical	$(KC)^m$	$k_B T\frac{\Gamma}{m}$	$k_B T\frac{\Gamma}{m}$
Langmuir	adsorbs to empty sites no interactions	$\frac{\Gamma_\infty KC}{1+KC}$	$k_B T\Gamma_\infty \ln\left[\frac{1}{1-\Gamma/\Gamma_\infty}\right]$	$\frac{k_B T\Gamma}{1-\Gamma/\Gamma_\infty}$
Volmer	finite molecule size	$\frac{\Gamma_\infty KC}{\exp\left[\frac{\Gamma}{\Gamma_\infty-\Gamma}\right]+KC}$	$\frac{k_B T\Gamma}{1-\Gamma/\Gamma_\infty}$	$\frac{k_B T\Gamma}{(1-\Gamma/\Gamma_\infty)^2}$
Frumkin	adsorbs to empty sites lateral interactions	$\frac{\Gamma_\infty KC}{\exp\left[-\frac{\beta\Gamma}{k_B T}\right]+KC}$	$k_B T\Gamma_\infty \ln\left[\frac{1}{1-\Gamma/\Gamma_\infty}\right]-\frac{\beta\Gamma^2}{2}$	$\frac{k_B T\Gamma}{1-\Gamma/\Gamma_\infty}-\beta\Gamma^2$
van der Waals	finite molecule size lateral interactions	$\frac{\Gamma_\infty KC}{\exp\left[\frac{\Gamma}{\Gamma_\infty-\Gamma}-\frac{\beta\Gamma}{k_B T}\right]+KC}$	$\frac{k_B T\Gamma}{1-\Gamma/\Gamma_\infty}-\frac{\beta\Gamma^2}{2}$	$\frac{k_B T\Gamma}{(1-\Gamma/\Gamma_\infty)^2}-\beta\Gamma^2$

Table 2.

Example adsorption and desorption fluxes for the isotherms detailed in table 1. Because only the *ratio* of j_a and j_d is constrained by equilibrium thermodynamics, each pair (j_a and j_d) in this table may be multiplied by any function of C and Γ without changing its equilibrium isotherm. Different surfactants with identical isotherms may respond very differently under dynamic conditions.

Isotherm	Adsorption flux, j_a	Desorption flux, j_d
Henry	$k_a C$	$k_d \Gamma$
Freundlich	$k_a K^{m-1} C^m$	$k_d \Gamma$
Langmuir	$k_a C(\Gamma_\infty - \Gamma)$	$k_d \Gamma$
Volmer	$k_a C(\Gamma_\infty - \Gamma)$	$k_d \Gamma \exp\left[\frac{\Gamma}{\Gamma_\infty - \Gamma}\right]$
Frumkin	$k_a C(\Gamma_\infty - \Gamma)$	$k_d \Gamma \exp\left[-\frac{\beta \Gamma}{k_B T}\right]$
van der Waals	$k_a C(\Gamma_\infty - \Gamma)$	$k_d \Gamma \exp\left[\frac{\Gamma}{\Gamma_\infty - \Gamma} - \frac{\beta \Gamma}{k_B T}\right]$

Table 3.

Common definitions of the Marangoni number, and their physical meaning. Temperature-dependent Marangoni effects are not considered here, and we list only the effects of composition dependence.

Definition	Description	Representative examples
$Ma = \frac{E_0}{\eta U}$	interfacial elasticity vs subphase viscous stress: measure of how much the subphase flow compresses the interface	Stebe *et at.* (1991) Seiwert *et al.* (2014)
$Ma_D = \frac{E_0 L}{\eta D_s}$	relaxation of concentration gradients due to Marangoni convection vs due to surface diffusion	Durand & Langevin (2002) Elfring *et al.* (2016)
$Ma_K = \frac{E_0 \tau_s}{\eta L}$	relaxation of concentration gradients due to Marangoni convection vs due to adsorption/desorption	Elfring *et al.* (2016)
$Ma_S = \frac{E_0 L}{\eta_s U}$	interfacial elasticity vs surface viscous stress (characterized by η_s or κ_s)	Verwijlen *et al.* (2012)
$Ma_\gamma = \frac{E_0}{\gamma}$	Marangoni vs capillary stress: relevant in applications with interfacial curvature like drop coalescence and fiber coating	Dai & Leal (2008) Quéré (1999)

Table 4.

Summary of asymptotic limits, when available, of the resistance coefficient $|\boldsymbol{F}|/4\pi\eta R|\boldsymbol{U}|$ for the translation of a cylindrical disk.

	deep subphase ($H \gg R$)	**shallow subphase ($H \ll R$)**
clean interface	$\frac{4}{3\pi}$	$\frac{2}{5}\frac{R}{H}$
Incompressible, inviscid monolayer $Ma \gg 1$ and $Bq = 0$	$\frac{2}{\pi}$	$\frac{1}{2}\frac{R}{H}$
Incompressible, viscous monolayer $Ma \gg 1$ and $Bq \to \infty$	$\frac{Bq}{\log(2Bq) - \gamma_E}$	$\frac{Bq}{\log(2\sqrt{BqH/R}) - \gamma_E}$
Compressible, inviscid monolayer $Ma \to 1$ and $Bq \to 0$	$\frac{4}{3\pi}$	$\frac{2}{5}\frac{R}{H}$
Compressible, viscous monolayer $Ma \to 1$, $Bq \to \infty$, and $\kappa_s \ll \eta_s$	-	$\frac{Bq/2}{\log(\sqrt{2BqH/R}) - \gamma_E}$
Compressible, viscous monolayer $Ma \to 0$, $Bq \to \infty$, and $\kappa_s \gg \eta_s$	-	$\frac{Bq}{\log(2\sqrt{BqH/R}) - \gamma_E}$